

**FRACTURE BEHAVIOR OF FIBER-REINFORCED  
CEMENTED PASTE BACKFILL UNDER CURING PRESSURE**

by

**Brett Holmberg**

A thesis

submitted to the Faculty of Graduate Studies  
in partial fulfillment of the requirements for the  
Degree of Master of Science

in

Civil Engineering

Supervisor

**Dr. Liang Cui**

Associate Professor – Dept. of Civil Engineering

Lakehead University

Thunder Bay, Ontario

August 2022

© Brett Holmberg, 2022

## **Author's Declaration Page**

I hereby declare that I am the sole author of this thesis. This is a true copy of the thesis, including any required final revisions, as accepted by my examiners. I understand that my thesis may be made electronically available to the public.

## **Abstract**

Due to the rapid strength acquisition rate, relatively high solid content, and sustainable reuse of waste tailings, cement paste backfill (CPB) technology has gradually become a standard practice in underground mining operations. To improve the engineering behavior and performance of CPB materials, fiber-reinforced CPB (FR-CPB) has attracted increasing interest over the past decade. The application of fiber reinforcement can improve the mechanical properties, including the material strength and ductility, and enhance post-peak resistance. However, the successful implementation of fiber reinforcement requires the full consideration of field curing conditions. After placement into underground mined-out voids (called stopes), the massive backfill structure (with a backfilling height of tens to hundreds of meters) yields a high-level curing pressure under the gravity effect, which accompanies the development of microstructure and macroscale mechanical properties of backfill materials from early to advanced ages. Therefore, to accurately assess the development of mechanical properties and behaviors of FR-CPB, it is essential to fully consider the effect of curing pressure. Moreover, the previous studies focus mainly on the conventional geomechanical behaviors, including compressive, tensile, and shear behaviors, of FR-CPB materials based on the elastoplastic theory. As a result, the previous studies aim to correlate the permanent deformation and material degradation and thus evaluate and design backfill materials for their engineering applications. However, as a type of cementitious material, the brittle response and the associated catastrophic failure of the CPB matrix are governed by the crack growth. Through crack propagation and coalescence, the degradation of mechanical properties occurs and may lead to material failure at the macroscale. Therefore, the brittle failure process in the CPB matrix indicates that fracture behaviors and properties of FR-CPB are intrinsically required by a reliable and accurate assessment of in-stope behavior and performance of backfill materials. Considering the in-situ loading conditions, both tensile and shear cracks can develop in the hardened CPB matrix. Therefore, it is necessary to study the fracture behavior and properties of FR-CPB materials under various loading conditions, including mode-I (tensile stress), mode-II (in-plane shear stress), and mode-III (out-of-plane shear stress) loadings. Correspondingly, a systematic investigation of the fracture behavior and properties of FR-CPB has been designed and conducted through this study. A new curing pressure apparatus featured with an air-pressure control system, high volume capacity, and simple assemble/disassemble operation is

developed to capture the effect of curing pressure. Moreover, a series of fracture behavior tests, including semicircular bend (SCB) tests and edge notched disc bend (ENDB) tests, are conducted on FR-CPB and control CPB without fiber reinforcement at different curing pressures (0 kPa, 100kPa, and 200kPa), and different curing times (3 days, 7 days, 28 days, and 56 days). Meanwhile, to facilitate the identification of mechanisms responsible for the changes in microstructure and macroscale fracture properties, the scanning electron microscopy observation and measurement of dry density of FR-CPB and control CPB specimens are measured. The obtained results show that the curing pressure influences fracture behavior of FR-CPB, especially the post-peak behaviors, which confirms the effect of curing pressure on the fiber reinforcement. Moreover, curing pressure also affects the time-dependent evolution of fracture properties, including stiffness, fracture toughness, and fracture energy from early to advanced ages. This is because a higher curing pressure leads to matrix densification and thus contributes to a continuous improvement in the fracture properties. Furthermore, a very limited variation of fracture toughness ratios has been discovered in this study, which indicates that mode-I fracture toughness can be used as a valuable quantity to approximate the fracture modes-II and modes-III for FR-CPB materials. In addition, through sensitivity analysis of fracture properties, it has been found that fracture toughness can be employed as a more reliable fracture property to evaluate fracture behavior of mine backfill structure under high geo-stress.

**Keywords:** FR-CPB, Induced Curing Pressure, Fracture toughness, Fracture Energy

## **Acknowledgments**

I would first and foremost like to acknowledge my thesis supervisor Dr. Liang Cui, for the mentorship and guidance he has provided throughout this research program. He has provided me with the capabilities and determination to not only follow where the path may lead but also to create my own trail.

Thank you to my family for their continued support, care, and kindness throughout this journey I have embarked on. Without you, I would not be where I am today. To my partner, Taylor, whose belief in my abilities at times surpassed my own. Thank you for being my better half and for your patience, understanding, and continued support from the beginning. To my colleagues, Aaron McAdie, Javaughn Mclean, and Sami Hassan, for reminding my struggles were never mine alone. Thank you for making this experience one of shared memories and enjoyment.

And finally, to the thesis committee members Dr. Baoqiang Liao and Dr. Jian Deng for their time, consideration, and valuable suggestion towards the continued pursuit and further enhancement of this work.

## Table of Contents

Abstract	iii
Acknowledgments.....	v
List of Tables .....	ix
List of Figures.....	x
List of Abbreviations .....	xiv
Abbreviations .....	xiv
Nomenclature.....	xv
Roman .....	xv
Greek.....	xvi
Chapter 1 Introduction .....	1
1.1 Background .....	1
1.2 Problem statement.....	3
1.3 Research methodologies.....	6
1.4 Thesis organization .....	7
Chapter 2 Literature review .....	2
2.1 Introduction.....	2
2.2 Mechanical process in FM-ITZ under induced curing pressure .....	5
2.2.1 Stress State and volume change in FM-ITZ.....	6
2.2.2 Multicracking behavior in FM-ITZ .....	7
2.3 Hydraulic process in FM-ITZ under induced curing pressure .....	9
2.3.1 Pore-water seepage behavior in FM-ITZ.....	9
2.3.1 Evolution of water retention capacity in FM-ITZ .....	11
2.4 Thermal process in FM-ITZ under induced curing pressure.....	13
2.4.1 Heat Transfer in FM-ITZ.....	13

2.4.2 Thermal deformation in FM-ITZ.....	16
2.5 Chemical process in FM-ITZ under induced curing pressure.....	18
2.5.1 Cement hydration kinetics in FM-ITZ.....	18
2.5.1 Hydration products in FM-ITZ.....	22
2.6 Discussion of the effects of induced curing pressure on the FM-ITZ.....	24
2.7 Conclusions from Literature Review .....	27
Chapter 3 Experimental testing program .....	29
3.1 Materials.....	29
3.2 Mix recipe and specimen preparation .....	30
3.3 A new curing pressure apparatus .....	33
3.4 Mechanical testing program .....	35
3.4.1 End Notch Disc Bend (ENDB) Test.....	35
3.4.2 Semicircular Bend (SCB) Test .....	37
3.4.3 Testing procedure .....	39
3.5 Scanning Electron Microscope (SEM) Analysis.....	40
3.6 Determination methods of fracture properties .....	41
3.6.1 Material Stiffness.....	41
3.6.2 Fracture Toughness.....	42
3.6.3 Energy of Fracture .....	44
Chapter 4 Experimental results.....	45
4.1 Evolutive fracture behavior and properties of CPB under curing pressure.....	45
4.1.1 Effect of curing pressure on mode-I fracture behavior of CPB.....	45
4.1.2 Effect of curing pressure on mode-II fracture behavior of CPB .....	46
4.1.3 Effect of curing pressure on mode-III fracture behavior of CPB .....	48
4.1.4 Effect of curing pressure on fracture properties of CPB .....	50

4.1.5 Sensitivity analysis of fracture toughness and energy of fracture initiation of CPB to curing pressure.....	55
4.2 Evolutive fracture behavior and properties of FR-CPB under curing pressure .....	59
4.2.1 Effect of curing pressure on mode-I fracture behavior of FR-CPB .....	59
4.2.2 Effect of curing pressure on mode-II fracture behavior of FR-CPB .....	62
4.2.3 Effect of curing pressure on mode-III fracture behavior of FR-CPB.....	64
4.2.4 Effect of curing pressure on fracture properties of FR-CPB .....	66
4.2.5 Sensitivity analysis of fracture toughness and energy of fracture initiation of FR-CPB to curing pressure.....	74
Chapter 5 Conclusions and recommendations .....	77
5.1 Conclusions .....	77
5.2 Recommendations for future work.....	80
References	82

## List of Tables

<b>Table 2-1.</b> Comparison of material properties between FM-ITZ and bulk matrix. ....	2
<b>Table 2-2</b> Summary of porosity- and saturation-dependent models for thermal conductivity of porous media. ....	17
<b>Table 2-3.</b> Typic cement hydration models.....	19
<b>Table 3-1</b> Grade Curve Characteristics. ....	29
<b>Table 3-2</b> Fiber Properties.....	30
<b>Table 3-3</b> Mix Design. ....	31

## List of Figures

<b>Figure 1-1</b> Pumping of fresh CPB into open stope. ....	1
<b>Figure 1-2</b> Frequency of tailings dam failures from 1960 to 2018 by year [7].....	2
<b>Figure 1-3</b> Modes of Loading .....	4
<b>Figure 1-4</b> Microstructure of interfacial transition zone of (a) polypropylene fiber reinforced concrete[8], and (b) cemented paste backfill[40]. ....	6
<b>Figure 2-1.</b> Correlation among induced curing pressure, multiphysics process, and fiber-matrix interface behavior.....	4
<b>Figure 2-2.</b> Confining pressure dependency of triaxial compressive behavior of 90-day polypropylene fiber reinforced cemented paste backfill under consolidated undrained tests: (a) deviatoric stress-axial strain curve and (b) volumetric strain-axial strain curve. ....	5
<b>Figure 2-3.</b> Effect of interfacial contact pressure, $\sigma_c$ , on pullout response of stainless fiber embedded into concrete (compressive stress is considered negative)[76].....	7
<b>Figure 2-4.</b> Crack deflection and branching in FM-ITZ of steel fiber-reinforced mortar[93]. ....	8
<b>Figure 2-5.</b> Evolution of (a) volumetric water content and (b) matric suction in FR-CPB and plain CPB. ....	9
<b>Figure 2-6.</b> Excess pore water pressure dissipation in (a) cemented paste backfill and (b) fiber-reinforced cemented paste backfill under cyclic shear loading [97].....	11
<b>Figure 2-7.</b> Evolution of matric suction and water content in FRCC. ....	12
<b>Figure 2-8.</b> Dependence of thermal conductivity on the volumetric water content in FRCC (FC: fiber weight content w.r.t. the total weight of solid phase)[114]. ....	14
<b>Figure 2-9.</b> Dependence of cement hydration rate on curing pressure[120]. ....	15
<b>Figure 2-10.</b> Dependence of thermal expansion of confined water on pore size[125]. ....	17
<b>Figure 2-11.</b> Dependence of cement hydration on curing pressure at 38°C [173]. ....	22
<b>Figure 2-12.</b> Microcracking in C <sub>3</sub> S matrix under a stress of 6.8MPa after 18-hour hydration (a) 350x (b) 300x [120]. ....	22
<b>Figure 2-13.</b> TEM image of LD CSH and HD CSH in a mature C <sub>3</sub> S paste (CH: calcium hydroxide)[195]. ....	24
<b>Figure 3-1</b> Particle Size Distribution. ....	29
<b>Figure 3-2</b> (a) Kitchen Aid Mixer (b) CPB in cylinder mold. ....	30

<b>Figure 3-3</b> Polypropylene Fibers (a) before and (b) after separation.....	32
<b>Figure 3-4</b> Pressure tanks.....	33
<b>Figure 3-5</b> Modifications to the Levlor Sprayer Tanks (a) internal rods (b) pressure gauge (c) quick connect coupler and regulator (d) laboratory supply outlets. ....	34
<b>Figure 3-6.</b> FR-CPB samples for ENDB tests (a) side view ENDB schematic (b) side view ENDB FR-CPB sample (c) loading bar ENDB schematic (d) loading bar ENDB FR-CPB sample. ....	36
<b>Figure 3-7</b> Self-designed cutting Jigs for fabrication of SCB and END samples (a) mode-III, mode-I, and semi-circular cut Jig top view (b) mode-III, mode-I, and semi-circular cut Jig side view (c) mode-II Jig side view (d) mode-II Jig top view. ....	37
<b>Figure 3-8.</b> CPB samples for mode-I and mode-II SCB tests. (a) top view schematic b) top view sample c) side view mode-I SCB dimensions d) side view mode-I specimen e) side view mode-II SCB dimensions f) side view mode-II specimen.....	38
<b>Figure 3-9</b> Bar Spacing of SCB Loading Frame (a) loading bar schematic (b) FR-CPB sample in load frame. ....	39
<b>Figure 3-10</b> ELE load frame and computer set up. ....	40
<b>Figure 3-11</b> a) Hitachi Su-70 microscope b) gold coated FR-CPB samples. ....	41
<b>Figure 3-13</b> Calculation of stiffness from load-displacement graph.....	42
<b>Figure 3-14</b> Definition of fracture properties of FR-CPB:(a) energy of fracture initiation and (b) energy of fiber bridging. ....	44
<b>Figure 4-1.</b> Effect of curing pressure on the mode-I load-displacement curves at (a) 3 days, (b) 7 days, (c) 28 days, and (d) 56 days.....	45
<b>Figure 4-2.</b> Effect of curing pressure on the mode-II load-displacement curves at (a) 3 days, (b) 7 days, (c) 28 days, and (d) 56 days.....	46
<b>Figure 4-3</b> SEM images of microstructure of control CPB matrix at (a) 3 days, (b) 7 days, (c) 28 days, and (d) 56 days. ....	47
<b>Figure 4-4</b> SEM images of microstructure of 28 day CPB matrix at (a) 0 kPa, (b) 100 kPa and (c) 200 kPa.....	48
<b>Figure 4-5.</b> Effect of curing pressure on the mode-III load-displacement curves at (a) 3 days, (b) 7 days, (c) 28 days, and (d) 56 days.....	49
<b>Figure 4-6.</b> Effect of curing pressure on evolutive stiffness of CPB under (a) mode-I, (b) mode-II, and (c) mode-III loadings.....	50

<b>Figure 4-7.</b> Effect of curing pressure on evolutive fracture toughness of CPB under (a) mode-I, (b) mode-II, and (c) mode-III loadings. ....	52
<b>Figure 4-8.</b> Effect of curing pressure on evolutive energy of fracture initiation ( $W_c$ ) of CPB under (a) mode-I, (b) mode-II, and (c) mode-III loadings. ....	54
<b>Figure 4-9.</b> Comparison of the percent increase in $K_c$ and $W_c$ at (a) different curing times and (b) different curing pressures. ....	56
<b>Figure 4-10.</b> Comparison of the sensitivity of $K_c$ and $W_c$ to (a) curing times and (b) curing pressures. ....	57
<b>Figure 4-11.</b> Comparison of dominant fracture quantities at (a) different curing times, and (b) different curing pressure. ....	58
<b>Figure 4-12.</b> Effect of curing pressure on the mode-I load-displacement curves at (a) 3 days, (b) 7 days, (c) 28 days, and (d) 56 days. ....	59
<b>Figure 4-13.</b> Fiber bridging across the crack surfaces in FR-CPB under mode-I loading (without curing pressure) at (a) 3 days, (b) 7 days, (c) 28 days, and (d) 56 days. ....	60
<b>Figure 4-14</b> Images of microstructure of 28-day FR-CPB matrix at (a) 0 kPa, (b) 100 kPa and (c) 200 kPa. ....	62
<b>Figure 4-15.</b> Effect of curing pressure on the mode-II load-displacement curves at (a) 3 days, (b) 7 days, (c) 28 days, and (d) 56 days. ....	63
<b>Figure 4-16.</b> Effect of curing pressure on the mode-III load-displacement curves at (a) 3 days, (b) 7 days, (c) 28 days, and (d) 56 days. ....	65
<b>Figure 4-17.</b> Effect of curing pressure on evolutive stiffness of FR-CPB under (a) mode-I, (c) mode-II, and (c) mode-III loadings. ....	67
<b>Figure 4-18.</b> SEM images of microstructure of control CPB matrix at (a) 3 days, (b) 7 days, (c) 28 days, and (d) 56 days. ....	67
<b>Figure 4-19.</b> Effect of curing pressure on evolutive fracture toughness of FR-CPB under (a) mode-I, (c) mode-II, and (c) mode-III loadings. ....	69
<b>Figure 4-20</b> Improvements to the ITZ of fiber and matrix with increasing curing pressure a) 0 kPa b) 100 kPa c) 200 kPa. ....	71
<b>Figure 4-21.</b> Comparison of fracture toughness ratios of FR-CPB. ....	72

**Figure 4-22.** Effect of curing pressure on evolutive energy of fracture initiation ( $W_c$ ) and fracture energy of fiber bridging ( $W_f$ ) of FR-CPB under (a and b) mode-I, (c and d) mode-II, and (e and f) mode-III loadings..... 73

**Figure 4-23.** Comparison of the percent increase in  $K_c$  and  $W_c$  at (a) different curing times and (b) different curing pressures..... 75

**Figure 4-24.** Comparison of the sensitivity of  $K_c$  and  $W_c$  to (a) curing times and (b) curing pressures..... 76

**Figure 4-25.** Comparison of dominant fracture quantities at (a) different curing times, and (b) different curing pressure. .... 76

## List of Abbreviations

### Abbreviations

CPB	Cement Paste Backfill
FR-CPB	Fiber Reinforced Cement Paste Backfill
CHF	Cemented Hydraulic Fill
UCS	Uniaxial Compressive Strength
ITZ	Interfacial Transition Zone
FRCC	Fiber Reinforced Cementitious Composite
FM-ITZ	Fiber Matrix Interfacial Transition Zone
THMC	Thermal Hydraulic Mechanical Chemical
CTE	coefficient of thermal expansion
HD	High Density
LD	Low Density
TEM	transmission electron microscopy
ENDB	End Notch Disc Bend
SCB	Semicircular Bend
LVDT	Linear Variable Differential Transformer
SEM	Scanning Electron Microscope
MSDA	Material Strength Design Approach
W/C	Water to Cement Ratio
Cm	Cement Content by Mass

## Nomenclature

### Roman

a	Depth of notch (mm)
D	Diameter of specimen (mm)
$E_a$	Activation Energy (J/mol)
$C_i$	Fitting Constants (i=1 to 4)
$K_c$	Fracture Toughness (Pa. $\sqrt{m}$ )
$K_I$	Mode-I Fracture Toughness (Pa. $\sqrt{m}$ )
$K_{II}$	Mode-II Fracture Toughness (Pa. $\sqrt{m}$ )
$K_{III}$	Mode-III Fracture Toughness (Pa. $\sqrt{m}$ )
$K_T$	Thermal Conductivity (W/mK)
$M_c$	Mass of wax-coated specimen (g)
MC	Moisture content
$M_{dry}$	Mass of dried sample (g)
$M_t$	Mass of moist(total) specimen (g)
$M_{sub}$	Mass of the wax-coated specimen, submerged in water (g)
$M_{wet}$	Mass of the wet sample(g)
P	Peak load (N)
$\bar{P}_i$	Average percent increase
$P_k$	Percent increase in $K_c$
$P_r$	Reference Pressure (MPa)

$P_w$	Percent increase in $W_c$
$q$	Heat Flux ( $W/m^2$ )
$R$	Ideal Gas Constant ( $8.3145J/mol \cdot K$ )
$R$	Radius of specimen (mm)
RH	Relative Humidity
$r$	Pore Radius (mm)
$S$	Distance between central and edge bar of loading frame (mm)
$S_I$	Sensitivity Index
$t$	Curing Time (D)
$T$	Thickness of specimen (mm)
$T_s$	Surface Tension (N/m)
$V$	Volume of test specimen ( $cm^3$ )
$Y_I$	Normalized stress intensity factor for mode I (6.52)
$Y_{II}$	Normalized stress intensity factor for mode II (1.072)
$Y_{III}$	Normalized stress intensity factor for mode III (0.0713)

## **Greek**

$\nabla T$	Temperature Gradient (K)
$\Delta V$	Activation Volume ( $m^3/mol$ )
$\delta_{40}$	Displacement corresponding to 40% peak load (mm)
$\delta_{60}$	Displacement corresponding to 60% peak load (mm)
$\epsilon_T$	Thermal Deformation
$\sigma_c$	Interfacial Contact Pressure (MPa)
$\rho_x$	density of wax ( $g/cm^3$ )
$\rho_w$	Density of water( $g/cm^3$ )

$\rho_d$	Dry Density( $\text{g}/\text{cm}^3$ )
$\xi$	Dimensionless Hydration Degree
$\alpha_H$	Pore water Activity
$\Psi$	Soil Suction (Pa)

# Chapter 1 Introduction

## 1.1 Background

Traditional methods of mine waste disposal, such as above ground sequestration in artificial dams, leads to environmental concerns, with alternative methods of disposal gaining popularity in both industry and the global community[1-2]. Of the viable alternatives, the use of cement paste backfill (CPB) has gained popularity in recent years as it offers greater strength than that of its counterpart hydraulic fill while simultaneously reducing the need for surficial storage of tailings waste[3-4]. The main hindrance to the use of CPB is the cost associated with the implementation and continued use of such systems. As such, further investigation into the material properties, performance, and refinement of design may lead to increased acceptance and use within the industry. CPB is comprised of up to 85% thickened mine tailings, 3-7% cement binder, and water [5]. The material is batched at the surface and then pumped underground through a network of pipes into previously excavated sections of the mine known as stopes (Figure 1-1). Its placement is used as a ground support measure, preventing ground subsidence, rock burst, or general collapse of the stope walls or roof. Moreover, with the progression of underhand cut and fill, the material itself may be used as an artificial roof or as a working platform for continued mining activities. As such, an assurance of the material's strength and capabilities is vital in maintaining safe work procedures in the underground environment.

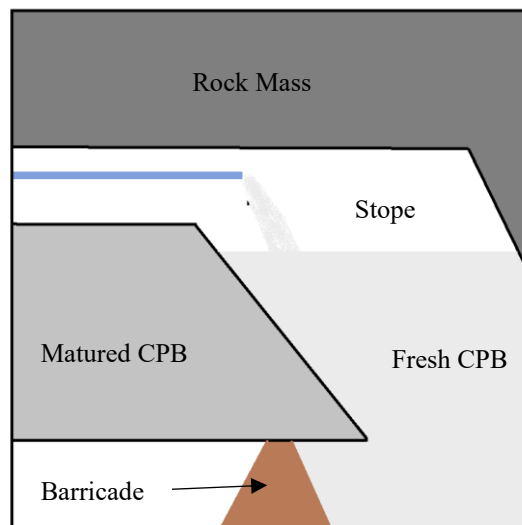
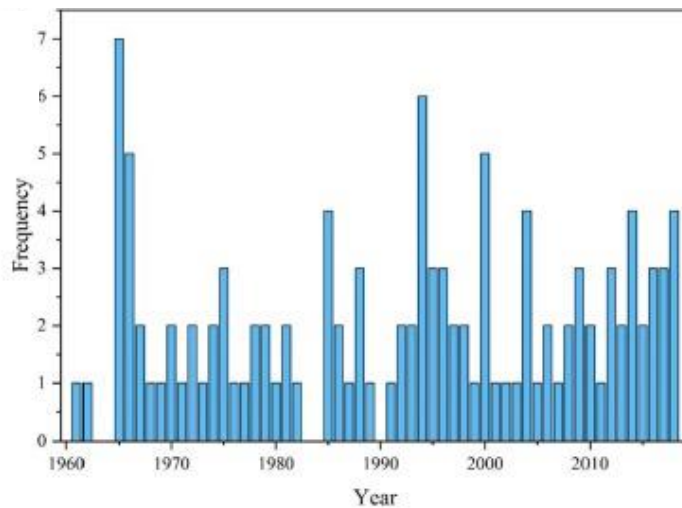


Figure 1-1 Pumping of fresh CPB into open stope.

While this study will focus on the material strength characteristics of CPB, the advantages can be viewed from environmental, structural, and economic aspects. With regard to the environmental perspective, the sequestration of mining waste in tailings dams is fraught with environmental concerns and disasters. The variability in standards of construction, as well as the need for consistent monitoring from inception to the end of lifespan and post-reclamation future, have resulted in a multitude of failures. While failures occur on a smaller scale each year, a major failure has occurred as recently as 2019. In January of 2019, a tailings dam collapse in Brumadinho, Brazil, resulted in the release of over 11 million cubic meters of toxic waste material, spreading over a 10 km area, entering major waterways, and seeping into the surrounding soils [6]. Figure 1-2 highlights the frequency of tailings dam failures from 1960 to 2018 and as such the environmental risk associated with continued implementation [7]. The use of CPB as a method of tailings sequestration has the ability to reduce the total volume of surficially stored waste material and thus the potential for environmental disaster. From a structural perspective, CPB provides superior support than that of its counterpart cemented hydraulic fill (CHF) while also reducing the potential for serious geotechnical hazards related to the failure of CHF barricades. Over the past three decades, we have seen the switch from CHF to CPB not only for its increased structural capacity but also to reduce the relation to cement binder used [8]. From an economic standpoint, the cost of the cement binder in CPB can account for 75% of the overall cost of the material [9], as such the continued refinement of the design will lead to a further reduction in overhead costs.



**Figure 1-2** Frequency of tailings dam failures from 1960 to 2018 by year [7].

Traditional methodologies of CPB mix design have focused on the material strength-based design approach (MS-DA) [2,5]. As CPB is required to provide adequate ground support to the surrounding rock mass, its ability to resist compressive forces is understood to play an important role in the stability of the structure. The use of uniaxial compressive strength (UCS) testing is, therefore, one of the main methods of determining material strength and designing CPB structures. Extensive studies have been conducted to experimentally and numerically investigate the compressive behavior of CPB material in the form of (UCS) testing[10–13], with a common UCS range of 0.2-4 mPa[14]. As a means to improve the UCS and mechanical behavior of cementitious materials, the addition of fiber reinforcement has also been heavily investigated[15–18]. This research has been applied in multiple studies to CPB. X.W.Yi et al. [19] investigated the effects of fiber reinforcement in CPB at varying amounts of cement content. The inclusion of fiber improved both the UCS and the ductility of CPB, with a 0.5% fiber inclusion resulting in compressive strength gains between 70-90% and an axial strain at failure 300% greater than that of the control tests. The importance of this result is further highlighted when noting that the fiber reinforced cement paste backfill (FR-CPB) with 3% cement reached higher compressive strengths than that of the CPB with a cement content of 5%. Similar results were found by Chen et al. [20] when performing a fiber optimization study of CPB. An average improvement in UCS with the addition of 0.15% fiber was 213.11%, 43.96%, and 143.45% at respective ages of 3, 7, and 28 days. While improving the mechanical properties, the incorporation of fiber reinforcement to CPB also has the benefit of providing the brittle material with a residual strength after cracking[18] [21]. This is important as fiber thus allows for the progressive failure of the structure rather than catastrophic.

## **1.2 Problem statement**

While UCS testing is essential in the design of FR-CPB structure, the highly dynamic environment in which material is placed leads to the formation of complex loading conditions and, therefore, complex methods of failure. As discussed in section 1.1, extensive studies have been conducted on the capacity of FR-CPB. It should be noted that additional studies have been conducted on the other conventional geomechanical behaviors of FR-CPB, such as tensile and shear strength[22-23]. The methodology of this testing with respect to failure in an actual CPB structure, however, does not take into account the likely process of crack initiation and propagation within the FR-

CPB matrix. Furthermore, the complexity of the loading, such as that of the polyaxially condition, allows for the conjunctive development of both tensile and shear cracks within the mass. Tensile cracking will occur both with the progression of underhand cut and fill (the FR-CPB mass acting as a roof), and through the biaxial loading condition created during the subsequent excavation of adjacent rockfaces. As well, within the mass itself, the unequal principal stresses resulting from changes in confinement will yield to the formation of shear stress and the subsequent propagation of shear cracking. By nature of the blasting used in excavation, the walls of a stope are characterized by rough non-homogenous surfaces, with convex and concave wedges of rock mass. As such the interface of FR-CPB is characterized by micro and macroscopic notches, not unlike the formation of cracks along the surface. Based on this form of structure the investigation of the material properties of FR-CPB thus lends itself to the study of fracture mechanics more so than geomechanical analysis. With regard to Figure 1-3, the development of Mode-I, tensile loading conditions, is present in the underhand roof of the mine (A) and the exposed face of matured CPB (B), mode-II, in plane shear loading conditions are present within the mass of CPB body (C) and along the face of the exposed face of matured CPB (B), and mode-III, out of plane shear loading is present in the exposed face of matured CPB (B). As such an investigation of the fracture behaviour and properties of FR-CPB under mode-I, mode-II, and mode-III loading can provide an in-depth insight into mechanical behavior and performance of FR-CPB materials, contributing to the successful implementation of fiber reinforcement in underground mine backfill operation.

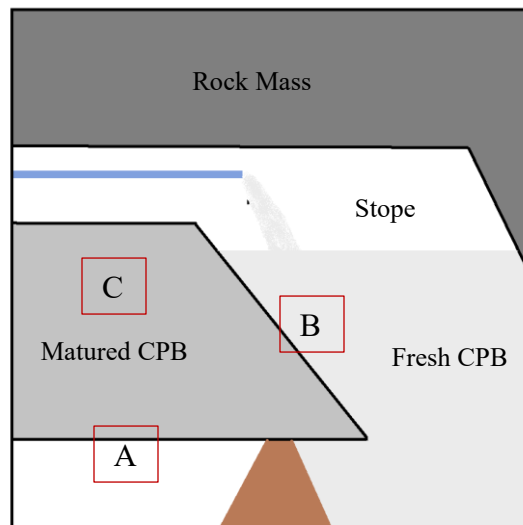


**Figure 1-3** Modes of Loading

The second objective of this study addresses the in-situ conditions faced by FR-CPB during placement and subsequent curing in underground mining stopes. There have been several major investigations into the in-situ properties of cement paste backfill, the results indicating an underrepresentation of material strength when compared to that of conventional laboratory analysis[24–27]. For instance, studies by Cayouette [28] and Revell [25] found in situ UCS strengths of CPB up to 200% higher than that of the same mixes cured under laboratory conditions[29]. Additionally, a field study of the golden giant mine by Le Roux et al. [25] found discrepancies in the material properties and a shear strength 50%-80% higher than that of laboratory conditions. Prior investigations into the field's strengths of CPB have highlighted the effects of induced curing pressure on the microstructural development and macroscale mechanical response from early to advanced ages. Mining stopes vary based on the methodology of excavation, with long hole mining having the ability to reach tens of meters in the cross-sectional and vertical dimensions, or that of alimak mining having small cross-sectional areas but the potential to reach hundreds of meters in height[30]. As such, the continued filling process of the stope results in uniquely high self-weight induced stress. This coinciding with the large confining pressures developed by excavation contraction and high geostress leads to the formation of an induced curing pressure on the CPB material. The works of Yilmaz et al. [31-32], Ghirian and Fall. [33] and Cui and Fall. [34] each found that the increase in effective stress associated with higher curing pressure led to a reduction in porosity/ void ratio and thus a strengthening of the CPB matrix. The addition of fibers to cementitious material leads to the formation of mesoscale interfacial transition zones (ITZ) between the fibers and matrix [35-36]. This may be attributed to the wall effect between the larger fibers and spatial packing pattern of the fine particles that make up the CPB matrix[37]. As a result, the ITZ is generally characterized by loose particle packing and a higher porosity than that of the bulk matrix (Figure 1-4)[38]. FR-CPB is thus sensitive to changes to its pore structure and induced curing pressure is crucial to the effectiveness of the fiber reinforcement technique for CPB materials in underground mines[39]. To discover the fracture behavior and properties of in-situ CPB materials, the induced curing pressure must therefore be fully considered. However, no studies have been designed and conducted to systematically investigate the effect of curing pressure on fracture behavior of FR-CPB, which significantly affects the thorough understanding of failure process in FR-CPB and thus the safe design of FR-CPB technology. To address this research gap, a comprehensive experimental testing program, and new pressure curing system is

developed through this thesis study to investigate the effect of curing pressure on the evolutive mode-I, mode-II, and mode-III fracture behaviors and properties of FR-CPB at various curing times. The obtained results can significantly improve the understanding of FR-CPB, and thus promotes its successful application in underground mine backfill operation.

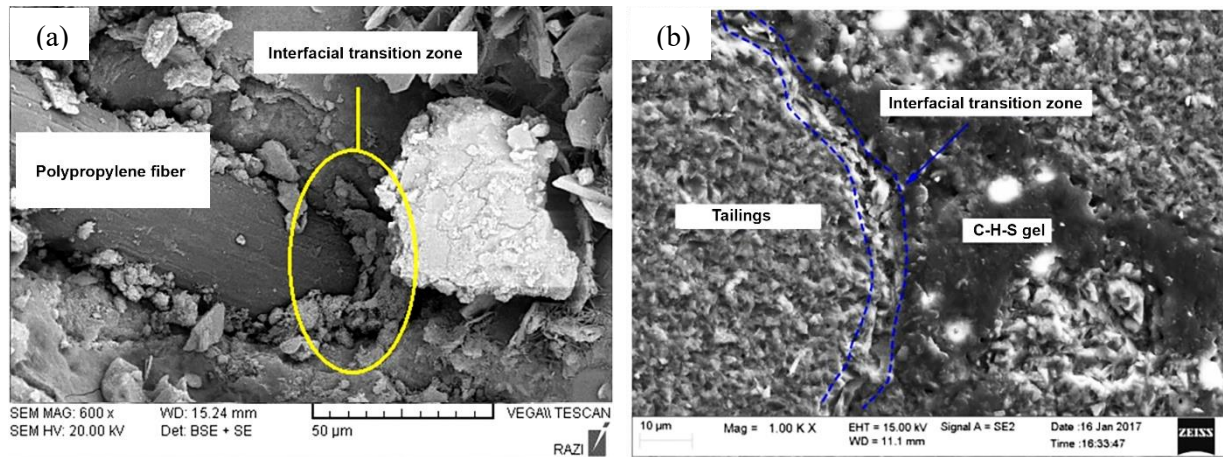


**Figure 1-4** Microstructure of interfacial transition zone of (a) polypropylene fiber reinforced concrete[8], and (b) cemented paste backfill[40].

### 1.3 Research methodologies

In order to address the research gap and investigate the effect of induced curing pressure on the fracture behavior of FR-CPB, the following research methodologies were implemented:

1. A comprehensive literature review of the effect of induced curing pressure on the multiphysics process occurring in the interfacial transition zone of fiber-reinforced cementitious composites.
2. Construction of a cost-effective pressure curing apparatus to apply the curing pressure on multiple samples.
3. An experimental testing program capable of investigating multiple aspects of fracture behavior such as fracture toughness, work of crack initiation, work of fiber bridging, and material stiffness.
4. Auxiliary laboratory analysis of FR-CPB samples in the form of density progression and SEM imagery in order to support the finding gained through the experimental testing program.

5. Sensitivity analysis of the impacts of induced curing pressure on the fracture behavior of FR-CPB as a method to qualitatively and quantitatively identify the most suitable fracture quantity for the analytical description of fracture initiation in FR-CPB.

## **1.4 Thesis organization**

The arrangement of this thesis is broken down into five chapters. The first chapters, as well as presenting the thesis organization, aids in introducing relevant background information related to the use of FR-CPB, the research gap present in the fracture behavior of FR-CPB under induced curing pressure, and the methodologies implemented in its investigation. Chapter two provides a comprehensive literature review of the effect of induced curing pressure on the multiphysics process occurring in the interfacial transition zone of fiber-reinforced cementitious composites. By presenting the state of current research on cementitious material, it captures a more detailed analysis of findings related to the effects of induced curing pressure. FR-CPB has comparably lower volumes of cement than concrete. The inclusion of multiple forms of cementitious material allows for a well-rounded understanding of behavior. Chapter three details the experimental testing program and methodologies followed in this study, allowing for transparency of data collection methods and replicability of work. Chapter four presents the results of the experimental testing program, auxiliary analysis, and sensitivity index. With reference to the literature review and prior studies, an interpretation and discussion of the results are offered. The fifth and final chapter of this thesis is used to present the most significant conclusions gained from the study. Based on the findings, a reflection of the study and recommendations for further research in the field of research are drawn.

## Chapter 2 Literature review

### 2.1 Introduction

The incorporation of artificial (e.g., carbon, glass, steel) and natural (e.g., wood, hast, leaf) fibers into the mix design of cementitious materials such as concrete [41–43], cemented soils[44–46], or cemented backfill[44–46], has proved a novel means of addressing the tensile and shear induced brittle failure commonly associated with such materials of limited tolerance ability for plastic strain[47-48]. The introduction of a component of greater size to that of the cement grain leads to the formation of a mesoscale interfacial transition zone (ITZ) between component and matrix. As mentioned in Section 1.2. the formation of the ITZ between a larger object such as fiber or aggregate and the bulk matrix is a result of the wall effect leading to an area of loose particle packing and high porosity when compared to that of the bulk matrix[38]. Cementitious composites being highly porosity dependent, the material properties of fiber-reinforced cementitious composites (FRCC) are thus sensitive to changes within the pore structure. As such when a comparison is done between the bulk matrix and fiber matrix interfacial transition zone (FM-ITZ), such as in Table 2-1, the obvious discrepancies between the material properties of each respective area.

**Table 2-1.** Comparison of material properties between FM-ITZ and bulk matrix.

Type of FRCC	Material Properties	FM-ITZ	Bulk matrix	Reference
Polypropylene fiber reinforced concrete	Elastic modulus (GPa)	3.7-45.5	20.1-47.6	[49]
	Hardness (GPa)	0.1-2.3	0.71-2.5	
	Surface roughness value (nm)	146.9-278.5	65.4-98.5	
Polyvinyl alcohol fiber-reinforced concrete	Porosity (%)	27.9-43.8	15.9-28.6	[50]
	Permeability (m <sup>2</sup> )	2.44-8.15 ×10 <sup>-17</sup>	1.23-7.88 ×10 <sup>-21</sup>	[51]
	Elastic modulus (GPa)	37.50±11.32	78.31±14.05	
	Hardness (GPa)	2.46±1.43	10.13 ±3.88	
Steel fiber-reinforced cement mortar	Mean Hardness (GPa)	1.14	1.9	[52]
	Mean creep compliance (GPa <sup>-1</sup> )	0.06	0.03	
Kraft pulp fiber-reinforced cement	Elastic modulus (GPa)	72.7 ± 14.3	17.2 ± 5.6	[53]
	Hardness (GPa)	5.3 ±1.8	0.4 ± 0.2	

Calcium carbonate whisker fiber reinforced cement	Elastic modulus (GPa)	15.3-27.5	29.5-45.3	[54]
	Hardness (GPa)	0.2-1.1	0.8-2.6	
Steel fiber reinforced concrete	Mean tensile strength (MPa)	2.5	2.8	[55]
	Mean fracture energy (kPa/ $\sqrt{m}$ )	109.2	143	
	Mean Poisson's ratio (-)	0.24	0.21	[56]
	Mean elastic modulus (GPa)	94	37.8	
Glass fiber-reinforced cement	Relative hardness (-)	1.53-2.34	1.93-2.49	[57]

Such spatial heterogeneity from FM-ITZ to bulk matrix also indicates the radial anisotropic characteristics of FM-ITZ relative to the fiber surface. Most importantly, the locally heterogeneous and anisotropic characteristics inevitably affect the spatiotemporal distribution of stress and strain (i.e., mechanical process), pore-water pressure (i.e., hydraulic process), temperature (i.e., thermal process), and binder hydration products (i.e., chemical process), and thus result in a more complex thermo-hydro-mechanical-chemical (THMC) process in FM-ITZ. As shown in **Figure 2-1**, the multiphysics processes govern the evolution of material properties and state variables over the full-field domain (including FM-ITZ) of cementitious materials. For instance, it has been found that the formation of FM-ITZ is able to affect the crack propagation patterns in the matrix, and the resultant multi-cracking behavior can enhance the material toughness[58]. The coarse pore structure formed in FM-ITZ affects the local seepage behavior and the heat transfer process[59]. Moreover, it has also been confirmed that the discrepancy of pore water activity between FM-ITZ and bulk matrix affects the formation of hydration products[60]. Because FM-ITZ constituents are the weakest regions in cementitious materials[61], a thorough understanding of multiphysics processes in the mesoscale FM-ITZ plays a key role in the evaluation of the effectiveness of the fiber reinforcement technique.

Moreover, FRCCs are commonly used to produce massive structural elements exposed to various external loadings, which in turn cause an induced curing pressure (see **Figure 2-1**). For example, fiber-reinforced concrete has been widely used to cast columns, foundations, and high dams[62–64]. Because of the limited variability of self-weight[65], the resultant dead load exerts an induced curing pressure and accompanies the construction materials after being placed on site. Moreover, fiber reinforcement has been considered an effective approach to improve the engineering

performance of cemented backfill materials used in underground mines[66-67]. After placement, the backfill materials may experience large confining pressure caused by excavation contraction and high geostress[1,68]. Consequently, the induced curing pressure influences its microstructure and macroscale mechanical response from early to advanced ages. Similarly, the self-weight stress of massive cement-stabilized fiber reinforced soil body also forms the induced confining pressure. The studies[69–71] on the triaxial behavior of fiber-reinforced cemented soils have identified the dependence of stress-strain behavior and volume change on the confining pressure. As such, an increased understanding of the effects of induced curing pressure on the behavior of FRCCs allows for a more comprehensive evaluation of in-situ materials and increased accuracy of engineering design. To achieve such information, the THMC processes (as an internal governing mechanism) function as the key to linking the induced curing pressure (as external loading conditions) to the fiber-matrix interaction (i.e., material behavior) in the ITZ. Although extensive studies have been conducted on FRCCs, the link between induced curing pressure, multiphysics process, and fiber-matrix interaction has not been precisely determined. The objective of this critical literature review is to thus uncover the evolution of THMC processes in the mesoscale FM-ITZ under induced curing pressure, which can form the base for the accurate assessment of fiber reinforcement techniques used in FRCCs.

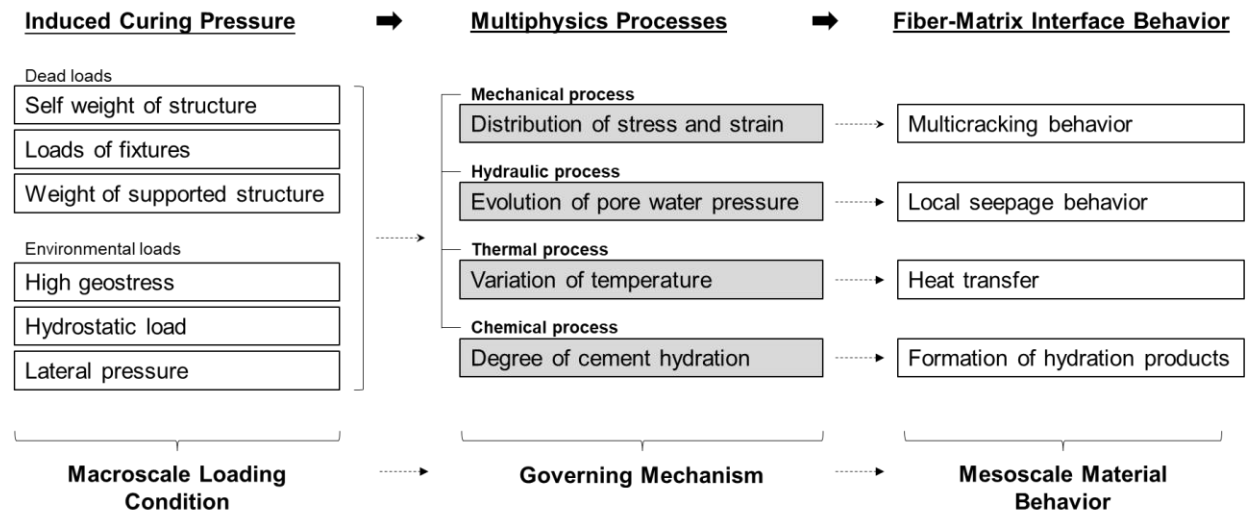


**Figure 2-1.** Correlation among induced curing pressure, multiphysics process, and fiber-matrix interface behavior.

## 2.2 Mechanical process in FM-ITZ under induced curing pressure

As the weak link between fiber and bulk matrix[72], the mechanical process in FM-ITZ governs the extent of local fiber reinforcement and thus affects the macroscale mechanical response of FRCCs[73–75]. For example, it has been widely observed that the macroscale mechanical behavior of FRCCs is sensitive to changes in confining pressure. Figure 2-2 presents the typical triaxial compressive behavior of fiber-reinforced cemented paste backfill (FR-CPB), as previously measured in the laboratory. It can be seen that the FR-CPB shows a highly confining pressure dependency of stress-strain relationship and volume change. It should be noted that, in terms of stress state, the induced curing pressure plays a role similar to the confining pressure and thus inevitably influences the macroscale constitutive behavior as well. However, the measured macroscale experimental data cannot be used to uncover the actual contribution of fiber reinforcement at the mesoscale. Therefore, a good understanding of the mechanical process in FM-ITZ is a prerequisite for the development of an effective fiber reinforcement technique. To this point, this section will discuss the significance of induced pressure on (1) stress state and volumetric deformation and associated changes in microstructure and (2) multi-cracking process in FM-ITZ. The critical discussion on two aspects is able to facilitate the identification of characteristics of mechanical processes in FM-ITZ under induced curing pressure.

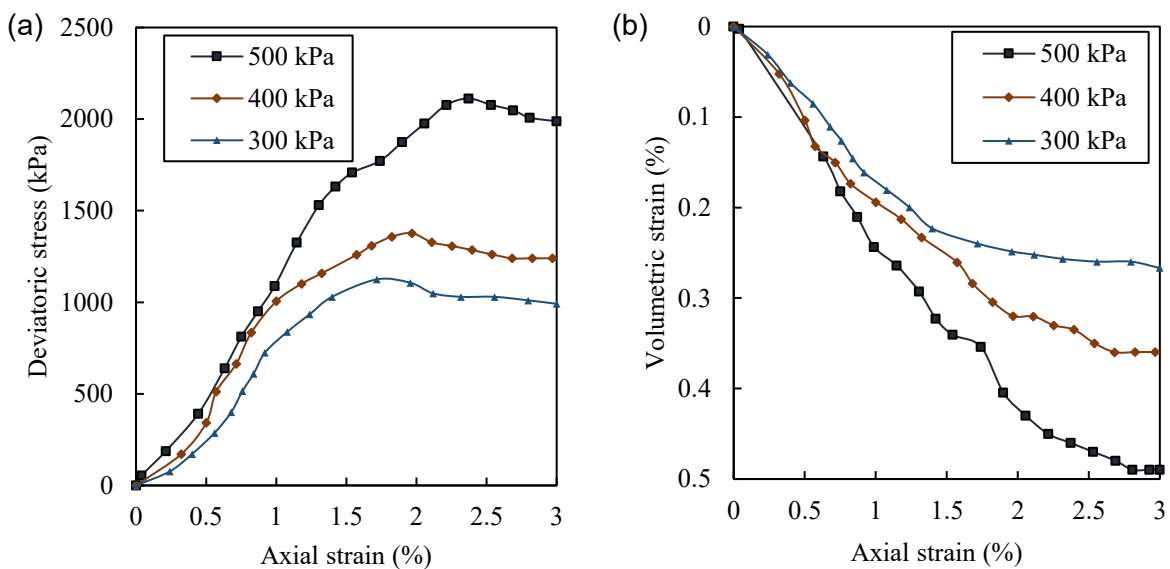


**Figure 2-2.** Confining pressure dependency of triaxial compressive behavior of 90-day polypropylene fiber reinforced cemented paste backfill under consolidated undrained tests: (a) deviatoric stress-axial strain curve and (b) volumetric strain-axial strain curve.

### **2.2.1 Stress State and volume change in FM-ITZ**

First, the pullout load of fiber embedded into the cementitious matrix is dependent on the interfacial contact pressure between the fiber and the surrounding matrix. For example, as shown in 2-3, the peak pull-out response and peak load are sensitive to the interfacial contact pressure due to the interfacial frictional bond strength between fiber and matrix[76-77]. Therefore, when the FRCC mass is exposed to the external confining pressure, the induced curing pressures are expected to increase the interfacial contact force and shear force along the fiber surface[78–83]. Consequently, the induced curing pressure and passively generated interfacial contact pressure form the boundary forces acting on the mesoscale FM-ITZ. It should be noted that such boundary forces can be immediately developed after the fresh cementitious paste is poured into the site, especially for massive structures such as cemented paste backfill (CPB), concrete dam, and cement-stabilized soil slope. Therefore, it is necessary to identify the effect of induced curing pressure on volumetric changes and the stress state of FM-ITZ. For the early-age soft FRCCs, volumetric deformation is closely related to the consolidation process induced by capillary water seepage. For example, the gravitational effect induced upward seepage may cause water accumulation at the top surface of cement-based materials, which has been widely observed in concrete[84], cement paste[85], and CPB[86]. Based on Terzaghi's consolidation theory, self-weight consolidation is able to reduce the porosity of material with weak cohesive bond strength. Therefore, the resultant bulk matrix densification process can be enhanced when the curing pressure is applied to early-age soft cementitious materials[86-87]. It should be pointed out that the denser bulk matrix under induced curing pressure will form an internal restraint boundary condition surrounding the FM-ITZ. Most importantly, as the formation of the hardened matrix, such restraint boundary conditions can form a type of unremovable confining pressure in the FM-ITZ even if the induced curing pressure is released at late ages (e.g., due to the removal of dead load from cementitious materials). Consequently, FM-ITZ, acting as the intermediary, carries such a confining pressure to permanently increase the interfacial contact pressure along the fiber surface. Therefore, the improvement of fiber bridging capacity and the macroscale mechanical properties has been repeatedly observed in FRCCs under curing pressure[88-89].

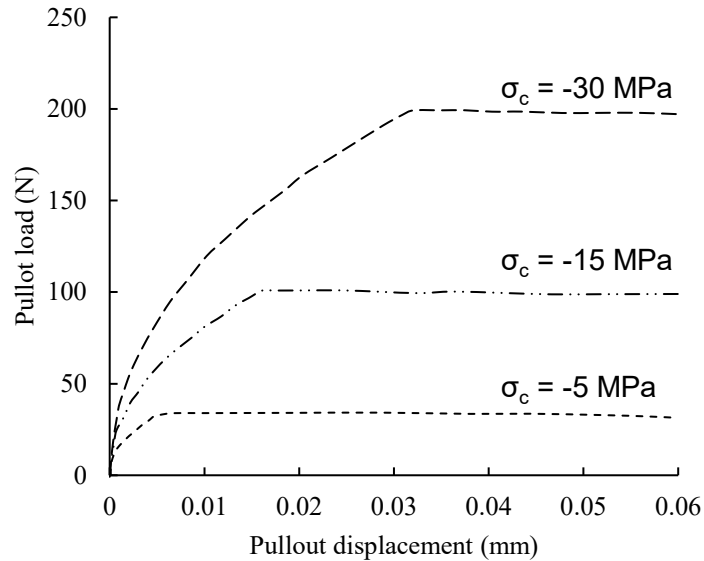


**Figure 2-3.** Effect of interfacial contact pressure,  $\sigma_c$ , on pullout response of stainless fiber embedded into concrete (compressive stress is considered negative)[76].

### 2.2.2 Multicracking behavior in FM-ITZ

Moreover, the induced curing pressure has the potential to contribute to the multiple cracking behaviors in FRCC at late ages. Specifically, the fibers embedded into the cementitious matrix are able to offer a bridging force across the cracks and restrain the microcracking process[88–90]. Such crack arrester role played by fibers inevitably changes the cracking paths in the FM-ITZ and causes the crack deflection and/or branching (see 2-4). Since the open crack surfaces are subjected to biaxial loading conditions, the induced curing pressure may enlarge the difference of principle stresses in the vicinity of the crack surface and thus strengthen the shear or tensile stress concentration. As a result, the induced curing pressure is able to promote the crack deflection and branching in the FM-ITZ. In addition, when fiber slips within the matrix, the Poisson effect may cause excessive contraction of the fibers [90]. However, due to the incompatible mechanical properties such as elastic modulus[91], the deformation from the surrounding matrix cannot compensate for the newly generated interfacial space between fiber and matrix. Therefore, local stress concentration becomes theoretically inevitable along the fiber-matrix interface and thus further contributes to the crack initiation and propagation in the FM-ITZ. The effects of enhanced multi-cracking behavior under induced curing pressure are twofold. First, the fracture process zone ahead of the traction-free crack can be extended, which can toughen the FM-ITZ. Correspondingly, mechanical performance such as the energy dissipation capacity of FRCCs can be improved.

Second, the strengthened multi-cracking process in FM-ITZ also indicates larger unrecoverable deformation formed in the vicinity of crack front region. Therefore, a stronger nonlinear post-cracking response, including hardening/softening behavior and the hysteretic response of FRCC, is expected under induced curing pressure. Furthermore, it is well known that the denser cementitious materials with smaller porosity are commonly featured by desirable engineering performance in practice. Therefore, apart from the stress state and microcracking process in FM-ITZ, it is also of great interest to understand the effect of induced curing pressure on the microstructure of FM-ITZ. In this regard, no published work on the microstructure change of FM-ITZ under induced curing pressure is available in the literature. However, the effect of curing pressure on the aggregate-matrix ITZ has been investigated. For instance, Helmi et al.[92] investigated the effect of curing pressure on the microstructure of reactive powder concrete. In this study, a static pressure of 8 MPa was applied to the fresh concrete samples for 5 hours until demolding. Pressure treatment resulted in an increase in density of 7% and an increase in uniaxial compressive strength of 33%. These results were strongly correlated to the reduction of the overall porosity of the bulk matrix. However, it is of significance to note that this reduction in porosity was not found in aggregate-matrix ITZ, which remained at a constant length. In other words, the induced curing pressure has an unnoticeable effect on the consolidation process in the aggregate-matrix ITZ and thus is unable to directly change the microstructure of ITZ.

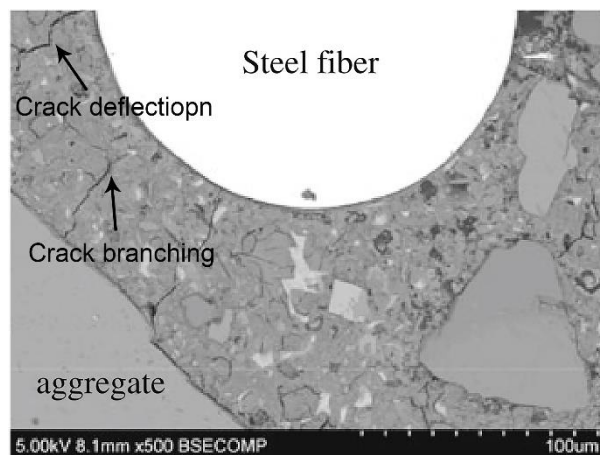


**Figure 2-4.** Crack deflection and branching in FM-ITZ of steel fiber-reinforced mortar[93].

### 2.3 Hydraulic process in FM-ITZ under induced curing pressure

Although the mechanical process, such as the consolidation process, has a limited effect on the microstructure of ITZ, the hydraulic process is able to influence the evolution of the microstructure of ITZ. This is because the hydraulic process is closely related to the migration of chemical ions (e.g., sulfate ions) and the development of pore water pressure in ITZ. Since the seepage process and water retention capacity are porosity-dependent, the formation of FM-ITZ can affect the evolution of pore water content and matric suction in the porous media. Figure 2-5 presents the development of volumetric water content (measured by ECH2O 5TE sensor) and matric suction (measured by TEROS 21 sensor) in FR-CPB over a curing period of 90 days in the authors' laboratory. It can be observed that the inclusion of fibers into the bulk matrix may weaken the development of matric suction (corresponding to a relatively high-water content) at late curing time, which clearly indicates the great importance of identifying the characteristics of the hydraulic process in the ITZ. Correspondingly, the discussion focuses on two aspects, including pore-water seepage and the water retention capacity of FM-ITZ in this section.

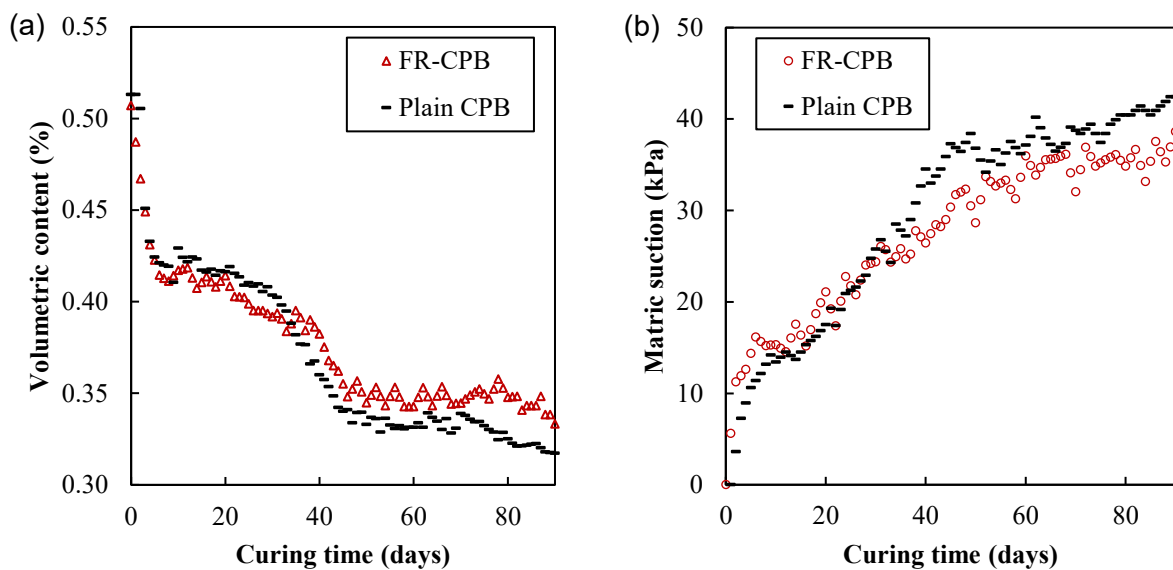
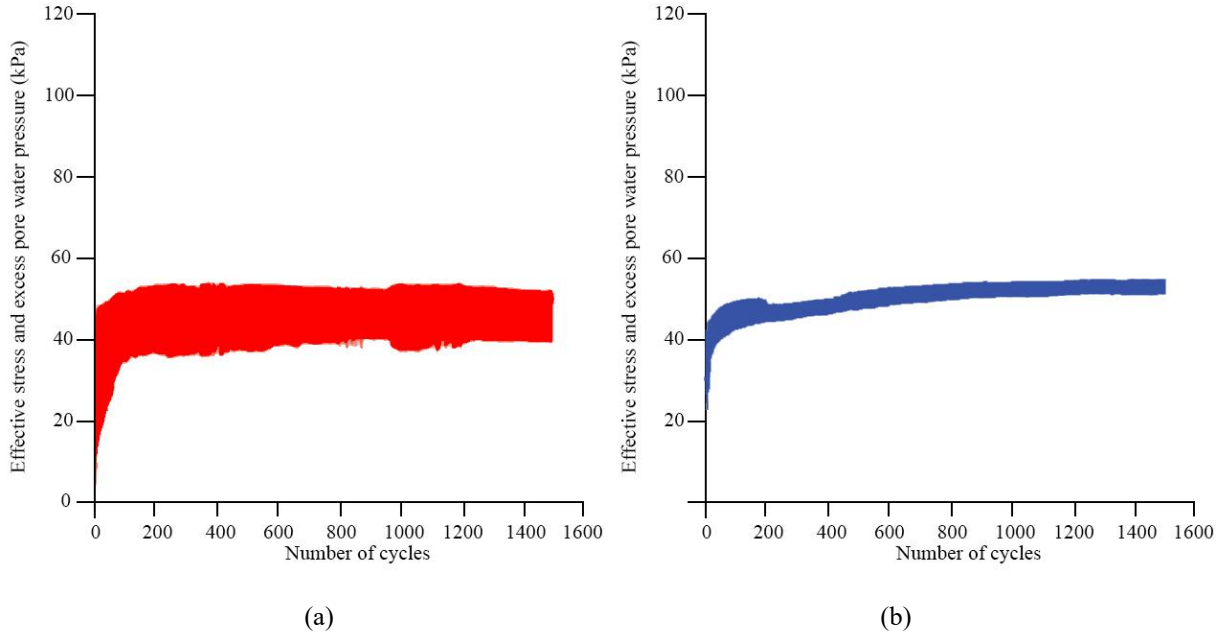


Figure 2-5. Evolution of (a) volumetric water content and (b) matric suction in FR-CPB and plain CPB.

#### 2.3.1 Pore-water seepage behavior in FM-ITZ

For the pore water seepage, the induced curing pressure inevitably interferes with the spatial distribution of hydraulic gradient through its effect on pore water pressure[94]. For example, the rapid placement of massive cementitious materials causes the formation of extremely high self-

weight stress and thus the generation of excess pore water pressure inside the cementitious materials[13,95]. Due to the existence of open boundaries such as top surfaces of cementitious materials, a higher hydraulic gradient can be formed inside cementitious mass and thus strengthen the water seepage[33]. Moreover, due to the considerably high porosity and permeability of ITZ compared with surrounding mortar[38], ITZs become the preferential channels for the strengthened pore-water seepage[96]. The higher hydraulic gradient and larger permeability will increase the seepage velocity in FM-ITZ. The increased seepage velocity can be indirectly confirmed by changes in the dissipation rate of excess pore water pressure in FRCCs. For instance, Festugato et al.[97] studied the excess pore water pressure of fiber-reinforced cemented paste backfill under cyclic loading conditions. As shown in Figure 2-6, the FRCC specimens (see Figure 2-6b) had an excess pore water pressure of around 40 kPa and showed a 27% reduction in excess pore water pressure compared to that (approximately 55 kPa) of the non-reinforced specimens (see Figure 2-6a). The enhanced local seepage in FM-ITZ cannot only affect the evolution of pore water pressure and effective stress, but also has the potential to affect the microstructure of ITZ. This is because the particle segregation process of fresh cementitious materials is commonly accompanied by the upward seepage in cementitious materials. For example, excessive concrete bleeding and water ponding at the surface of cemented paste backfill [98] have been widely observed in practice, which can directly interfere with the uniform distribution of fine particles such as cement grains in the matrix. As a result, the locally progressive loss of cement grains with capillary water seepage will weaken the pore refinement by the hydration products and result in a relatively coarse pore structure[99]. Such coarsening process can be future promoted due to the locally rapid seepage in FM-ITZ. Consequently, strengthened seepage in ITZ under induced curing pressure has the potential to weaken the development of bond strength of ITZ during the very early ages and thereby partially offset the contribution of effective stress to the strength improvement of cementitious materials.



**Figure 2-6.** Excess pore water pressure dissipation in (a) cemented paste backfill and (b) fiber-reinforced cemented paste backfill under cyclic shear loading [97].

### 2.3.1 Evolution of water retention capacity in FM-ITZ

The water drainage associated with pore water seepage contributes to the transition from a fully to partially saturated state inside cementitious materials[4,95]. When the cementitious materials transit into the unsaturated state, the pressure jump (i.e., capillary matrix suction) across the curved air-water interface gradually forms and is balanced by the surface tension of the air-water interface[100-101]. Moreover, the adsorbed water around the particle surfaces and absorbed water inside particles can further contribute to the development of matrix suction in the porous media[102]. For example, Simms and Grabinsky[103] found that a reduction of the volumetric water content of 2% yielded an increase in matrix suction of 80 kPa within CPB materials. Since matrix suction tends to pull the solid skeleton together, the material strength can be improved with the development of matrix suction. Therefore, it is important to evaluate the matrix suction and the associated water retention capacity of granular materials.

Based on the Yong-Laplace equation,  $\Psi=2T_s \cos\alpha/r$  (with surface tension  $T_s$ , contact angle  $\alpha$ , and pore radius  $r$ ), the pore size affects the magnitude of matrix suction and thus the water retention capacity. As discussed in Section 2.2.1, the induced curing pressure is able to cause the discrepancy in the consolidation process in the FM-ITZ and bulk matrix. Therefore, the pore-size dependence of water retention capacity indicates that the induced curing pressure can exaggerate the deficiency

in water retention capacity between bulk matrix and ITZ[104]. The effects of differential water retention capacity are twofold. First, the weaker water retention capacity in the FM-ITZ leads to the additional pore-water migration from FM-ITZ to the bulk matrix and thus further reduces the water content in FM-ITZ. Second, the relatively low water content in ITZ under induced curing pressure directly affects the contribution of matric suction to the material strength. This is because matric suction is developed through surface tension along the air-water interface. When the water content decreases, the contact area between pore water and solid particles is reduced accordingly. Correspondingly, the developed matric suction only acts on the limited surfaces of solid particles (see Figure 2-7). As a result, the lower water content weakens the contribution of matric suction to the material strength in FM-ITZ compared with the counterpart in the bulk matrix under induced curing pressure. Therefore, it is of great importance to incorporate the water retention capacity into the evaluation of the material strength of FRCC under induced curing pressure, especially for cementitious materials with low cement content. This is because the matric suction and cohesion are more comparable in soft FRCC with low cement content. For instance, the cohesion of 28-day CPB with a cement content of 4.5% is commonly in a range of 150 to 250 kPa[105], while the matric suction can reach up to 100 kPa in the 28-day CPB materials[106]. Therefore, the matric suction plays a critical role in improving the materials strength of FRCC under the induced curing pressure.

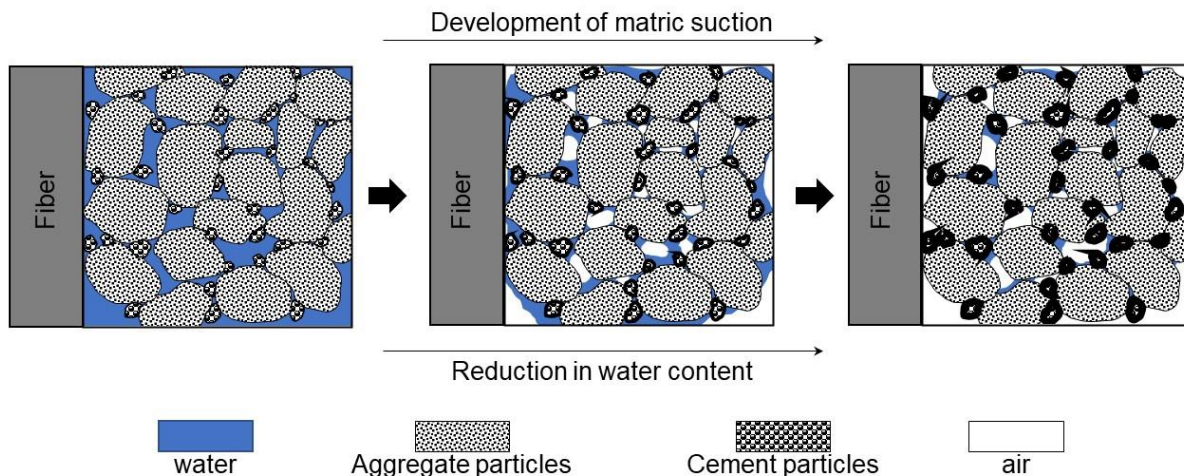


**Figure 2-7.** Evolution of matric suction and water content in FRCC.

## 2.4 Thermal process in FM-ITZ under induced curing pressure

After placement into the pour site, a complex thermal process occurs in FRCC under the field thermal loading conditions. The internal temperature evolves with heat conduction by a local temperature gradient, heat advection by the pore-water seepage, and heat generation by the binder hydration[107]. The evolution of temperature and subsequent temperature gradient formed between components of cementitious material is of great significance to the development of internal stresses acting on its microstructure[108–111]. As the weakest link between fiber and bulk matrix, FR-ITZ is more susceptible to the resultant thermal deformation. Correspondingly, the thermal incompatibility of different constituents of FR-ITZ may result in the cracking at the mesoscale and thus macroscale damage, which eventually adversely affects the mechanical performance of FRCC. Therefore, the discussion in this section will provide an insight into the evolution of the heat transfer process and thermal deformation of FR-ITZ under induced curing pressure.

### 2.4.1 Heat Transfer in FM-ITZ

The evolution of temperature in FM-ITZ is governed by heat conduction, heat advection, and heat generation. Therefore, it is necessary to identify the evolution characteristics of each contributor. The convective heat transfer process is driven by the migration of pore fluid, including capillary water and pore air. The characteristics of seepage behavior in FM-ITZ have been discussed in Section 2.3.1. This section will focus on the conductive heat transfer process and heat generation in the FM-ITZ under induced curing pressure. For the conductive heat transfer process, Fourier's law ( $q=-K_T \nabla T$  with  $q$  heat flux ( $W/m^2$ ),  $K_T$  thermal conductivity ( $W/mK$ ), and  $T$  temperature (K)) is widely adopted to analytically describe the evolution of heat flux by the local gradient of temperature. In terms of thermal properties, thermal conductivity is a porosity- and saturation-dependent quantity which is affected by the composition and mutual configuration of each individual component in the multiphase porous media[112]. During early ages, the thermal conductivity of fully saturated FMCC depends only on the solid phase and liquid phase. As discussed in Section 2.2.1, the primary consolidation due to the water seepage mainly occurs in the bulk matrix and has very limited influence on the microstructure of FM-ITZ. Consequently, the induced curing pressure will further enlarge the discrepancy in the microstructure of the bulk matrix and FM-ITZ and result in substantial changes in the porosity-dependent thermal

conductivity in the bulk matrix. Since the thickness of FM-ITZ is commonly in the range of 20 $\mu$ m to 100 $\mu$ m[39,55-56], a steep gradient of temperature difference is expected in the FM-ITZ to maintain the local thermal equilibrium, which not only complexifies the conductive heat transfer process, but also drives the further development of thermal deformation in this weak and narrow zone under induced curing pressure.

Moreover, when the FMCC transfers into a partially saturated state at the advanced ages, a dramatic decrease in the apparent thermal conductivity has been widely measured in FMCC (see Figure 2-8). This is because the thermal conductivity of pore air is approximately one order of magnitude smaller than that of pore water[113]. The increased pore air content reduces the magnitude of apparent thermal conductivity of the FRCC and thus retard the conductive heat transfer in the unsaturated porous media. Since the induced curing pressure is able to exaggerate the difference in water retention capacity between FM-ITZ and bulk matrix[104], additional water displacement will occur from FM-ITZ to bulk matrix. Consequently, lower water content is expected in FM-ITZ under induced curing pressure. As a result, the induced curing pressure can further reduce the thermal conductivity of FM-ITZ relative to that of the bulk matrix, which indicates an enhanced temperature gradient between FM-ITZ and the bulk matrix.

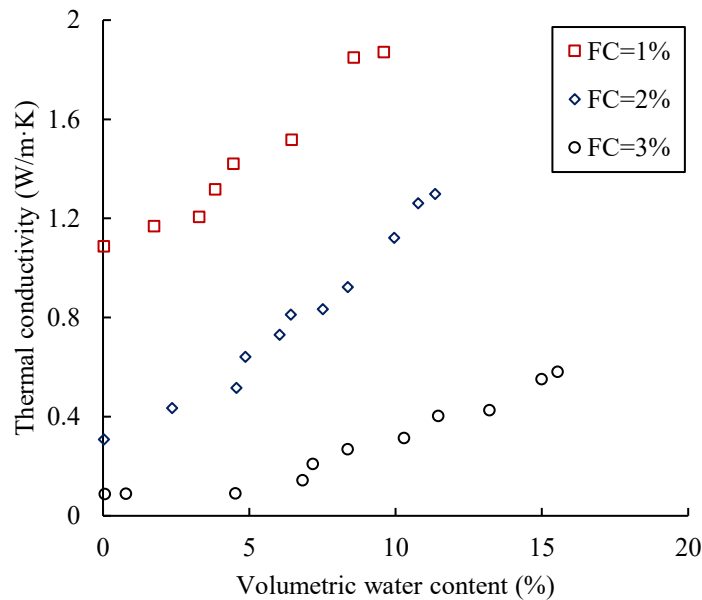


**Figure 2-8.** Dependence of thermal conductivity on the volumetric water content in FRCC (FC: fiber weight content w.r.t. the total weight of solid phase)[114].

Cement hydration is an exothermic chemical reaction process. After mixing with water, the major clinker phases of cement, viz. tricalcium aluminate ( $C_3A$ ), tricalcium silicate ( $C_3S$ ), dicalcium silicate ( $C_2S$ ), and tetracalcium aluminoferrite ( $C_4AF$ ), demonstrate different hydration rates[115], [116], which are accompanied by the release of a substantial amount of heat energy. More precisely, the  $C_3S$ ,  $C_2S$ , and  $C_4AF$  are able to release approximately 259-502 kJ/kg of heat, while  $C_3A$  can release around 865 kJ/kg[117]. Several studies[118–120] on cement hydration have reported that the hydration rate is sensitive to changes in curing pressure. As shown in Figure 2-9, the curing pressure is able to increase the hydration rate at a given curing time. This is because the curing pressure can induce the formation of microcrack at the interface between an unhydrated cement particle and hydrated cement matrix, especially in the early-age weak cement paste[121]. Consequently, the resultant microcrack will enhance the capillary water diffusion from hydrated to unhydrated cemented particles and, thereby, the hydration rate. Correspondingly, a proportional increase in heat generation can be obtained from cement hydration under induced curing pressure. Due to rapid cement hydration during the early ages, the enhanced heat generation under induced curing pressure will further strengthen the change in the temperature gradient with curing time, which inevitably contributes to the thermal deformation in the FM-ITZ. A detailed discussion on the thermal deformation in FM-ITZ under induced curing pressure will be presented in Section 2.4.2.

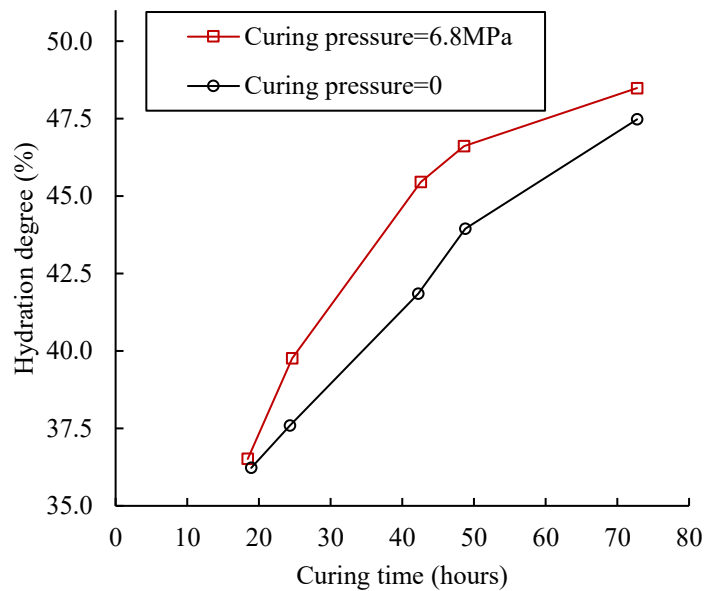


**Figure 2-9.** Dependence of cement hydration rate on curing pressure[120].

#### 2.4.2 Thermal deformation in FM-ITZ

The thermal deformation  $\varepsilon_T$  can be determined by the product of the coefficient of thermal expansion (CTE) and temperature gradient  $\nabla T$ . As discussed in Section 2.4.1, to maintain the local thermal equilibrium, a steeper temperature gradient develops between FM-ITZ and bulk matrix under induced curing pressure and thus further enlarges thermal deformation in the FM-ITZ. However, the difference in CTE of constituents of FMCC will lead to strong thermal incompatibility. In this regard, it should be pointed out the structure of hydrated cement is highly complex and composed of capillary pores in which water molecules can be located[122]. However, the water confined in the micro- and meso-pores of hydration products exhibits considerably high CTE compared with bulk water[123]. For example, as shown in Figure 2-10, the recent experimental studies [124-125] show that the thermal expansion of confined water increases with the reduction in the pore size and thus indicates an increased CTE of confined water in smaller capillary pores. In addition, as shown in Table 2.2, the solid constituents (i.e., aggregates, fibers, unhydrated cement particles, and hydration products) of FMCC also possess different CTE and thereby further exaggerate the thermal incompatibility between different solid phases. Consequently, the steeper temperature gradient in FM-ITZ will lead to a larger thermal deformation in the hardened hydration products such as C-S-H. Due to the critical bonding role played by the hydration products, the differential thermal deformation, and associated microcracks inevitably cause structural damage to the hydration products and thus the material degradation. Moreover, compared with material degradation in the bulk matrix, the thermal deformation-induced microcracks are able to impose more severe damage to the cohesive strength in the weak FM-ITZ, and influence the effectiveness of fiber reinforcement at the macroscale.

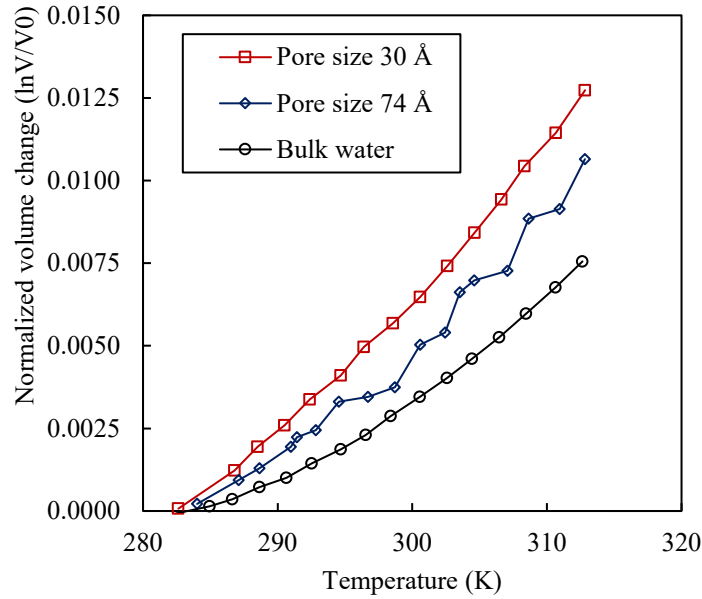


**Figure 2-10.** Dependence of thermal expansion of confined water on pore size[125].

**Table 2-2** Summary of porosity- and saturation-dependent models for thermal conductivity of porous media.

Constituent of FRCC	Coefficient of thermal expansion ( $10^{-6}/K$ )	Thermal conductivity (W/mK)
<i>Aggregate</i>		
Quartz	12.6 [126]	7.7-8.4 [127]
River gravel	12.51 [128]	0.55 [129]
Granite	5.60-9.5 [130]	3.247 [131]
Limestone	2.8-5.52 [132]	2.955-3.792 [133]
Sand	0.32-0.43 [134]	0.3-0.8 [134]
<i>Binder agent</i>		
Cement paste	10-27 [110]	0.8-1.2 [135]
CSH	42-99.1 [136-137]	0.98 [136]
CH	45-70 [134,138]	1.32 [139]
<i>Fiber</i>		
Synthetic fiber	70-100 [140-141]	0.22-0.31 [142-143]
Steel fiber	12-36 [144-145]	53 [146]
Natural fiber	22-45 [147]	0.0341-0.0599 [148]
<i>Pore fluid</i>		
Confined water	70-200 [149]	0.25-1.25 [150]
Pore air	2,500 [151]	0.026 [152]

## **2.5 Chemical process in FM-ITZ under induced curing pressure**

The evolutive strength of FMCC plays a critical role in their engineering performance during the service life, which is dominated by the progress of cement hydration. Correspondingly, it is necessary to identify the effect of induced curing pressure on cement hydration. The hydration of cement particles begins with the nucleation and growth of hydrates on the surface of the particle and continues until the surface of the particle is fully enveloped. It is well known that cement hydration kinetics are strongly dependent on the moisture diffusion through the gel pores of hydration products[87,153-154]. Correspondingly, the discussion on the effect of the induced current pressure on the integrated diffusion-reaction process can facilitate the identification of characteristics of cement hydration kinetics (Section 2.5.1) and hydration products (Section 2.5.2) in FM-ITZ.

### **2.5.1 Cement hydration kinetics in FM-ITZ**

For cement hydration, the chemical compositions of cement mainly consist of four different clinker phases, including  $C_3S$ ,  $C_2S$ ,  $C_3A$ , and  $C_4AF$ . Previous experimental studies [116,155-156] found that these four major clinker phases react with water at different rates. Most importantly, experimental studies have confirmed the sensitivity of cement hydration kinetics to curing pressure[87,157]. However, it is still unclear whether the individual constituent phase hydrates independently or at equal fraction rates. Consequently, it is generally accepted that the overall hydration progress is approximated by a degree of hydration. Extensive studies have been conducted to describe the hydration process analytically. The typical microscopic and macroscopic models for cement hydration have been summarized in Table 2-3 The proposed models have been used to characterize the effects of chemical composition[158], mixing parameters such as water-to-cement ratio [159] , and external curing conditions such as curing temperature[160]. Meanwhile, these cement hydration models can also be integrated into the multiphysics modeling for cementitious materials[107,161–164]. A detailed discussion on the cement hydration models has been presented in previous publications[164–166].

**Table 2-3.** Typical cement hydration models.

Group	Typical models	Remarks
Microscopic models	Jennings-Johnson model [167]	Aimed to capture the actual chemical process.
	CEMHYD3D model [160]	
	HYMOSTRUC model [168]	The chemical, physical, and mechanical characteristics of cement hydration are required in the modeling process.
	HydratiCA model [159]	
Macroscopic models	Knudsen model [169]	Established based on the macroscale experimental observation and thus belong to empirical models.
	HSTA model [170]	
	CFOP model [171]	
	Schindler-Folliard model [158]	Evaluate the overall degree of cement hydration.
	Bentz model [172]	

However, relatively limited models were developed to capture the effect of curing pressure on the cement hydration kinetics. The present studies mainly focus on the experimental investigation of the dependence of cement hydration on the curing pressure. For instance, Bresson et al.[119] identified that the extent of hydration reaction of cement and  $C_3S$  can be significantly different when the curing pressure is applied, especially at early ages. Moreover, Zhang et al.[173] utilized an ultrasonic cement analyzer to analyze the hydration kinetics and found that the increased pressure facilitates the ingress of water into the specimen and thereby accelerates the cement hydration (see Figure 2-11). Consistent results have also been observed in other studies[174–176]. In terms of a quantitative assessment of the effect of curing pressure, several mathematical models were proposed to predict the cement hydration under isothermal and isobaric curing conditions. For example, Pang et al.[177] incorporated a scale factor into the Arrhenius equation to capture the dependence of cement hydration kinetics on curing temperature and pressure.

$$\frac{\partial \xi}{\partial t} = C_1 \exp \left[ \frac{\Delta V}{RT} (P_r - P) + \frac{E_a}{R} \left( \frac{1}{T_r} - \frac{1}{T} \right) + C_2 \xi \right] \sin(\pi \xi^{C_3})^{C_4} \quad (2-1)$$

where  $\xi$  is dimensionless hydration degree,  $t$  is curing time (s),  $C_i$  ( $i=1$  to  $4$ ) are fitted constants,  $E_a$  denotes the apparent activation energy (J/mol),  $\Delta V$  is the apparent activation volume ( $\text{m}^3/\text{mol}$ ),  $R$  is the gas constant ( $8.314 \text{ J/mol}\cdot\text{K}$ ),  $T_r$  and  $T$  are a reference and actual curing temperature (K),  $P_r$  and  $P$  are a reference and actual curing pressure (Pa). For Eq. (2-1), it should be noted that the curing pressure and temperature are explicitly assumed to play similar roles in the progression of cement hydration. Moreover, according to the predicted results from Eq. (2-1), it was found that the effect of curing pressure on the cement hydration kinetics is weaker than that of curing temperature, which is consistent with the experimental findings[178]. For example, Scherer et al.[179] reported that a pressure change of 3.7 MPa is approximately equivalent to a temperature change of  $1^\circ\text{C}$ , in terms of its effects on the rate of cement hydration. Due to the high predictability of the combined effect of curing pressure and temperature, Eq. (2-1) has been widely used in the field of oil-well cement under complex field loading conditions[177–180].

The mechanisms governing the improvement of hydration kinetics under curing pressure are trifold. First, the diffusion of water through the gel pores of hydration products such as Calcium Silicates Hydrates (CSH) is driven by the pore humidity or chemical potential gradient between the exterior of the CSH shell and interior anhydrous cement particles through the gel pores[181]. Prior to the formation of a completely enveloped shell, the rapid initial hydration draws water from capillary pores creating nano-scale globules of CSH on the surface of the anhydrous cement grain[182]. Since induced curing pressure is able to increase the hydraulic gradient in ITZ, the accelerated inward transport of pore water pressure promotes the extent of hydration at interfaces between hydrated and anhydrous cement grains. Second, apart from the direct enhancement of water diffusion through the capillary pores of hydration products, it has also been found that capillary pressure affects the pore water activity, which is defined as the change in the chemical potential of liquid water from its pure state. It has been confirmed that the rate of cement hydration is dependent on pore water activity. The relationship between pore water activity  $a_H$  and pore water pressure  $P$  is given by Flatt et al.[60] :

$$\alpha_H = RH \exp \left[ -\frac{\bar{V}_H (P - P_r)}{RT} \right] \quad (2-2)$$

where RH is the relative humidity in the porous media (%),  $\bar{V}_H$  is the molar volume change of pore water in the cement hydration ( $\text{cm}^3/\text{mole}$ ), P is water pressure (MPa), and  $P_r$  is a reference pressure (MPa) above which condensation in a reservoir of bulk pure water will occur at the same temperature, R refers to the ideal gas constant ( $8.3145\text{J/mol}\cdot\text{K}$ ), and T is the temperature (K). It should be noted that the dependence of water activity on the capillary pressure plays a more important role in the unsaturated cementitious materials. As discussed in section 2.3, the transition of FRCC from a fully to partially saturated state leads to the development of negative pore pressure. However, the induced curing pressure results in less negative pore pressure in the porous matrix, which in turn weakens the reduction in the water activity and maintains the continuous cement hydration at advanced ages. For example, without consideration of induced pressure, it has been reported that cement hydration stops below 80% relative humidity associated with a more negative pore water pressure [183-184]. Such findings clearly indicate the critical role played by a less negative pore water pressure under induced curing pressure. Third, as shown in Figure 2-12, the microcracking process can be promoted under applied curing pressure [120] and thus form the accessible channels between hydrated, partially hydrated, and anhydrous cement. Consequently, the resultant microcracks in the cement matrix are able to enhance the pore-water migration and improve the contact between pore water and anhydrous cement. Therefore, due to the combined effect of the hydraulic gradient in ITZ, pore-water activity, and microcracking process, accelerated cement hydration can be expected under high curing pressure.

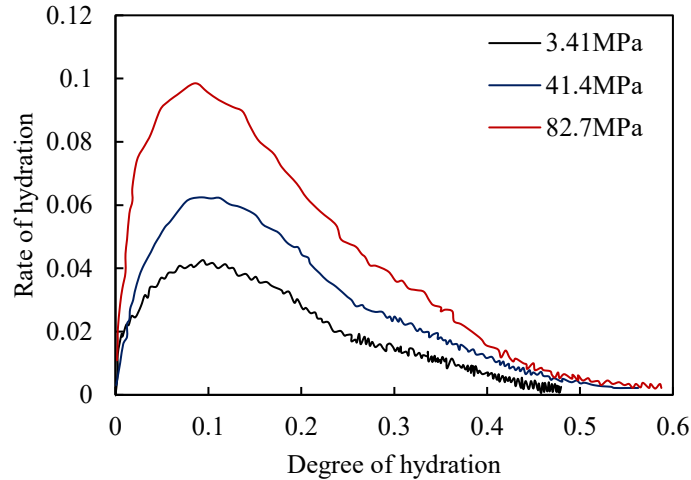


Figure 2-11. Dependence of cement hydration on curing pressure at 38°C [173].

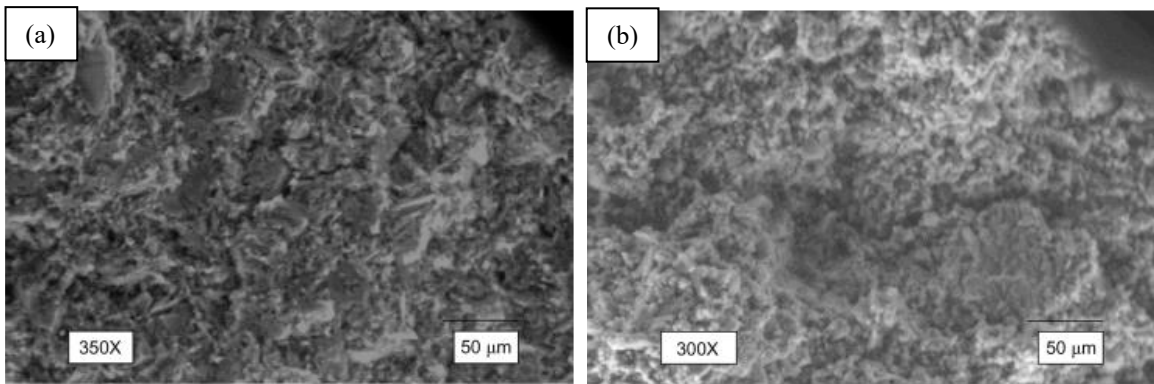


Figure 2-12. Microcracking in  $C_3S$  matrix under a stress of 6.8MPa after 18-hour hydration (a) 350x (b) 300x [120].

### 2.5.1 Hydration products in FM-ITZ

As uncovered by previous experimental studies, the mesoscale FM-ITZ possesses a very limited thickness relative to the solid surface of fibers in the matrix. Correspondingly, the microstructure development in FM-ITZ is expected to be sensitive to the changes in curing conditions, including the induced curing pressure. The direct influence of induced curing pressure on the microstructure of FM-ITZ has been discussed in Section 2.3. It has been found the induced curing pressure has an unnoticeable effect on the consolidation process in the ITZ. As a result, the solid particles are unable to bind intimately with the relatively large solid surface of fibers due to the wall effect[185]. For instance, the thickness of ITZ in reactive powder concrete shows an insignificant reduction from 17.3 $\mu\text{m}$  to 16.9 $\mu\text{m}$  when curing pressure changes from 0 to 8MPa [92]. Therefore, the

induced pressure has a weak influence on the microstructure of FM-ITZ in terms of thickness and porosity. However, as discussed in Section 2.55.2, the induced curing pressure is able to influence the hydration rate and thus the formation of hydration products in FM-ITZ. More precisely, the induced curing pressure can enhance the hydration rate and thus generate more hydration products in FM-ITZ at a given curing time, which further contributes to the interfacial bond strength between fiber and solid particles. Therefore, a stronger and stiffer FM-ITZ with unnoticeable change in porosity and thickness will be developed under the induced curing pressure.

Moreover, the induced curing pressure is able to interfere with the microstructure of hydration products as well. Specifically, as the key contributor to the mechanical strength of cementitious materials, CSH is the dominant hydrate formed in the pozzolanic reaction and can be further distinguished into high-density (HD) and low-density (LD) CSH phases [186], which have been recognized as two structurally distinct but compositionally similar CSH phases[187]. Multiple advanced characterization techniques, including atomic force microscopy[188], small angle neutron scattering[189], and transmission electron microscopy (TEM)[190], have been utilized to investigate the microstructure of CSH. For instance, the distinctive morphology of HD CSH and LD CSH can be clearly observed by the TEM image (see Figure 2-13). This HD CSH has greater mechanical strength that can be linked to the higher packing density of the hydrate[191] and thus positively contribute to the improvement of material engineering performance[192-193]. Most importantly, there exists a correlation between the production of HD CSH and curing pressure. For example, Kim et al.[194] have reported that increased curing pressure may lead to a higher order of silicate polymerization of CSH and thus greater production of HD CSH. More specifically, they have found the degrees of connectivity of the hardened cement hydrates increase by 13% when curing pressure increases from 0.1MPa to 10MPa. Therefore, the induced curing pressure not only facilitate the generation of more hydration products at a given curing time but also improve the quality of hydration product through the enrichment of HD CSH in the FM-ITZ.

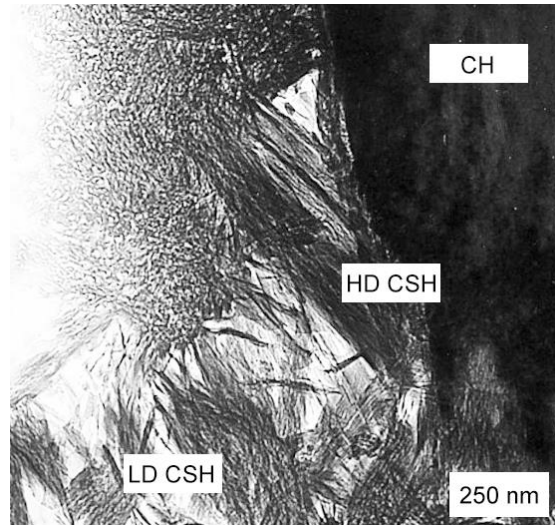


**Figure 2-13.** TEM image of LD CSH and HD CSH in a mature C3S paste (CH: calcium hydroxide)[195].

However, the induced curing pressure can also impose a deleterious effect on the formation of hydration products. This is because, compared with the bulk matrix, the resultant larger porosity indicates higher water content and water-to-cement ratio exist in the FM-ITZ. Consequently, more large crystals such as CH and expansive phases such as ettringite (Aft) can be generated in the large pore space of FM-ITZ [186-187]. However, as discussed in Section 2.3, the induced curing pressure is able to strengthen the pore-water seepage in the FM-ITZ, which may cause not only a relatively low water content but also a progressive loss of fine cement particles. Consequently, induced curing pressure also has a tendency to weaken the formation of hydration products in the ITZ. Such adverse effects associated with induced curing pressure can be further enhanced in the soft cementitious materials with high water content, such as CPB materials. The positive and deleterious effects of induced curing pressure on the production of hydration products clearly indicate the multiphysics processes must be fully considered and evaluated for the assessment of the critical role played by FM-ITZ and the effectiveness of fiber reinforcement technique.

## **2.6 Discussion of the effects of induced curing pressure on the FM-ITZ**

Although experimental investigation can improve the understanding of the mesoscale response of FM-ITZ, advanced quantitative analysis tools are required for successful engineering implementation of fiber reinforcement techniques in practice. In this regard, due to the complexity of multiphysics processes, the mathematical modeling approach can be used as an effective means. The macroscale multiphysics modeling for the fiber-reinforced matrix has been subject to

extensive research, and the relevant work has been summarized in the previous literature review[196-197]. However, the macroscopically homogeneous materials are commonly assumed by the macroscale modeling for the composite materials, which is invalid for the mesoscale FM-ITZ. This is because FMCC comprises spatially different material compositions and structures in the mesoscale FM-ITZ and thereby results in gradually varying material properties. As a result, the reliability of a robust multiphysics modeling tool depends on the prediction accuracy of spatial variability in FM-ITZ. Two fundamental aspects, including geometric and material heterogeneity, must be evaluated for the consideration of inhomogeneities in FM-ITZ. The geometric heterogeneity is mainly related to geometric properties of constitutional phases. For the solid phase, due to the dependence of pore size on particle size, the particle size distribution can be used as a key to capture the particle size-induced heterogeneity. For the fluid phases, the interaction between liquid pore water and gaseous pore air and their contribution to the solid phase can be characterized by the water retention curve. Most importantly, the water retention capability is sensitive to the changes in particle size. Therefore, the particle size distribution and water retention curves associated with FM-ITZ can provide valuable information for the characterization of the inhomogeneity in FM-ITZ.

Moreover, to evaluate the in-situ engineering performance of FMCC, the external loading conditions and internal governing mechanisms must be fully considered. Most importantly, couplings among different multiphysics processes result in a more complex material response in FM-ITZ under induced curing pressure. For the mechanical process, the mechanical deformation, such as the multicracking process in FM-ITZ, affects the porosity-dependent material properties, including hydraulic conductivity and thermal conductivity. Consequently, the pore-water seepage and heat transfer in FM-ITZ inevitably demonstrate the dependence on the mechanical process, which causes the associated evolution of pore-water pressure and temperature in the FM-ITZ. For the hydraulic process, the pore water pressure changes are respectively related to the magnitude of effective stress and matric suction in fully and partially saturated FMCC and thus influence the mechanical process. Moreover, the seepage process also governs the heat advection in the FM-ITZ. In addition, the moisture content changes induced by the seepage process affect the progression of cement hydration in FM-ITZ. For the thermal process, the heat transfer process causes the temperature evolution and influences the temperature-dependent cement hydration rate. Meanwhile, the difference in CTE of constituents of FMCC leads to the strong thermal

incompatibility between different solid phases, and the resultant thermal deformation directly affects the mechanical response of the FMCC. For the chemical process, cement hydration plays a critical role in the development of material strength, and the exothermic hydration process is able to interfere with the evolution of temperature in FM-ITZ as well. In addition, the chemical reaction consumes the pore water and thus causes water pressure dissipation. Therefore, the coupling among different multiphysics processes must be fully considered to evaluate the mesoscale response of FM-ITZ under induced curing pressure.

The engineering application of advanced mathematical tools depends on their predictability. Therefore, extensive experimental data, including the mesoscale material response and material properties, are required for the model validation. In terms of mesoscale measurements associated with FM-ITZ, advanced experimental instruments have been developed. For the mechanical process, the indentation technique has been widely adopted to evaluate the mesoscale load-displacement behavior and properties (e.g., hardness and Yong's modulus) of ITZ. Moreover, the 2D and 3D digital image (or volume) correlation technique has been successfully employed to measure full-field deformation. For the hydraulic process, the small length scale and multiphase flow associated with unsaturated FRCC lead to the challenge of measuring pore-scale seepage behavior. Correspondingly, the experimental microfluidic investigations can be considered a promising approach to capturing the real-time dynamics of pore-scale flow and transport. Since the microfluidic devices have been successfully used to investigate flow and transport in porous media[198-199], this visualization technique has the potential for the characterization of mesoscale seepage behavior in the FM-ITZ. For the thermal process, the measurement of mesoscale real-time spatial thermal distribution and its evolution over time has been a challenging task. In this regard, the micro/nano-meter thermal sensor (e.g., electrical and fluorescent thermal sensors) can be used to measure the local temperature at the mesoscale[200], while infrared thermometry has been used as an effective real-time spatial temperature imaging technique. For the chemical process, enormous techniques have been developed to characterize the cement hydration process, such as synchrotron X-ray diffraction tomography[201], nuclear magnetic resonance spectroscopy[202], and scanning electron microscopy[203].

Since the limitation of computing power imposes the bottleneck on the engineering application of mesoscale models into the field scale project, an accurate 3D spatial depiction of massive FRCC

through mesoscale models is generally not affordable at the scale of interest of most real projects nowadays. Unavoidably, upscaling techniques and the associated multiscale modeling approaches have been routinely used to calculate the homogenized model parameters and reduce the numerical effort and memory demand for the numerical analysis. The multiscale modeling approach is incredibly powerful and allows us to thoroughly probe the multiphysics process at a smaller scale and seamlessly integrate the governing mechanisms at the macroscale to evaluate the response of the overall system. Consequently, the multiscale modeling approach has been widely applied to a broad range of scientific and engineering problems[204]. Systematic literature reviews on multiscale modeling have been performed in previous studies[205–208]. However, it should be pointed out the fundamental reason for using the multiscale modeling approach is the present availability of computational power. With the increasing computing power, the multiscale modeling technique is expected to play a weaker role in the quantitative analysis of FRCC materials in the future.

## **2.7 Conclusions from Literature Review**

As the weakest region in cementitious materials, the mesoscale FM-ITZ under induced curing pressure plays a key role in the effectiveness of the fiber reinforcement technique. Therefore, extensive studies have been conducted to identify the influential factors and associated governing mechanisms responsible for the development of FM-ITZ. Based on the present critical review of the multiphysics process in FM-ITZ, it has been found the complex thermo-hydro-mechanical-chemical processes occur simultaneously and govern the material response inside the FM-ITZ. Following conclusions can be made based on the review.

- (1) For the mechanical process, the induced curing pressure is able to strengthen seepage in ITZ and has the potential to weaken the development of bond strength of ITZ during the very early ages, thereby partially offsetting the contribution of effective stress to the strength improvement of cementitious materials.
- (2) An enhanced densification process can be formed in the bulk matrix under induced curing pressure and therefore form a locked confining pressure boundary condition around the FM-ITZ. The resultant changes in a stress state and enhanced multicracking behavior can further toughen the FM-ITZ.

- (3) For the hydraulic process, strengthened seepage in FM-ITZ under induced curing pressure has the potential to weaken the development of bond strength of ITZ during the very early ages and thereby partially offset the contribution of effective stress to the strength improvement of cementitious materials.
- (4) The induced curing pressure is able to cause the discrepancy of the consolidation process between FM-ITZ and bulk matrix. As a result, the pore-size dependence of water retention capacity further exaggerates the deficiency in water retention capacity between bulk matrix and ITZ under induced curing pressure.
- (5) For the thermal process, the induced curing pressure can cause a steeper temperature gradient in the saturated and unsaturated FM-ITZ and thus influence the heat transfer process and temperature evolution in FM-ITZ.
- (6) Due to the different CTE of confined water and solid constituents of FMCC, the thermal incompatibility further contributes to the formation of microcracks in FM-ITZ under induced curing pressure and thus affects the effectiveness of fiber reinforcement.
- (7) For the chemical process, the induced curing pressure is able to enhance hydration kinetics due to the combined effects of the hydraulic gradient in ITZ, pore-water activity, and microcracking process. However, compared with the effect of curing pressure, the influence of induced curing pressure on the hydration rate is weaker.
- (8) Due to the dependence of cement hydration on curing pressure, more hydration products (especially the HD CSH) can be formed in FM-ITZ. However, the enhanced seepage behavior can also weaken the formation of hydration products in ITZ under induced curing pressure.

## Chapter 3 Experimental testing program

### 3.1 Materials

The materials used in the batching of the CPB and FR-CPB samples consisted of Portland Cement Type 1 (PCI), tap water, ground silica tailings, and 12mm polypropylene fibers. Ground silica tailings were chosen over that of tailing sourced from the industry as the material provided chemical stability not available in that of natural tailings. Tailings sourced from industry will contain varying levels of sulfides along with other chemicals allowing for variability in hydration products. To ensure replicability between tests, an artificial non-acid generating material was required. With much of Canadian hard rock mining being quartz-based, ground silica was chosen as its representative. Figure 3-1 presents a particle size distribution for the ground silica material. The calculated coefficients of uniformity and curvature are listed in Table 3-1. The polypropylene fibers used in testing were sourced from the Euclid Chemical group. The properties of the fibers are summarized in Table 3-2.

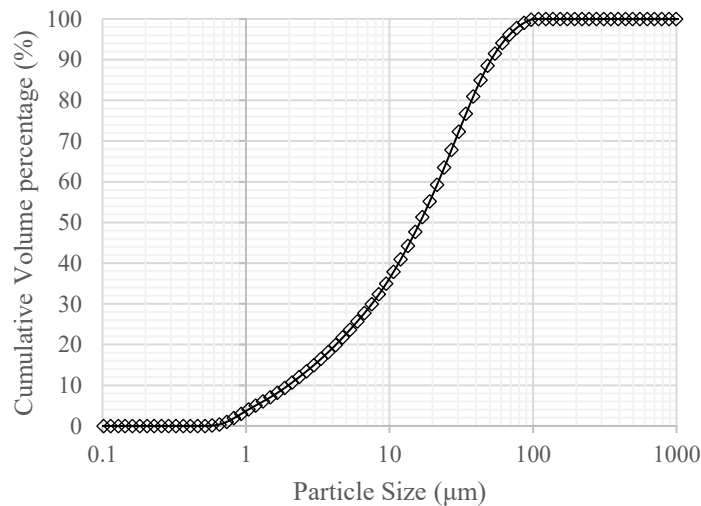


**Figure 3-1** Particle Size Distribution.

**Table 3-1** Grade Curve Characteristics.

D10 (µm)	D30 (µm)	D60 (µm)	Cu (-)	Cc (-)
2.22	9.52	27.60	12.42	1.48

**Table 3-2** Fiber Properties.

Properties List (unit)	Value
Specific Gravity (-)	0.91
Length(mm)	23
Diameter ( $\mu\text{m}$ )	54
Electrical and Thermal Conductivity	Low
Water Absorption (-)	Negligible
Acid and Alkali Resistance	Excelent

### 3.2 Mix recipe and specimen preparation

Specimens used in this study were individually batched in volumes consistent with ASTM standard C39 plastic cylinder moulds, dimensions 10cm in diameter by 20cm in height. As indicated by the field studies referenced in section 1.2, large volumes of CPB have been found to contain different volumes of cement when sampled in the field. In order to maintain consistency between the specimens used in testing, it was decided that each mix should be individually batched. As summarized in Table 3-3, the mix recipe followed in the batching of specimens contained a cement content of 4.5% and a water-to-cement ratio of 7.6. The FR-CPB samples contained an additional 0.5% fiber reinforcement content. A combined method of manual and mechanical mixing was adopted throughout this study. The mechanical mixing of samples was completed using a Kitchen Aid D100 mixer set to the second lowest rotational setting (Figure 3-2).

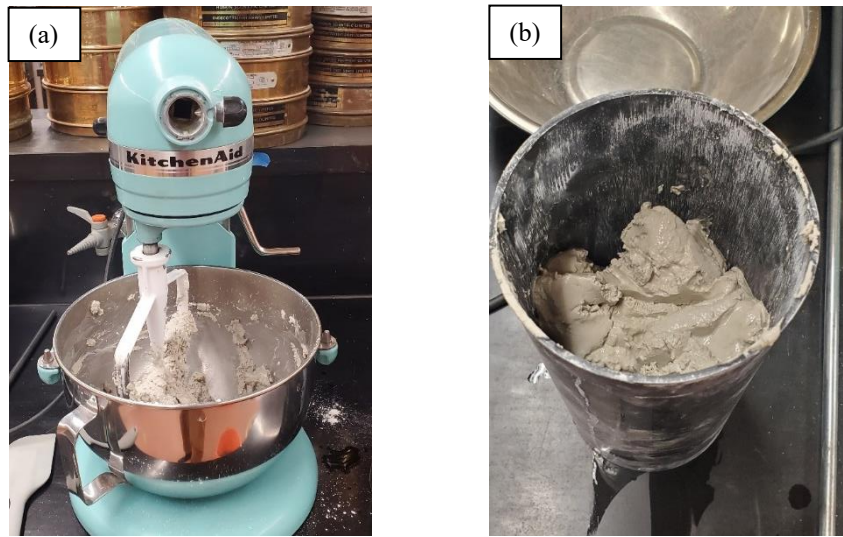


**Figure 3-2** (a) Kitchen Aid Mixer (b) CPB in cylinder mold.

**Table 3-3** Mix Design.

<b>Group</b>	<b>Curing Pressure</b>	<b>Mix Recipe</b>	<b>Curing Times (Days)</b>	<b>Tests per Age</b>	<b>Fracture Modes</b>	<b>Total Tests</b>
1A	0 kPa	W/C = 7.6 C <sub>m</sub> = 4.5% F <sub>c</sub> = 0.5%	3, 7, 28, 56	6 x SCB 3 x ENDB	I / II / III	36
1B	0 kPa	W/C = 7.6 C <sub>m</sub> = 4.5%	3, 7, 28, 56	6 x SCB 3 x ENDB	I / II / III	36
2A	100 kPa	W/C = 7.6 C <sub>m</sub> = 4.5% F <sub>c</sub> = 0.5%	3, 7, 28, 56	6 x SCB 3 x ENDB	I / II / III	36
2B	100 kPa	W/C = 7.6 C <sub>m</sub> = 4.5%	3, 7, 28, 56	6 x SCB 3 x ENDB	I / II / III	36
3A	200 kPa	W/C = 7.6 C <sub>m</sub> = 4.5% F <sub>c</sub> = 0.5%	3, 7, 28, 56	6 x SCB 3 x ENDB	I / II / III	36
3B	200 kPa	W/C = 7.6 C <sub>m</sub> = 4.5%	3, 7, 28, 56	6 x SCB 3 x ENDB	I / II / III	36

Note: water to cement ratio (W/C), cement content (C<sub>m</sub>), fiber content (F<sub>c</sub>), semicircular bend test (SCB), end notch bend test (ENDB).

Dry materials were first added to the bowl and mixed by hand for a period of 1.5 minutes to ensure the even distribution of the binder within the mix. For the FR-CPB mixtures, fibers were also added at this preliminary stage. It should be noted that the fibers were manually separated prior to their addition to allow for even distribution and reduce the potential for fiber clumping within the mix. Figure 3-3 highlights the difference between fibers before and after separation. After mixing the dry materials, water was added to the mixture, and the contents were manually mixed for an additional 1.5 minutes. By manually mixing the contents of the CPB/FR-CPB, the potential for freestanding water to splash out of the bowl during mechanical mixing became negligible. Mechanical mixing was conducted for a period of 7 minutes, pausing the procedure periodically to remove the build-up of material from the sides of the bowl. The freshly mixed material appeared, as can be seen in Figure 3-2b.

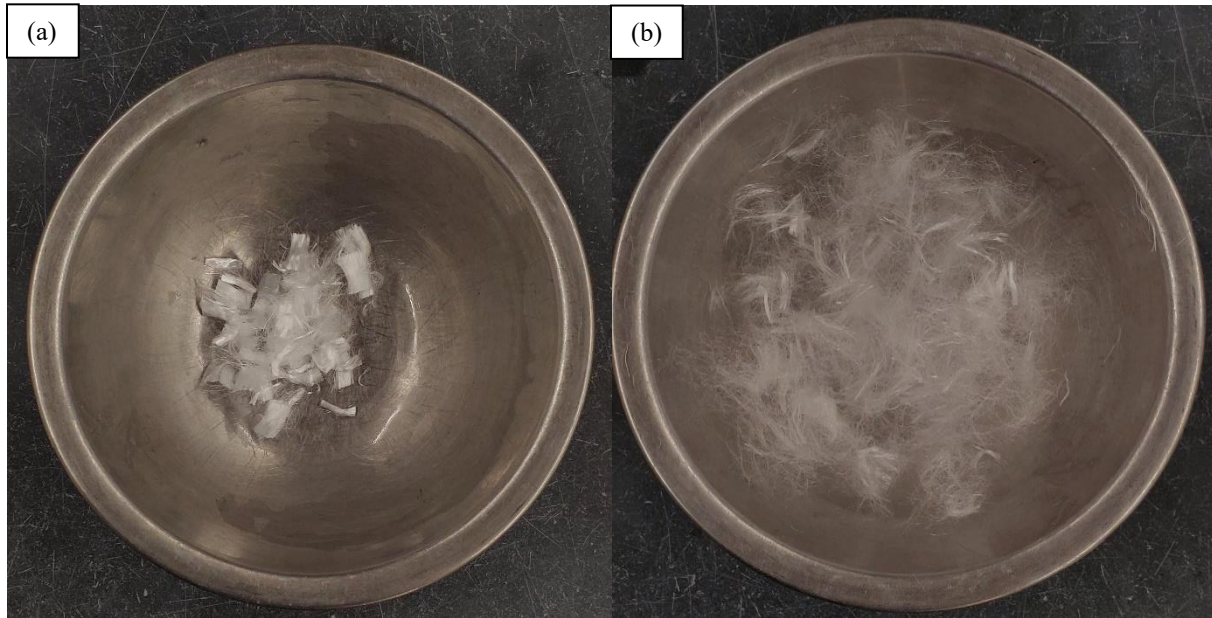


**Figure 3-3** Polypropylene Fibers (a) before and (b) after separation.

The placement of mixed contents followed a modified version of ASTM C31 for concrete cylinder testing. The use of rodding between each lift of material placed into the mold was neglected as it was found in the initial pre-trial design to result in additional voids within the cured samples. The mixed material was instead placed into the mold in three equal parts, with a rubber mallet being used to consolidate the material between lifts. After adding the total volume of material to the mold, plastic wrap was used to cover the exposed surface and secured with electrical tape. The plastic wrap was sealed tight against the sides of the mold to prevent loss of moisture during the curing process; however, the wrap itself was loose to allow for deformation of the sample as a result of the induced curing pressure. Specimens were cured for 3, 7, 28, and 56 days at pressures of 0, 100 and 200 kPa. A cylinder mold contained enough cured material to create either three circular specimens or six semi-circular specimens (dimensions and procedures for the creation of these are described in section 3.4). The testing program focused equal components on that of CPB and FR-CPB, the denotation of fiber inclusive samples having the letter A affixed to their group number and B for that of the fibreless samples. Each test conducted during this study was completed three times. In total, 48 cylinders were cast, allowing for a total of 216 semicircular bend (SCB) or end notch disc bend (ENDB) tests to be performed.

### 3.3 A new curing pressure apparatus

Extensive research was conducted into prior designs of pressure curing systems. The systems created and used in studies of Belem et al. [209], Yilmaz et al. [31], and Ghirian and Fall [33] each performed exceptionally well in capturing the in-situ characteristics of CPB. The caveat within this study was the desire to create a cost-efficient system capable of curing multiple cylinders at once. With the number of specimens required to complete the testing program of this study, a system capable of meeting the demand was necessary. As such, a new pressure curing system was created and adopted for use in this study. The curing tank system consisted of four modified levlor spray paint pressure pots, two tanks with a capacity to cure four cylinders, and an additional two tanks each with the capacity to cure two cylinders allowing for a total of 12 cylinders to be cured at any given time (Figure 3-4).



Figure 3-4 Pressure tanks.

In order to utilize the tanks as a pressure curing system, the following modifications were required. Two internal shafts, one for the paint mixer and the other for the distribution outlet, had to be removed from the system (Figure 3-5a). The internal component of the paint mixer was cut from the system, and the distribution shaft was unscrewed and sealed to prevent pressure fluctuations.

A dial gauge capable of reading pressure in kilopascals with an accuracy of 5 kPa was fixed to the top of each tank (Figure 3-5b). And finally, a quick connect inlet line was placed on top of pressure regular to allow access to the laboratory distribution network (Figure 3-5c and d). The distribution network allowed for a maximum pressure supply of 350 kPa, the pressure capacity of the tanks was approximately 400 kPa, and the maximum curing pressure utilized during testing was 200 kPa.



**Figure 3-5** Modifications to the Levlor Sprayer Tanks (a) internal rods (b) pressure gauge (c) quick connect coupler and regulator (d) laboratory supply outlets.

### **3.4 Mechanical testing program**

The mechanical testing program utilized the semicircular and end notch bend tests in order to determine mode-I, mode-II, and mode-III fracture properties. The method of cutting the samples as well as loading frame test setup is presented in sections 3.4.1 and 3.4.2. The testing procedure, including the setup and use of data acquisition software, is detailed in section 3.4.3.

#### **3.4.1 End Notch Disc Bend (ENDB) Test**

End Notch Disc Bend (ENDB) tests were used in the determination of mode-III fracture properties. Figure 3-6(a and b) provides a detailed diagram of the sample dimensions and notch sizes alongside examples of the actual specimens. All cuts of samples to the required dimension, including that of the notch, were conducted with a Bosch miter saw with a masonry blade. Using a cured cylindrical specimen with a height of 200 mm and a radius of 100mm), three circular specimens were cut to heights of 50 mm. To ensure a flat surface for the first specimen, the top 150mm of the cylindrical specimen was first cut and discarded. Using the cutting jig presented in Figure 3-7(a and b) a 20mm deep notch was cut along the base through the center of each of the ENDB test specimens. The same cutting jig was used throughout the duration of testing to ensure uniformity between trials. Prior to testing, a line was drawn across the top of the specimen corresponding to the positioning of the notch below. A secondary line was drawn at an angle of 60 degrees of the center of the notch position to indicate the desired position of the loading bar and allow for the sample to be rotated into position within the loading frame. Figure 3-6(c and d) details the positioning of the test specimen with reference to the loading frame. The bottom loading bars were spaced 900 mm apart, and the specimen rotated so that the notch ran 60 degrees off the center of the top loading bar. In total, 72 ENDB tests were performed, allowing each respective curing pressure, age, and fiber content to be trialed three times.

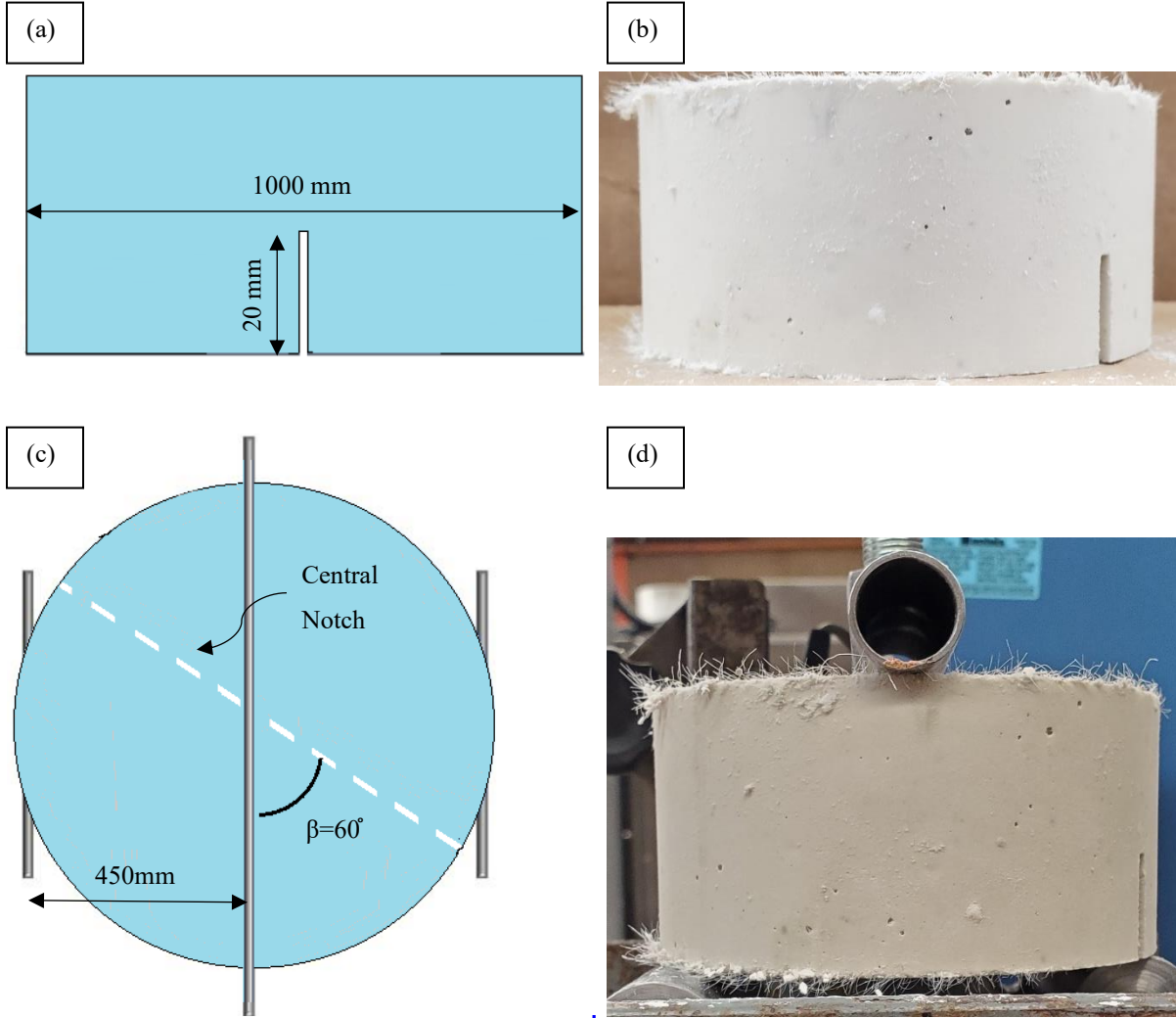


**Figure 3-6.** FR-CPB samples for ENDB tests (a) side view ENDB schematic (b) side view ENDB FR-CPB sample (c) loading bar ENDB schematic (d) loading bar ENDB FR-CPB sample.

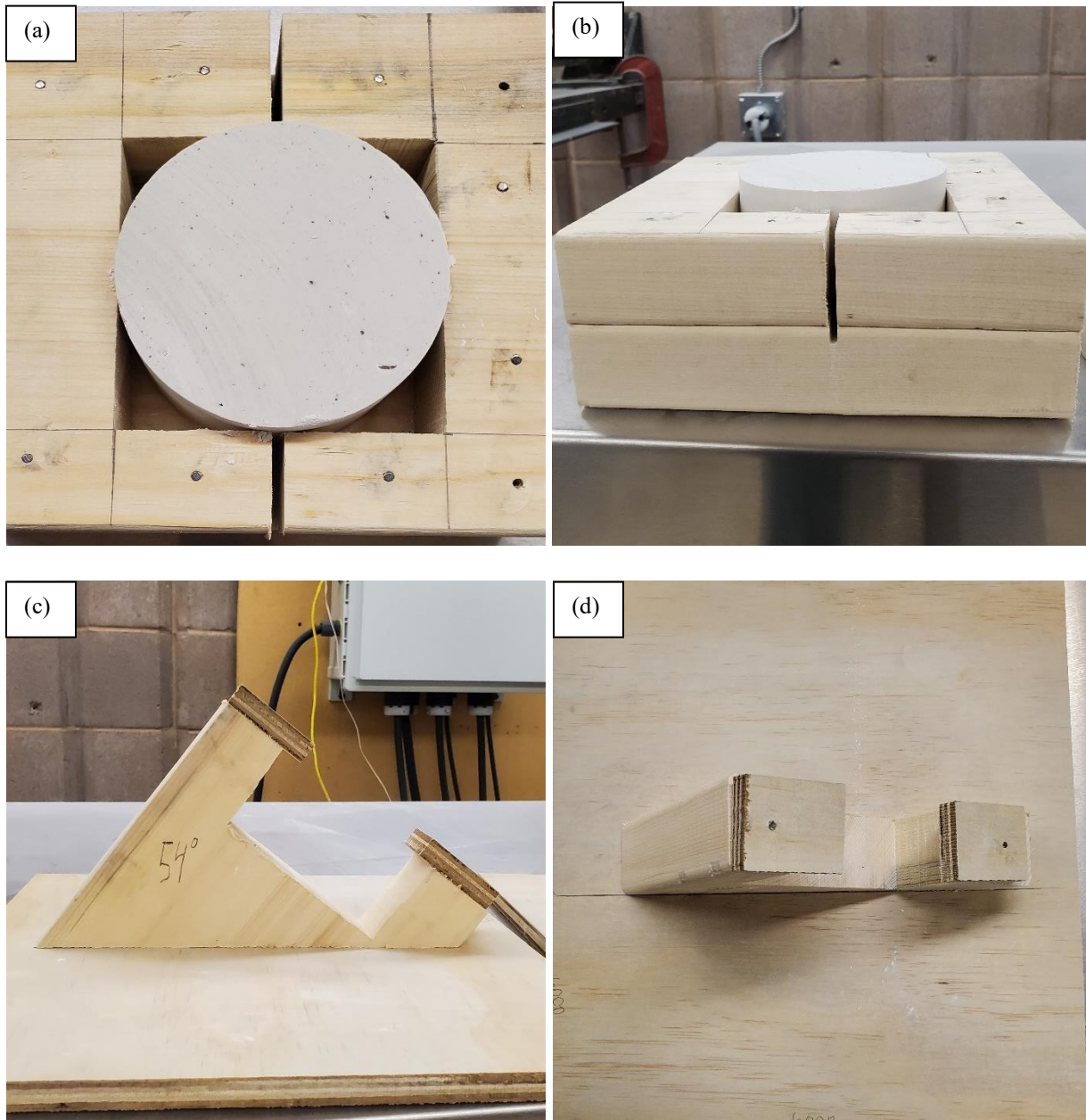


**Figure 3-7** Self-designed cutting Jigs for fabrication of SCB and END samples (a) mode-III, mode-I, and semi-circular cut Jig top view (b) mode-III, mode-I, and semi-circular cut Jig side view (c) mode-II Jig side view (d) mode-II Jig top view.

### 3.4.2 Semicircular Bend (SCB) Test

Semicircular Bend (SCB) tests were used in the determination of mode-I and mode-II fracture properties. Figure 3-8 provides a detailed diagram of the sample dimensions and notch sizes alongside examples of the actual specimens. All cuts of samples to the required dimensions, including that of the notch, were conducted with a Bosch miter saw with a masonry blade.

Following the same procedure outlined in section 3.4.1, the specimens were first cut into discs of height of 500 mm, the samples were then cut in half using the jig presented in Figure 3-7(a and b) to create semicircular specimens of the height of 250 mm with a radius of 500 mm. For mode-I loading conditions, a 250 mm deep notch was cut through the base of the semi-circular specimen parallel to the plane of loading. For mode-II loading conditions, a 250 mm deep notch was cut through the center of the base of the specimen at an angle of 54 degrees off the plane of loading. The same cutting jig used in ENDB sample preparations was used for mode-I notching, and the cutting jig used in the cutting of mode-II samples is displayed in Figure 3-7 (c and d).

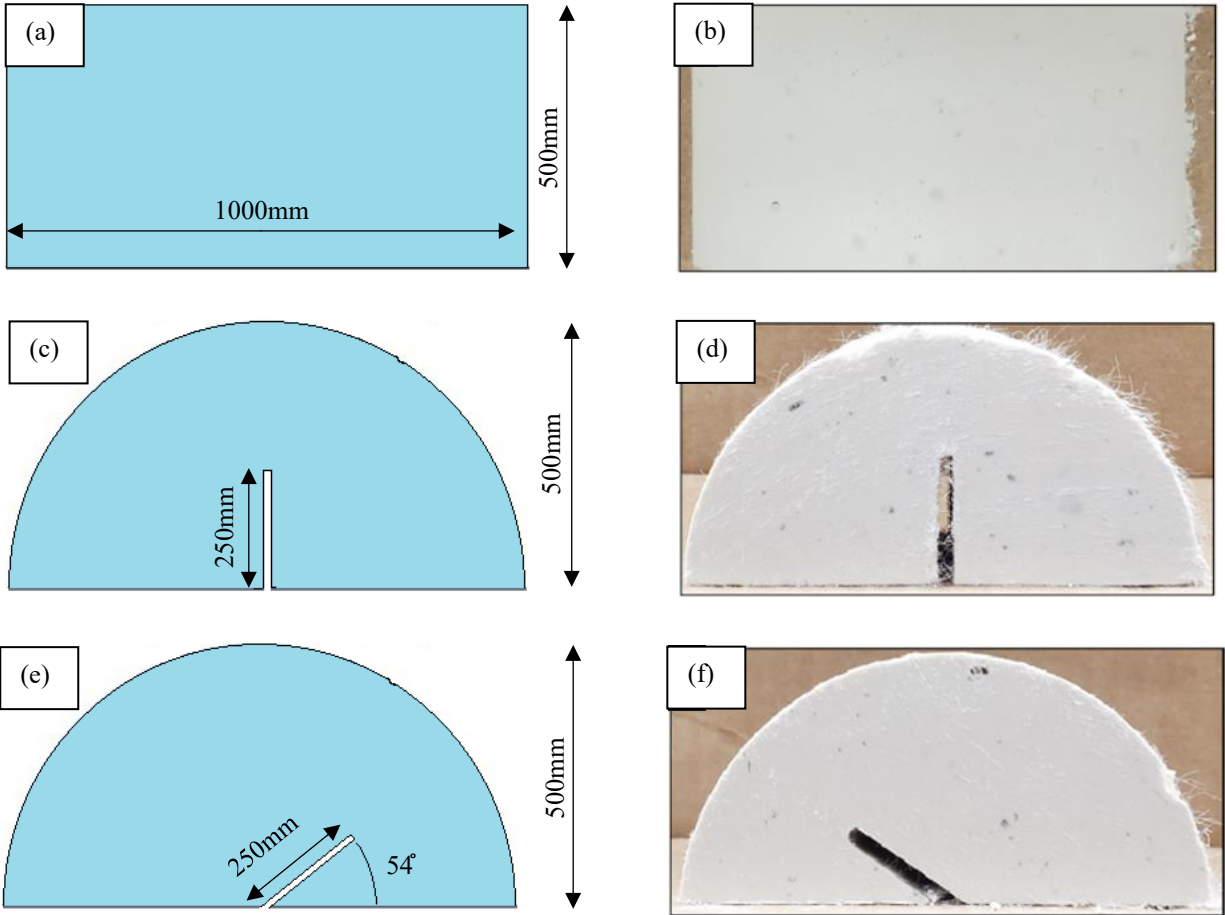


**Figure 3-8.** CPB samples for mode-I and mode-II SCB tests. (a) top view schematic (b) top view sample (c) side view mode-I SCB dimensions (d) side view mode-I specimen (e) side view mode-II SCB dimensions (f) side view mode-II specimen.

The test setup used for mode-I and mode-II loading utilized the same loading bars. The bottom bars were spaced at 800mm and were free to rotate so as to allow deformation of the sample with the application of loading. The top loading bar was fixed and placed directly over the center of the

semicircular specimens. A schematic showing the bar spacing as well as an image of a mode-I sample on the loading frame is provided in Figure 3-9. The failure pattern was documented throughout the testing program as a tool to explain any deviations in test results. In total, 144 SCB tests were performed, allowing each respective curing pressure, age, and fiber content to be trialed three times.

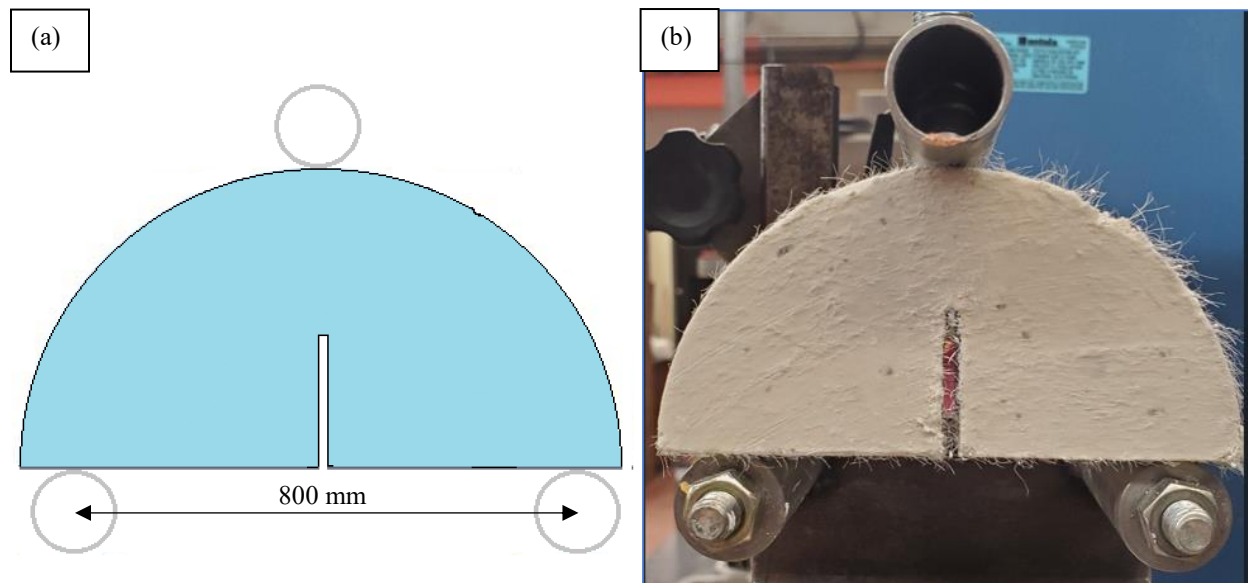


**Figure 3-9** Bar Spacing of SCB Loading Frame (a) loading bar schematic (b) FR-CPB sample in load frame.

### 3.4.3 Testing procedure

Load displacement testing was performed for each failure mode using an ELE Digital Tritest 50 Load frame in conjunction with Strain Smart 5000 data acquisition software. A loading rate of 1mm per minute was set with a sampling rate of 10 readings per second. Force and displacement were measured using an S-type load cell from ARTECH Industries Inc. with a capacity of 1000 pounds, and a linear variable differential transformer (LVDT) displacement sensor from A-Tech Instruments Ltd. Sensors were calibrated prior to each test performed. The data acquisition software allowed for the load-displacement data to be monitored through the testing process and provided an excel spreadsheet of raw data at the conclusion of each test. The loading frame set up along with the monitoring system can be seen in Figure 3-10.

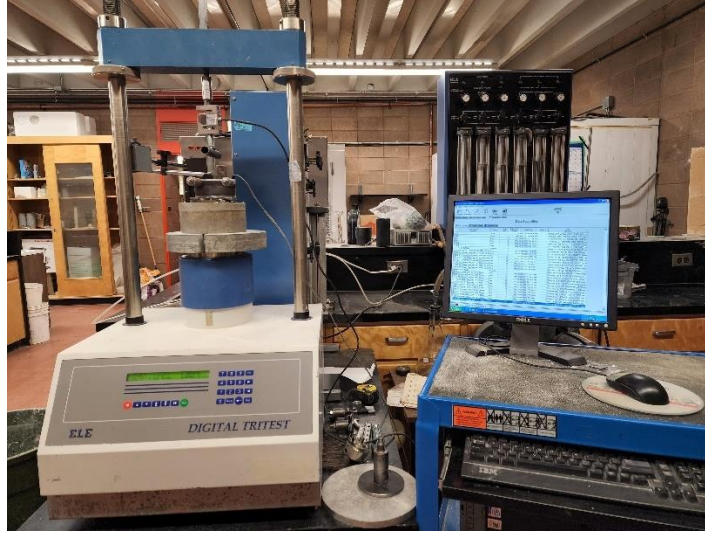


Figure 3-10 ELE load frame and computer set up.

### 3.5 Scanning Electron Microscope (SEM) Analysis

Scanning Electron Microscope (SEM) imagery was taken to explore the microstructural evolution of CPB with curing pressure, time, and the addition of fiber reinforcement. After the completion of each of the primary experimental analyses, a portion of the specimen was labeled and placed into an oven at 70 degrees Celsius in order to arrest the progression of hydration. The samples were removed after 24 hours, placed into a Ziploc bag, and then stored until the date of imaging. Sample preparation included reducing the sample size to a 5mm square with a thickness of 1mm, affixing the sample to an observation pedestal, then coating the sample with a conductive gold spray so as to allow the image formation. A Hitachi SU-70 microscope with the capability of capturing images up to a magnification of 80000x (1  $\mu\text{m}$  scale). Images were taken at 5,10,20,50, and 100  $\mu\text{m}$  so as to be able to observe the micro and mesoscale changes in the specimen. The equipment used and a set of 12 coated samples is displayed in Figure 3-11.

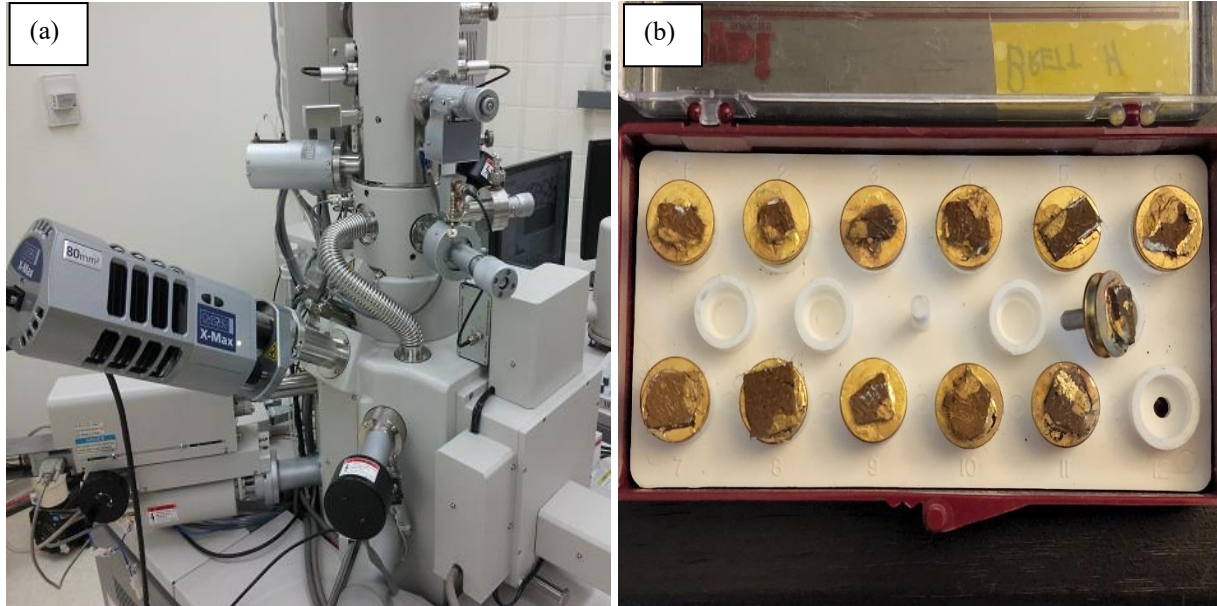


Figure 3-11 a) Hitachi Su-70 microscope b) gold coated FR-CPB samples.

### 3.6 Determination methods of fracture properties

The load-displacement graphs acquired through testing of the respective SCB and ENDB specimens allowed for the calculation of three fracture properties, material stiffness, fracture toughness, and energy of fracture. The calculation of each fracture toughness is described in sections 3.6.1 to 3.6.3. While the addition of binders such as cement to composites generally results in a brittle material, the low volumes used in that of CPB, along with the fine gradation of tailings material, lends itself to a more dynamic evolution of material properties with both curing pressure and time. As such, the determination of multiple fracture properties was conducted in order to capture the best representation of the material behavior.

#### 3.6.1 Material Stiffness

Material stiffness is a measure of a composite's ability to resist permanent deformation under the application of force. A value of high stiffness thus represents a composite with the ability to undergo little deformation at high levels of stress. As CPB may be used as a working surface, the need to prevent deformation under dynamic application of loading is essential. Material stiffness is represented by the slope of the load-displacement curve prior to failure. In order to capture the most consistent slope of the graph values of 40% and 60% peak load were chosen for calculations in this study. Equation 3-4 shows the method of calculation for material stiffness with Figure 3-

13 showing the process for how the load and displacement values used in the calculation were gained.

$$S = \left( \frac{0.6P - 0.4P}{\delta_{60} - \delta_{40}} \right) \quad 3-4$$

Where,

P: peak load (N)

$\delta_{60}$ : displacement corresponding to 60% peak load

$\delta_{40}$ : displacement corresponding to 40% peak load

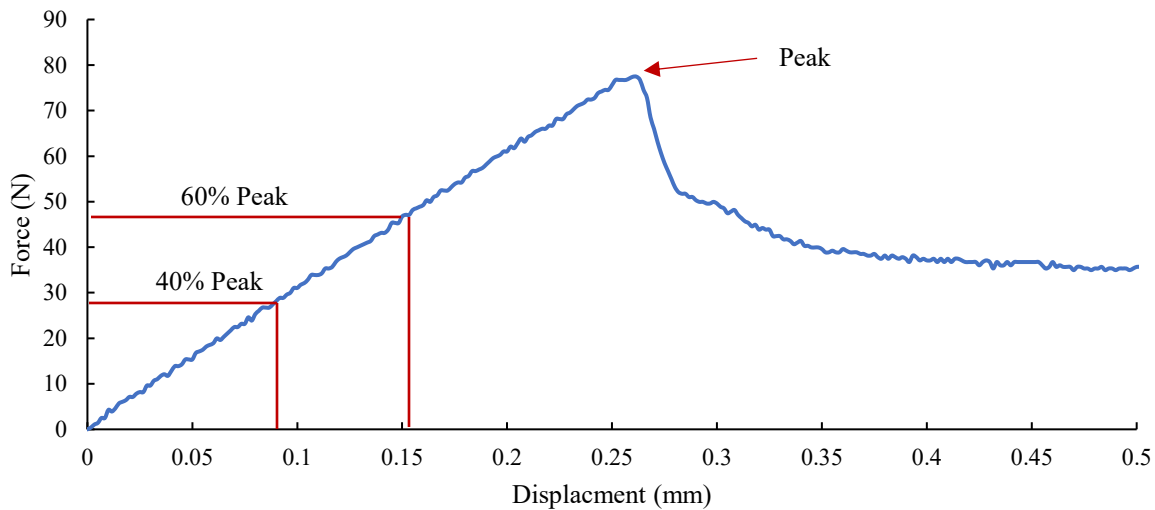


**Figure 3-12** Calculation of stiffness from load-displacement graph.

### 3.6.2 Fracture Toughness

Fracture toughness represents the ability of an imperfect (flawed or cracked) material to resist the propagation of further cracking. The notches placed in the SCB and ENDB specimens correspond to the imperfections within the material. Mode-I fracture toughness represents the ability of the material to resist crack propagation under pure tensile forces acting normal to the plane of the crack. Mode-I loading conditions were simulated using the SCB specimen with a 25mm deep notch cut parallel to the plane of loading. Mode-II fracture toughness represents the ability of the material to resist crack propagation under in-plane shear stress acting parallel to the plane of the crack. Mode-II Loading conditions were simulated using the SCB specimen with a 25mm deep

notch cut to an angle of 54 degrees through the base of the specimen at the position directly under the point of loading. Mode-III fracture toughness represents the ability of the material to resist crack propagation under out-of-plane shear stress acting parallel to the plane of the crack. Mode-III loading conditions were simulated using the ENDB test with a 20mm deep notch cut through the base of the specimen at an angle of 60 degrees off the center point of the top loading bar. Each loading condition was representative of a different form of failure method present in a CPB structure. The progression of mining below a structure results in tensile forces developing in the artificial CPB rough and thus the potential for mode-I loading conditions. The removal of an adjacent rock wall results in an imbalance of confining pressure within the structure and along its exposed face. The unequal principal stresses resulting from changes in confinement can yield to the formation of mode-II and mode-III loading conditions and the subsequent propagation of shear cracking. As such, each mode of fracture was investigated within this study. The calculation of modes-I, -II, and -III fracture toughness were completed using equations 3-5, 3-6, and 3-7, respectively.

$$K_I = \frac{P}{DT} \sqrt{\pi a} Y_I \quad (3-5)$$

$$K_{II} = \frac{P}{DT} \sqrt{\pi a} Y_{II} \quad (3-6)$$

$$K_{III} = \frac{6PS}{RB^2} \sqrt{\pi a} Y_{III} \quad (3-7)$$

Where,

$K_I, K_{II}, K_{III}$ : fracture toughness for modes -I, -II, -III, respectively ( $\text{Pa} \cdot \sqrt{\text{m}}$ )

P: maximum force (N)

D: diameter of the specimen (mm)

T: thickness of specimen (mm)

a: depth of notch (mm)

S: distance between central and edge bar of loading frame (mm)

R: radius of the specimen (mm)

$Y_I$ : normalized stress intensity factor for mode-I (6.52)

$Y_{II}$ : normalized stress intensity factor for mode-II (1.072)

$Y_{III}$ : normalized stress intensity factor for mode-III (0.0713)

### 3.6.3 Energy of Fracture

The energy of fracture referred to in this study is representative of the work of fracture for the specimens used. The property being extensive in nature, the values calculated in this study are applicable for comparison with respect to curing pressure and age of curing for the designated specimen size; however, they are not representative of an intensive material strength for the mix design. The energy of fracture takes into account both force and displacement in its calculation, making it an additional tool in the investigation of fracture properties for CPB and FR-CPB. Analysis of CPB samples included that of the energy of crack initiation, while that of FR-CPB samples also included the energy to reach fiber bridging. The energy of crack initiation is representative of the work needed to initiate the propagation of cracking within the sample and was calculated as the area under the load-displacement graph from initial loading to peak (Figure 3-14a). The energy to fiber bridging is representative of the additional energy dissipated post cracking to reach fiber bridging and was calculated as the area under the load-displacement curve from initial loading to the end of the initial linear post-peak branch (Figure 3-14b).

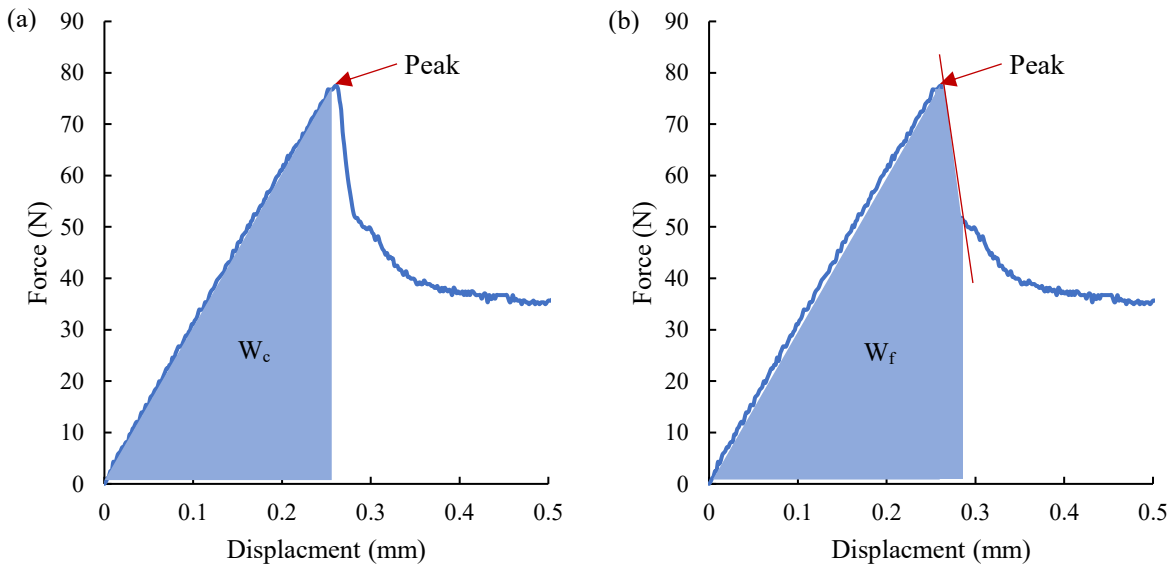
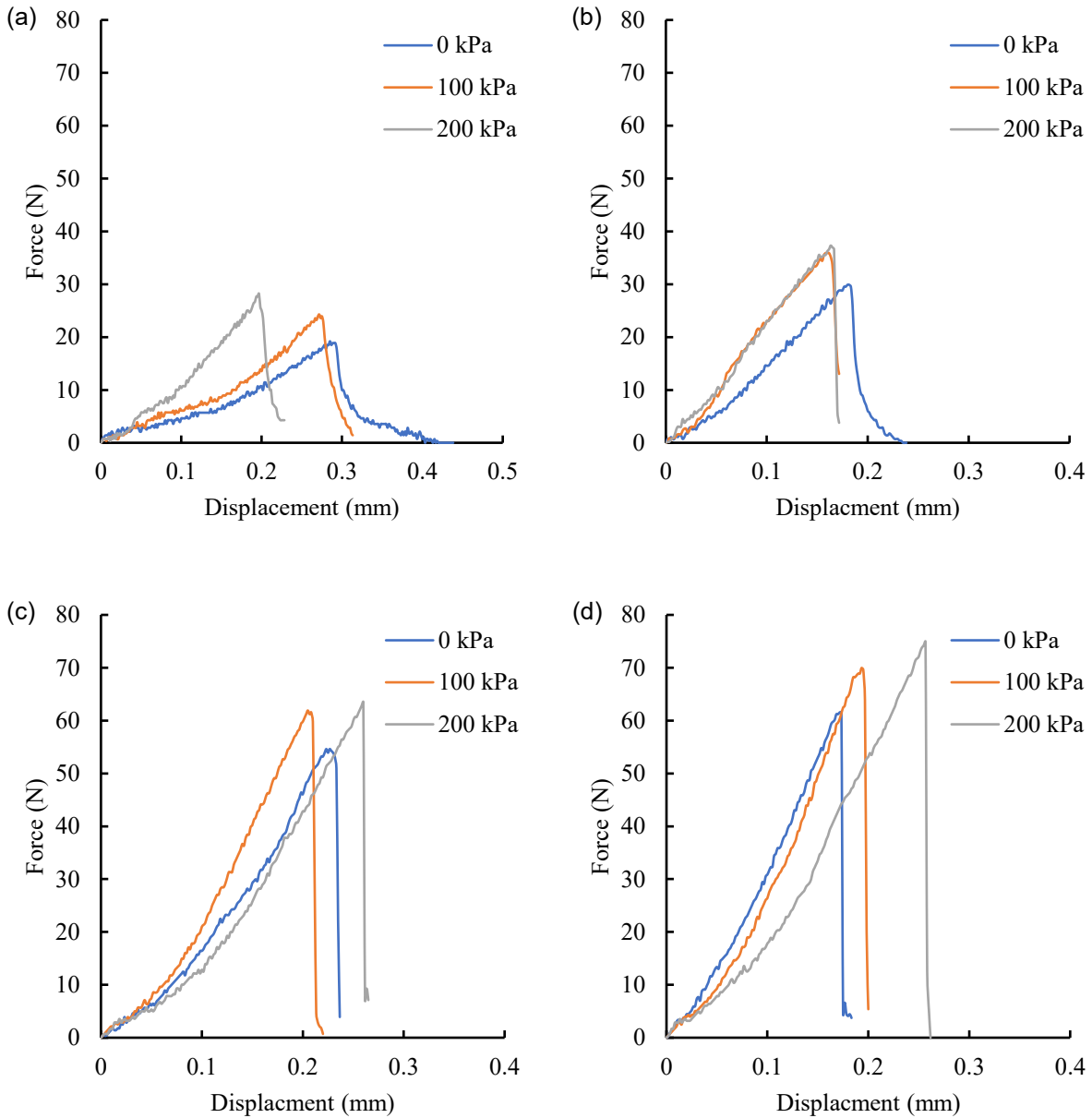


**Figure 3-13** Definition of fracture properties of FR-CPB:(a) energy of fracture initiation and (b) energy of fiber bridging.

## Chapter 4 Experimental results

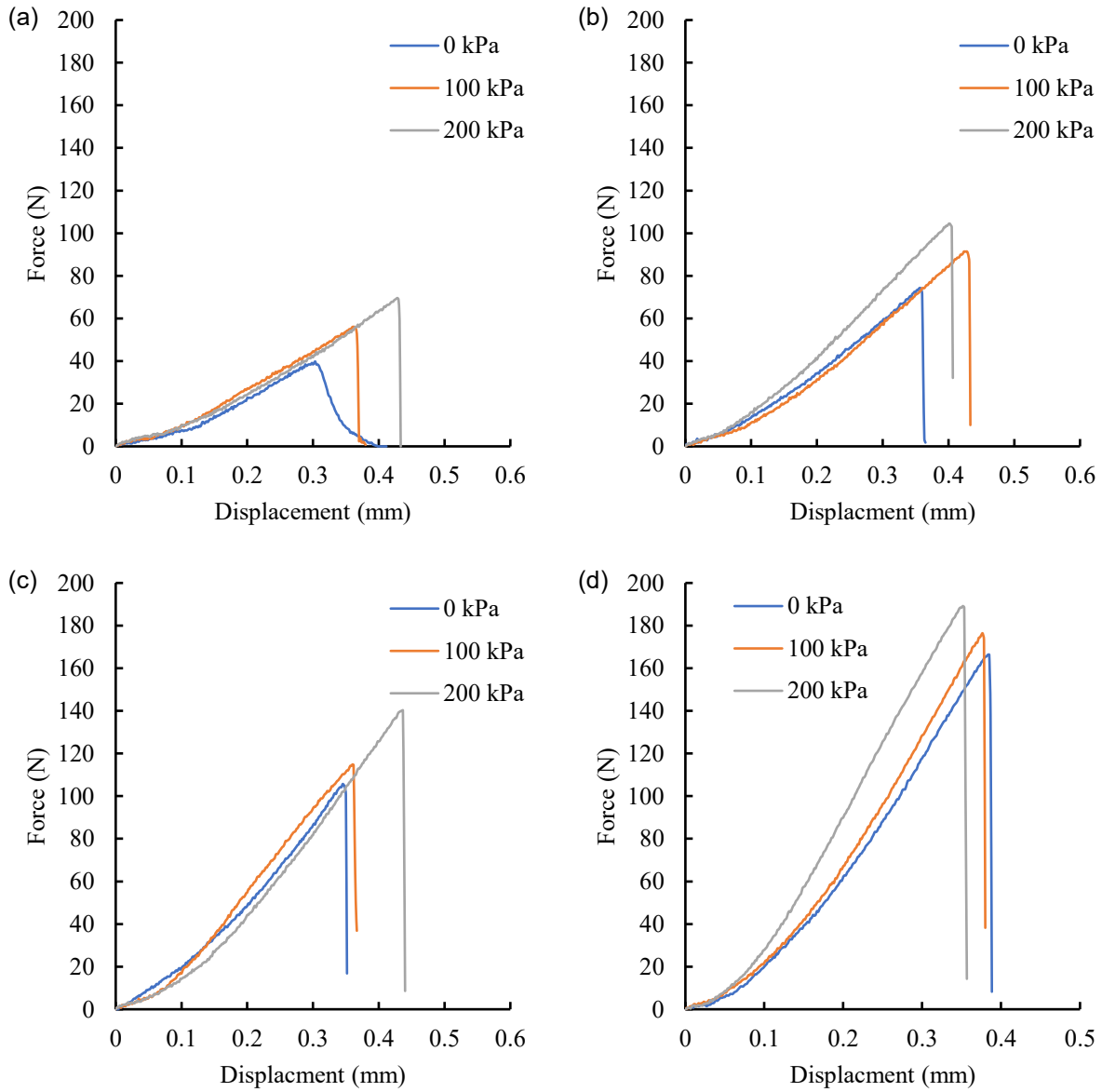
### 4.1 Evolutive fracture behavior and properties of CPB under curing pressure

#### 4.1.1 Effect of curing pressure on mode-I fracture behavior of CPB



**Figure 4-1.** Effect of curing pressure on the mode-I load-displacement curves at (a) 3 days, (b) 7 days, (c) 28 days, and (d) 56 days.

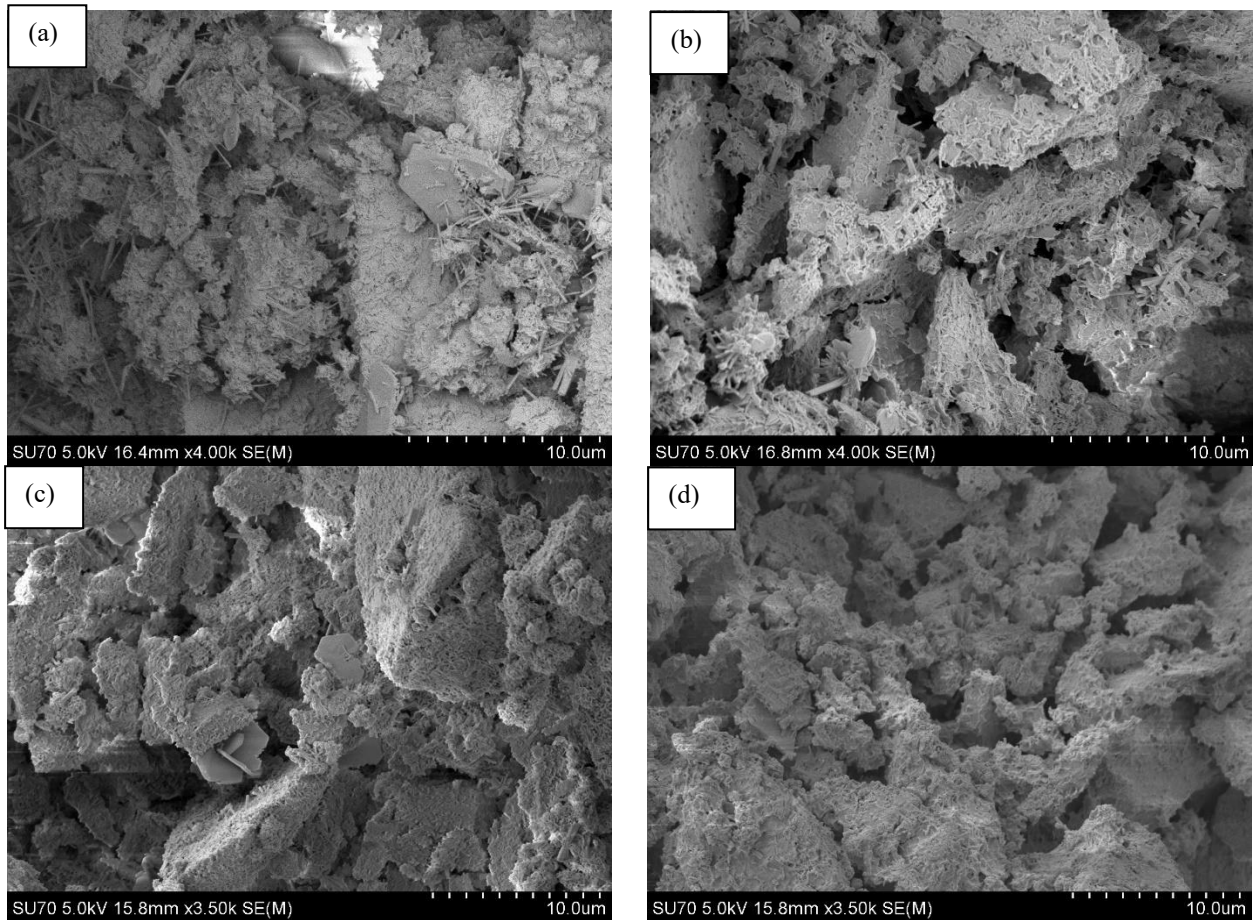
### 4.1.2 Effect of curing pressure on mode-II fracture behavior of CPB



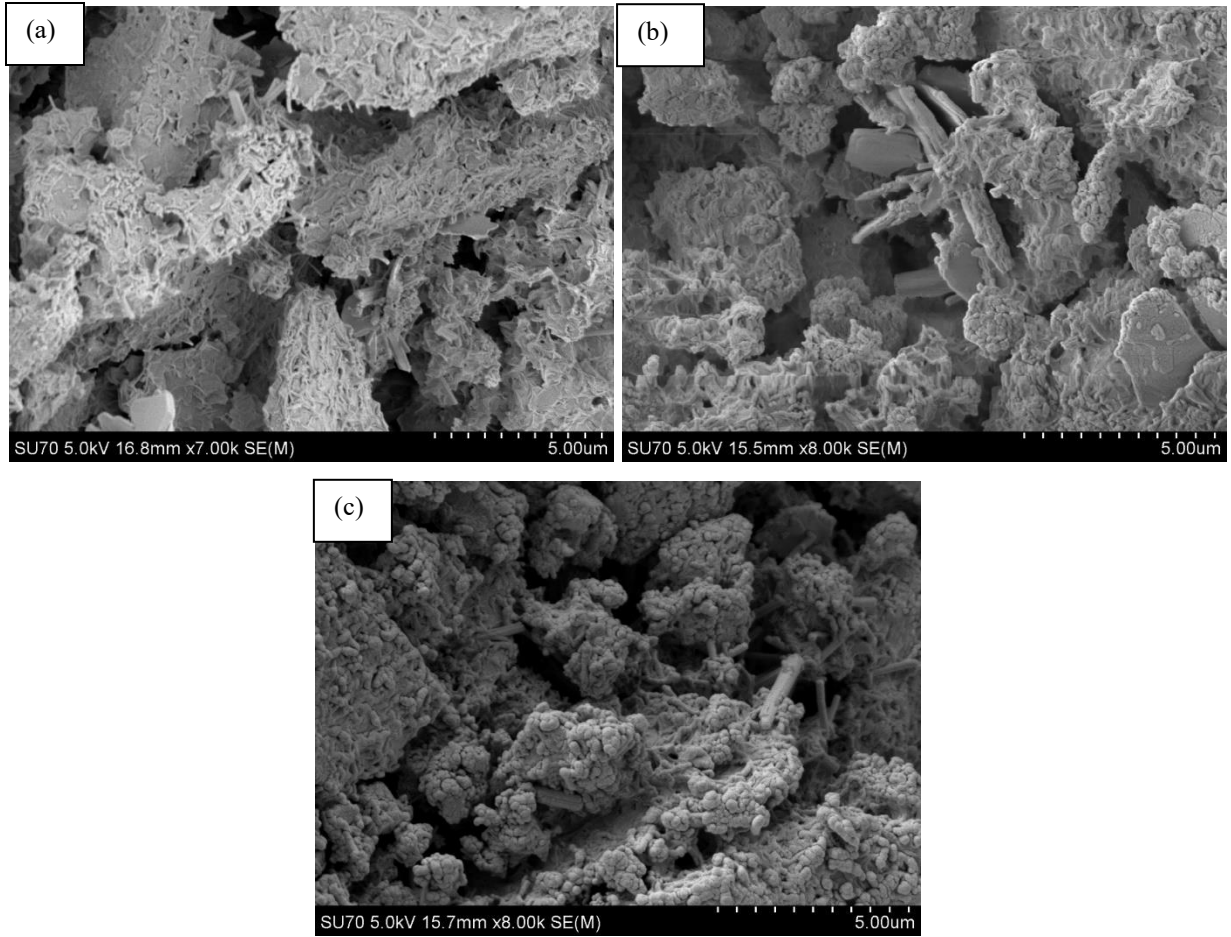
**Figure 4-2.** Effect of curing pressure on the mode-II load-displacement curves at (a) 3 days, (b) 7 days, (c) 28 days, and (d) 56 days.

The evolution of mode-II fracture behavior follows that discussed in Section 4.4.1. From early to advanced ages, it can be found that the CPB materials gain strength with increases in curing pressure and time (see Figure 4-2). The progression of cement hydration allows for greater interparticle bonding. This is visible in the progression of cement hydration exhibited in Figure 4-3 from early to advanced ages. Take note of the greater volumes of ettringite (crystal structure) forming because of the loose pore structure in early ages and the increase in CSH (globule-like

structure) surrounding the particulate matter in advanced ages. The failure method of mode-II loading is a result of pure in-plane shear stress. The increases in strength may be attributed to either cohesion or friction. While it may be assumed that densification of the particles would result in greater degrees of friction within the material, adding to the resistance of crack initiation, there is little evidence that pressure can affect friction angle. The work of Ghirian and Fall [22] found that cohesion is a driving factor in increasing the strength of CPB with curing stress. The increase in interparticle bond strength may be attributed to the greater degree of cement hydration for samples cured at higher pressures as well as the reduction in porosity, the hydration products filling in the smaller voids in the densified structure. This is evident in the comparison of hydration products at different curing pressures for samples at the same ages. Figure 4-4 shows the hydration products formed at different curing pressures for samples cured for 28 days. The reduction in CH and ettringite formation may be observed in the 200 kPa sample, which consists of a higher degree of CSH.

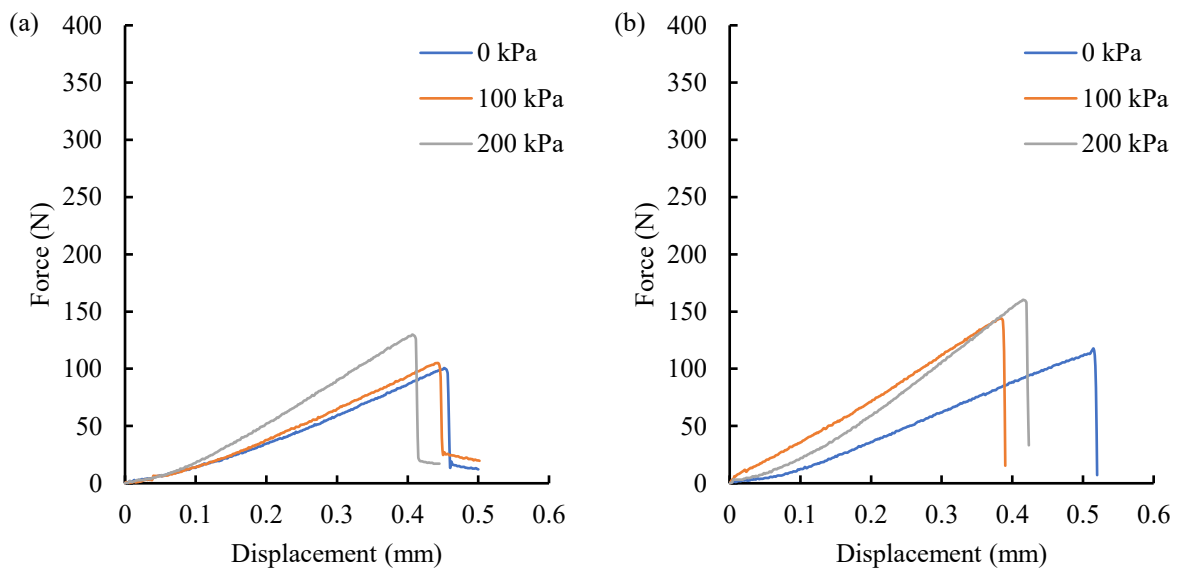


**Figure 4-3** SEM images of microstructure of control CPB matrix at (a) 3 days, (b) 7 days, (c) 28 days, and (d) 56 days.



**Figure 4-4** SEM images of microstructure of 28 day CPB matrix at (a) 0 kPa, (b) 100 kPa and (c) 200 kPa.

#### 4.1.3 Effect of curing pressure on mode-III fracture behavior of CPB



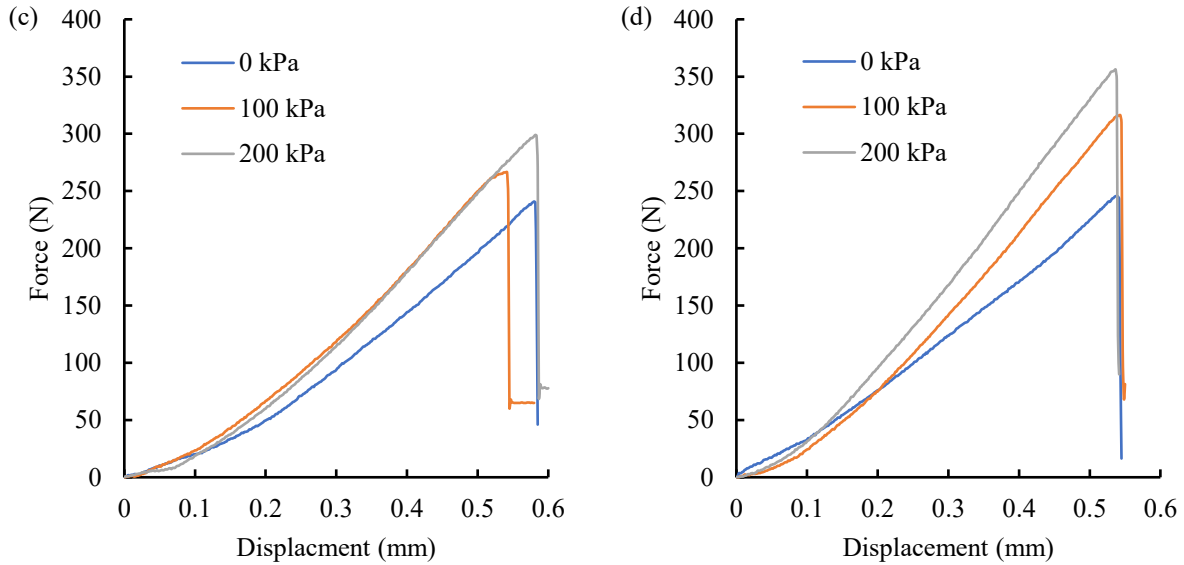


**Figure 4-5.** Effect of curing pressure on the mode-III load-displacement curves at (a) 3 days, (b) 7 days, (c) 28 days, and (d) 56 days.

For mode-II crack propagation, the unequal principal stresses commonly lead to the formation of shear stress which can result in the formation of in-plane shear. However, when the CPB surfaces are exposed after the secondary stopes are extracted, the resultant loss of confining pressure on the exposed surface will lead to the lateral deformation of CPB mass under the surrounding discharge pressure from rock mass. In the vicinity of rock walls, the crack propagation will be parallel to the vertical rock walls, which indicates the formation of torsional loads acting on CPB mass near the rock walls. As a result, the mode-III (out-of-plane shear) cracks can be formed. As such, it is of practical importance to investigate the fracture behavior of mode-III loading in conjunction with that of mode-II. Similar to the previous modes of failure, the evolution of mode-III fracture toughness is sensitive to curing pressure and time. The greatest improvements in fracture behavior of mode-III loading with respect to curing pressure are found in the advanced ages of curing. At this stage, the deformation at failure becomes consistent, the effects of curing pressure increasing the peak loading by 29% and 45% with respective increases in curing pressure of 100 kPa and 200 kPa. The densification of the matrix with respect to curing pressure allows for the formation of hydration products to progressively have a greater impact with respect to time, as discussed in section 4.1.2

## 4.1.4 Effect of curing pressure on fracture properties of CPB

### 4.1.4.1 Material Stiffness

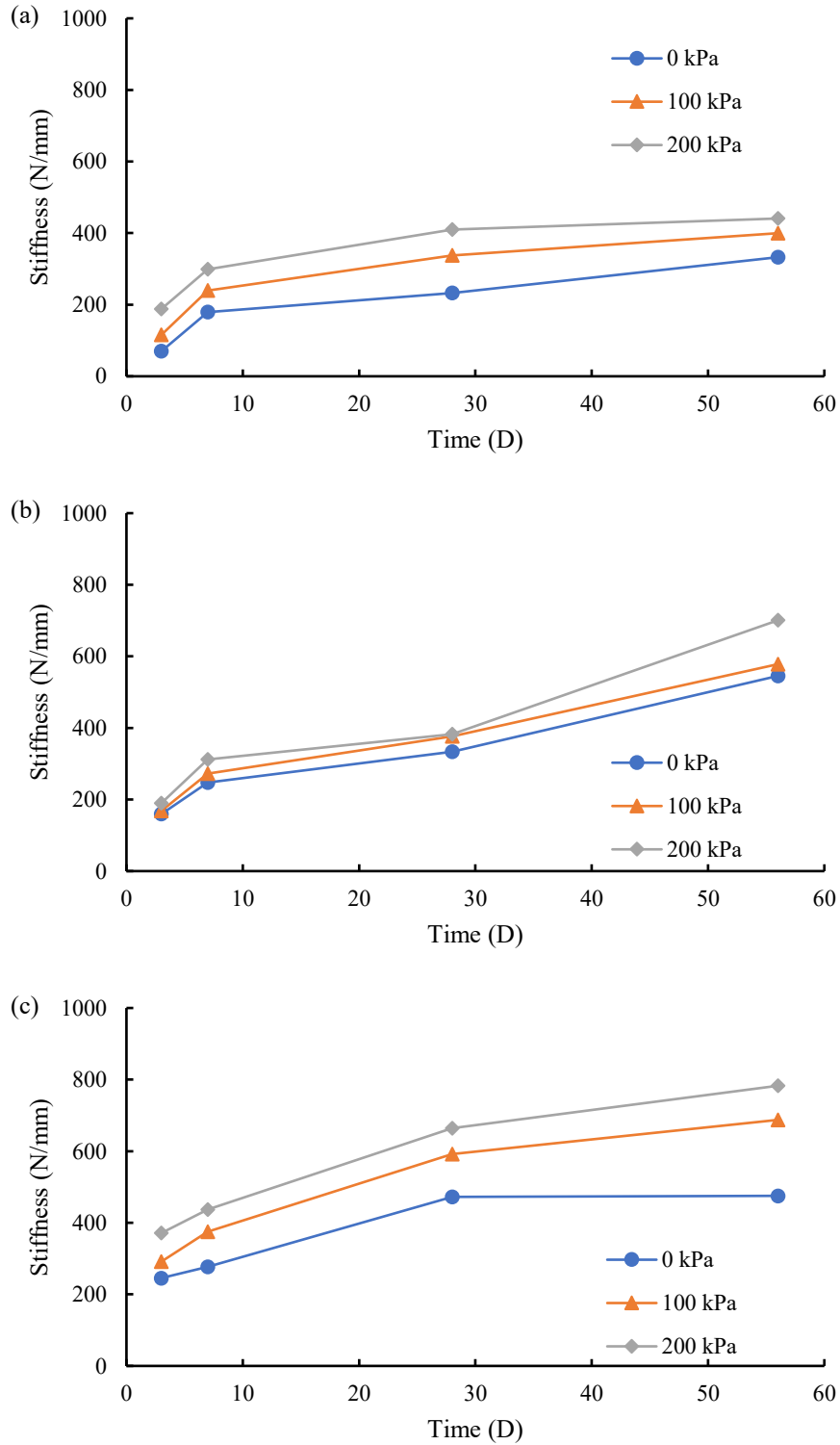
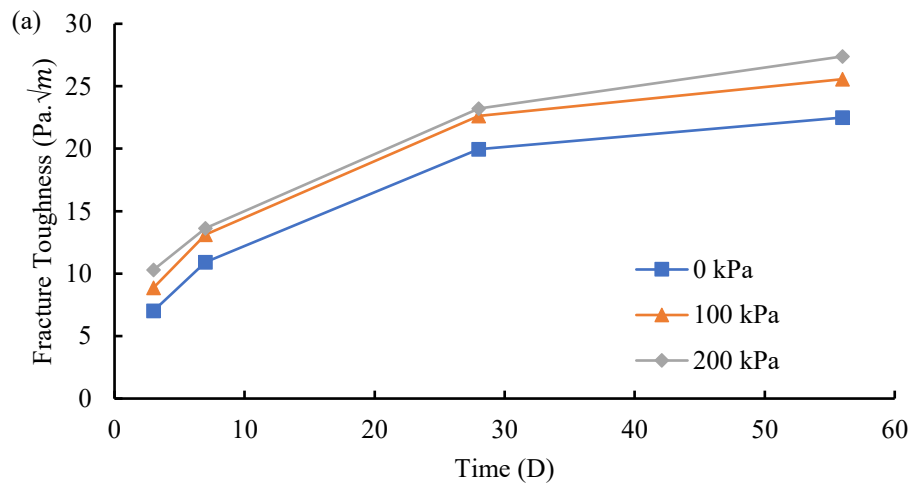
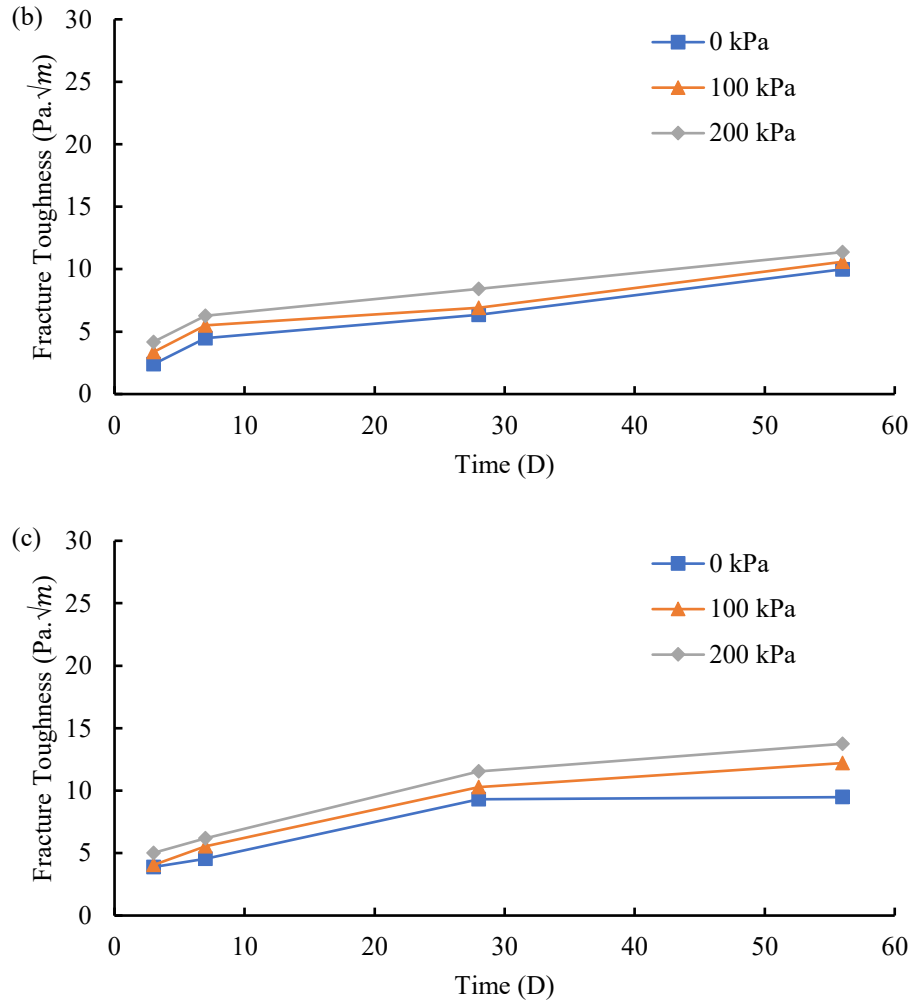


Figure 4-6. Effect of curing pressure on evolutive stiffness of CPB under (a) mode-I, (b) mode-II, and (c) mode-III loadings.

With regard to Figure 4-6, the material stiffness of CPB shows continuous improvement with both increased curing pressure and age. The evolution of material stiffness with age follows a typically logarithmic trend for both mode-I and mode-III loading. This trend represents the rate of reaction for hydration within the mixture, the pace quick at early ages and increasingly slowing down as less surface area of cement is available to hydrate. What is of interest is the stiffness for mode -II loading conditions between 28 and 56 days, where the rate increases further. This may highlight the effects of cement hydration on the interparticle forces at later ages. Studies on cemented soils undergoing curing under induced pressure conditions have found that the early age hardening of the composites structure resulted in significant increases in stiffness during shearing[210-211]. This is reflected in the results of modes-II and modes-III, which show greater progressions of material stiffness with curing pressure than that of mode-I samples. While an increase in all fracture properties was hypothesized with regard to the effects of induced curing pressure, the effects were thought to largely be a result of the increases in fiber matrix interfacial interaction, as can be seen in section 4.2.4.1. The results found with ordinary CPB thus highlight the contribution of the bulk matrix itself to the fracture properties of FR-CPB.

#### 4.1.4.2 Fracture Toughness



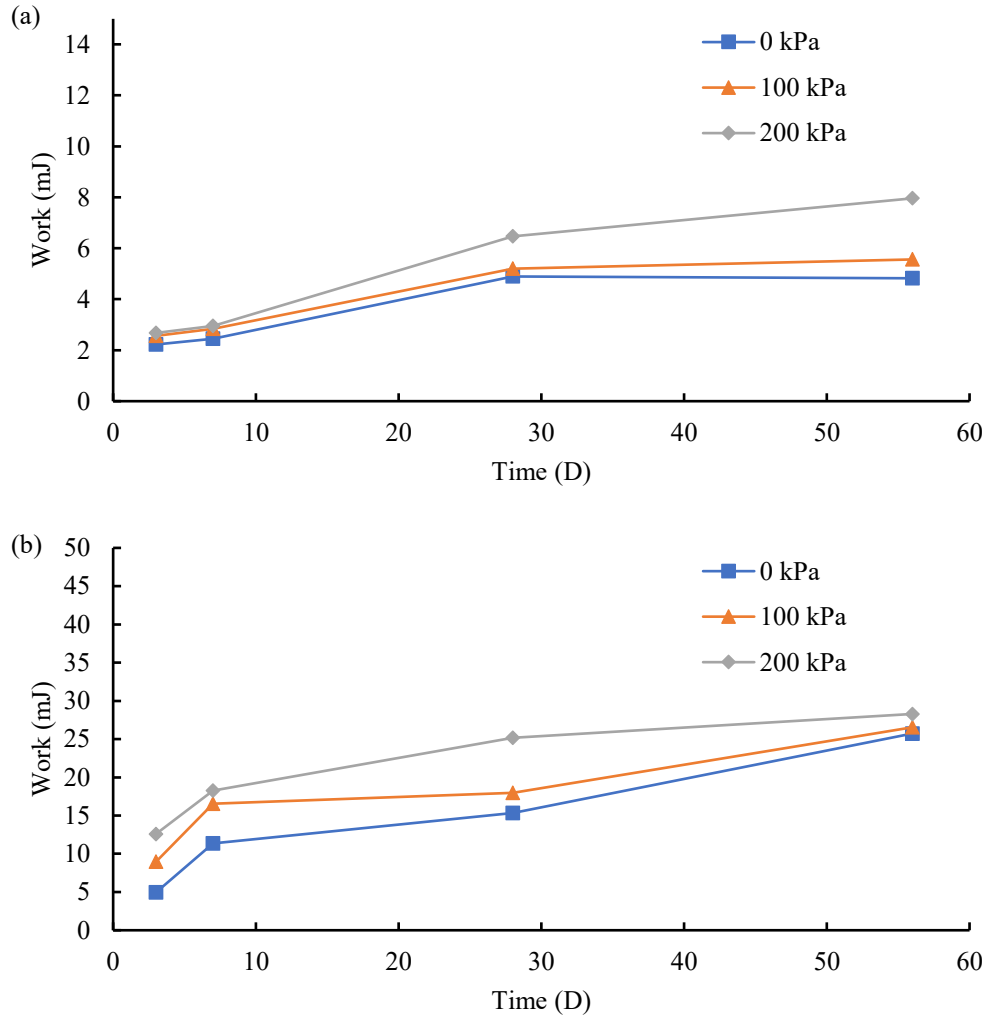


**Figure 4-7.** Effect of curing pressure on evolutive fracture toughness of CPB under (a) mode-I, (b) mode-II, and (c) mode-III loadings.

Fracture toughness for each mode of loading was found to increase with both time and increased levels of curing pressure. As stated in each of the prior sections, the continued formation of hydration products with time is responsible for respective gains in fracture toughness. The logarithmic improvement in fracture toughness of mode-I loading shows the dependency of tensile resistance on the hydration process, following the same trend as that of strength with cement hydration[212]. What is of significance to this study is the notably larger increase in fracture toughness with increasing curing pressure at advanced ages, specifically in that of mode-I and mode-III samples (Figure 4-7). This finding highlights the time-dependent nature of the effects of induced curing pressure. At early ages, the benefits of increased curing pressure are mirrored in the evolution of fracture toughness with time. The apparent increase in performance at advanced

ages may be explained through the formation of HD-CSH. This is supported by the correlation of increased production of HD CSH with curing pressure [194]. As shown in section 4.1.2, the effects of induced curing pressure allow for the formation of higher degrees of CSH within the bulk matrix, and the effect of curing time allows for greater penetration of water into the outer shell of CSH allowing for the stronger HD-CSH to form.

#### 4.1.4.3 Fracture Energy



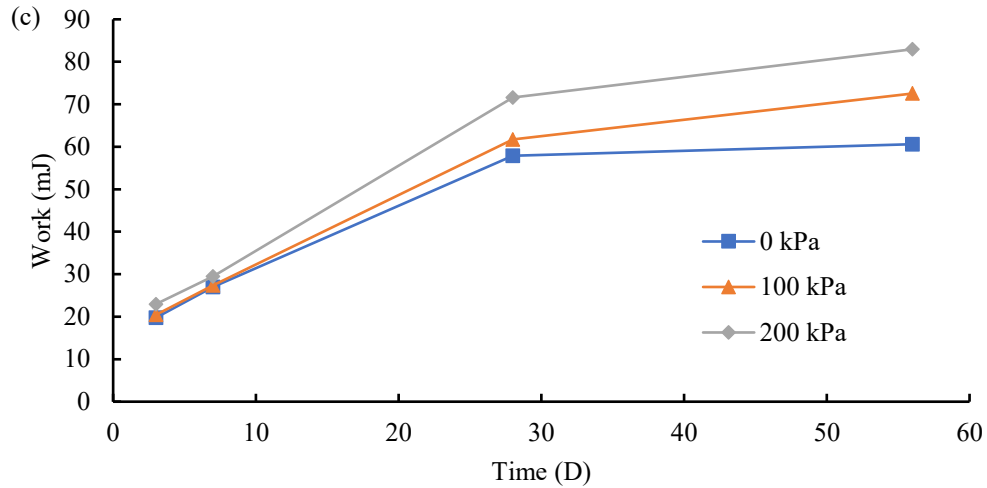


**Figure 4-8.** Effect of curing pressure on evolutive energy of fracture initiation ( $W_c$ ) of CPB under (a) mode-I, (b) mode-II, and (c) mode-III loadings.

As discussed in section 3.6.3, the values calculated for fracture energy are extensive in nature, dependent on sample size. As the area of fracture varies between modes of failure, a comparison with regard to modes of loading may not be conducted. The changes with respect to time and pressure for each mode of loading, however, may be compared individually. The evolution of fracture energy with respect to each form of loading shows markedly greater increases with respect to curing pressure at advanced ages of 28 days (all modes) and 56 days (mode-I and mode-III). The densification of the bulk matrix under induced curing pressure occurs due to the rearrangement of particles within the mix as a result of the applied pressure and as a result of the increase in hydration product. The reduction of pore sizes leads to the formation of greater amounts of LD and HD-CSH and a reduction of other forms of hydration product. At early ages the particle rearrangement is responsible for the increase in the contact area between tailings and cementitious product; however, the progression of cement hydration as a factor of time leads to the increase in cohesion between particles. As such, the effects of induced curing pressure are seen to a greater degree in the fracture energy at later stages. Higher degrees of hydration lock in the densified matrix resulting in a material with the ability to resist crack propagation to a more significant extent.

#### **4.1.5 Sensitivity analysis of fracture toughness and energy of fracture initiation of CPB to curing pressure**

Fracture toughness ( $K_c$ ) and energy of fracture initiation ( $W_c$ ) were calculated in sections 4.1.3 and 4.1.4. According to the fracture mechanics theory, both  $K_c$  and  $W_c$  can be used to determine the onset of crack initiation. However, it should be pointed out that these two quantities were determined through the same peak force for each curing time and curing pressure. Therefore, it is of theoretical and practical importance to identify the more suitable quantity (among  $K_c$  and  $W_c$ ) for the analytical description of evolutive fracture behavior of FR-CPB under curing pressure. To achieve this objective, it is crucial to quantitatively evaluate the discrepancy in the sensitivity of  $K_c$  and  $W_c$  to changes in curing time and curing pressure. Then, the quantity with a higher degree of sensitivity to curing conditions can be selected as the more suitable candidate for the characterization of fracture behavior of FR-CPB.

To implement such an analysis approach, the prerequisite is to convert the target data ( $K_c$  and  $W_c$ ) into comparable intensive variables. In this regard, the percent increase in  $K_c$  and  $W_c$  is calculated. For the characterization of sensitivity to curing time, the percent increase in  $K_c$  and  $W_c$  was calculated with reference to the values of 3-day FR-CPB under the same curing pressure, respectively. Then, the percent increases in  $K_c$  and  $W_c$  under the same pressure at the same curing time were grouped as a pair of data. Since the obtained pairs of data contain information about the changes in  $K_c$  and  $W_c$ , the data dispersion relative to the 1:1 line can be used to compare the sensitivity of  $K_c$  and  $W_c$  to the curing time. The same calculation method is used to evaluate the discrepancy in the sensitivity of  $K_c$  and  $W_c$  to the curing pressure. Correspondingly, the percent increase in  $K_c$  and  $W_c$  is calculated with reference to the values of FR-CPB without curing pressure (0 kPa) at the same curing time. The comparison of the percent increase in  $K_c$  and  $W_c$  is plotted in Figure 4-9. In terms of similarity, the percent increase data are spread around the 1:1 line, which indicates the  $K_c$  and  $W_c$  change covariantly to curing time (4-9a) and curing pressure (Figure 4-9b). Therefore, both  $K_c$  and  $W_c$  can be used to characterize the evolutive fracture behavior of FR-CPB under curing pressure. Moreover, the percent increase data is sensitive to the curing time and curing pressure. Precisely, an increase in curing time and curing pressure can enlarge the percent increase in  $K_c$  and  $W_c$ , which results in the nonlinear improvement of  $K_c$  and  $W_c$  with curing time and pressure. In terms of discrepancy of a percent increase, it can be seen that the increase in curing time causes the transit of percent increase data from the upper left quadrant to the lower right

quadrant relative to the 1:1 line. Therefore,  $K_c$  shows more rapid changes at an early age, while  $W_c$  possesses a higher rate of change at later ages. However, compared with the effect of curing time, the percent increase data show a relatively uniform distribution around the 1:1 line under different curing pressures. Therefore, there exists a discrepancy in the sensitivity of  $K_c$  and  $W_c$  to the curing time and curing pressure. To quantify the sensitivity discrepancy of  $K_c$  and  $W_c$  to curing conditions, the dispersion of percent increase data is evaluated by the variance (i.e., the average of the squared differences between percent increases in  $K_c$  and  $W_c$ ) (Figure 4-10). It can be observed that the increase in curing time and curing pressure can further enlarge the variability of percent increase data. Therefore, the enhanced data dispersion clearly indicates the necessity to identify a more suitable quantity (between  $K_c$  and  $W_c$ ) for the analysis of fracture behavior of FR-CPB materials.

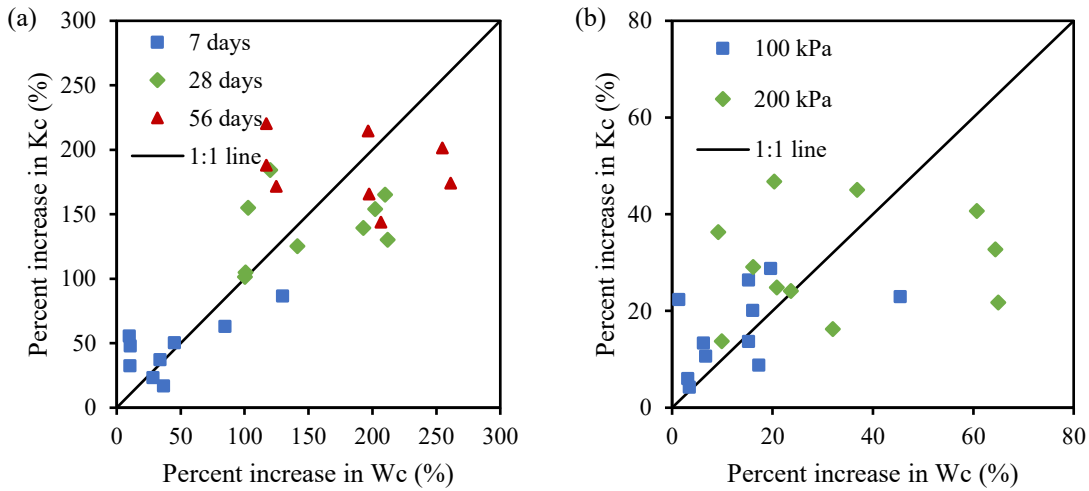


**Figure 4-9.** Comparison of the percent increase in  $K_c$  and  $W_c$  at (a) different curing times and (b) different curing pressures.

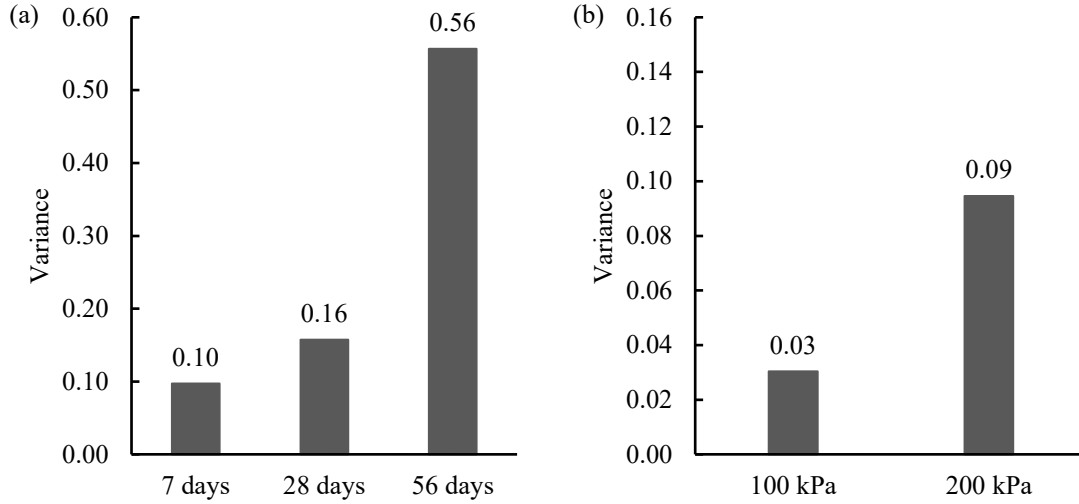


**Figure 4-10.** Comparison of the sensitivity of  $K_c$  and  $W_c$  to (a) curing times and (b) curing pressures.

To identify the more appropriate quantity for the capacitation of fracture behavior of FR-CPB, the sensitivity index ( $S_I$ ) is proposed and defined as follows:

$$S_I = \frac{1}{n} \sum_{i=1}^n \frac{P_{W_i} - P_{K_i}}{|P_{W_i} - P_{K_i}|} \sqrt{(P_{W_i} - \bar{P})^2 + (P_{K_i} - \bar{P})^2} \quad (3)$$

with

$$\bar{P}_i = \frac{P_{W_i} + P_{K_i}}{2}$$

where  $P_W$  and  $P_K$  are the percent increase in  $W_c$  and  $K_c$ , and  $\bar{P}_i$  is the average percent increase for a particular pair of data. The first ratio term in the summation operation acts as a sign function. Through this term, a positive 1 indicates a larger change in  $W_c$  relative to that in  $K_c$ , while a negative 1 implies the changes in  $K_c$  are more sensitive to the curing conditions. The squared root term represents the distance between the data point and 1:1 line and thus the extent of dominance for a particular fracture quantity. As a result, the combined usage of the sign function and squared root term cannot only identify the fracture quantity with a higher sensitivity to curing conditions, but also quantitatively evaluate the extent of sensitivity.

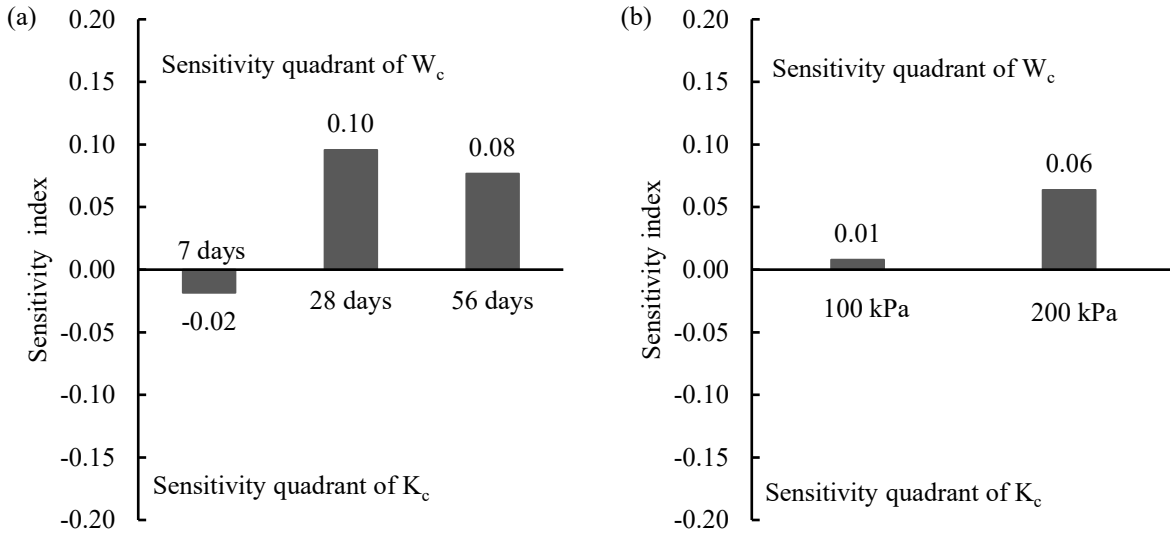
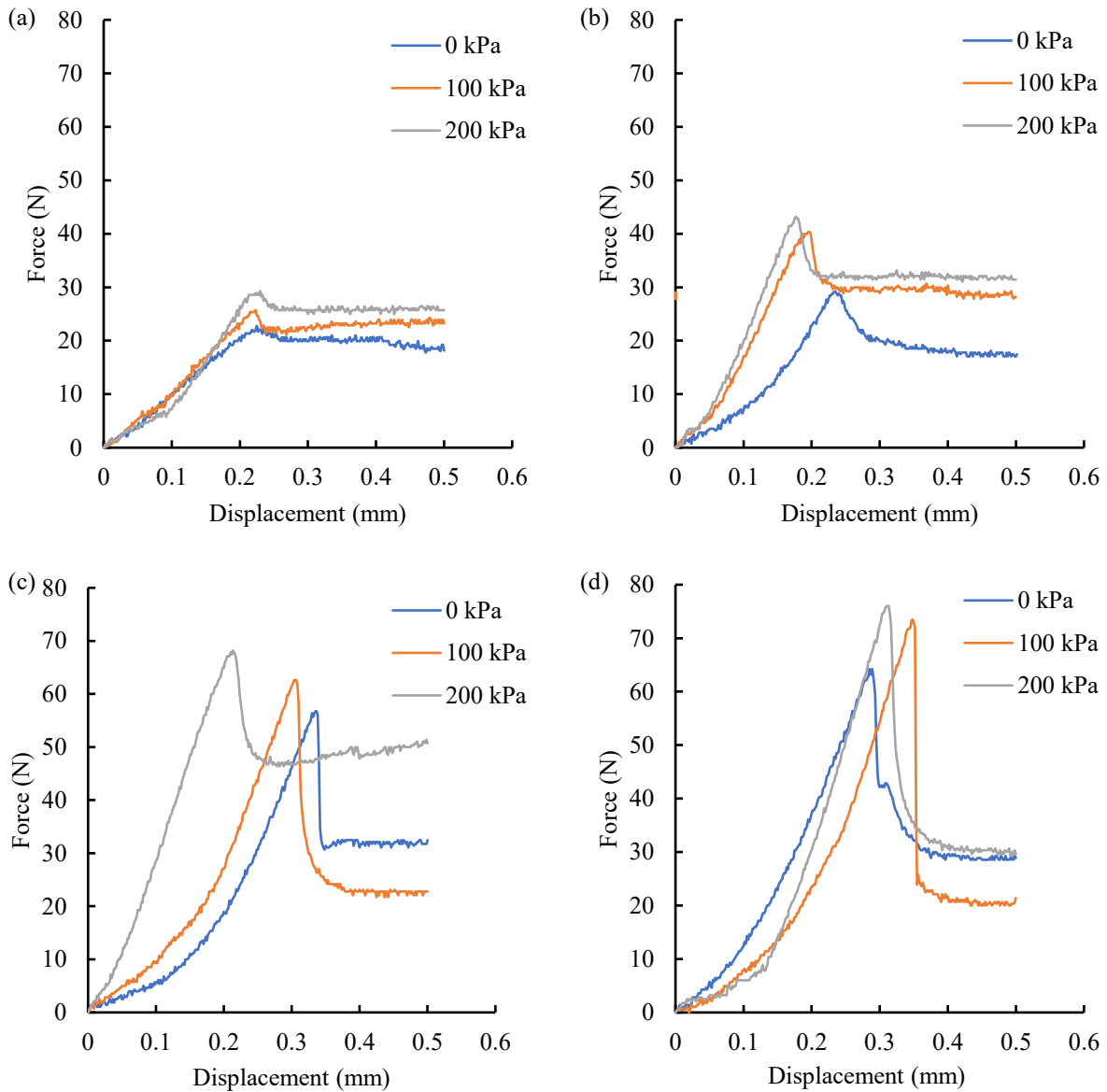


**Figure 4-11.** Comparison of dominant fracture quantities at (a) different curing times, and (b) different curing pressure.

The calculation results of  $S_I$  are presented in Figure 4-11. As shown in Figure 4-11a, it can be seen that the sensitive fracture quantity switch from  $K_c$  to  $W_c$  as curing time increases. Therefore, to capture the effect of curing time, it is more appropriate to select  $K_c$  for early-age FR-CPB and  $W_c$  for advanced-age FR-CPB. Moreover, from Figure 4-11b, it can be seen that when curing pressure increases from 0 kPa (the reference pressure used to calculate percent increase) to 200 kPa, the  $S_I$  shows a more positive value which indicates the stronger curing-pressure sensitivity of  $W_c$  compared with that of  $K_c$ . Consequently, when the induced curing pressure is a concern for the engineering design of CPB,  $W_c$  can be used as a more reliable fracture property to evaluate the fracture behavior of FCPB. Therefore, the proposed sensitivity index ( $S_I$ ) can be used as a valuable tool to qualitatively identify the more suitable fracture quantity and quantitatively evaluate the extent of sensitivity of the selected fracture quantity to curing conditions for the analytical description of fracture initiation in FR-CPB.

## 4.2 Evolutive fracture behavior and properties of FR-CPB under curing pressure

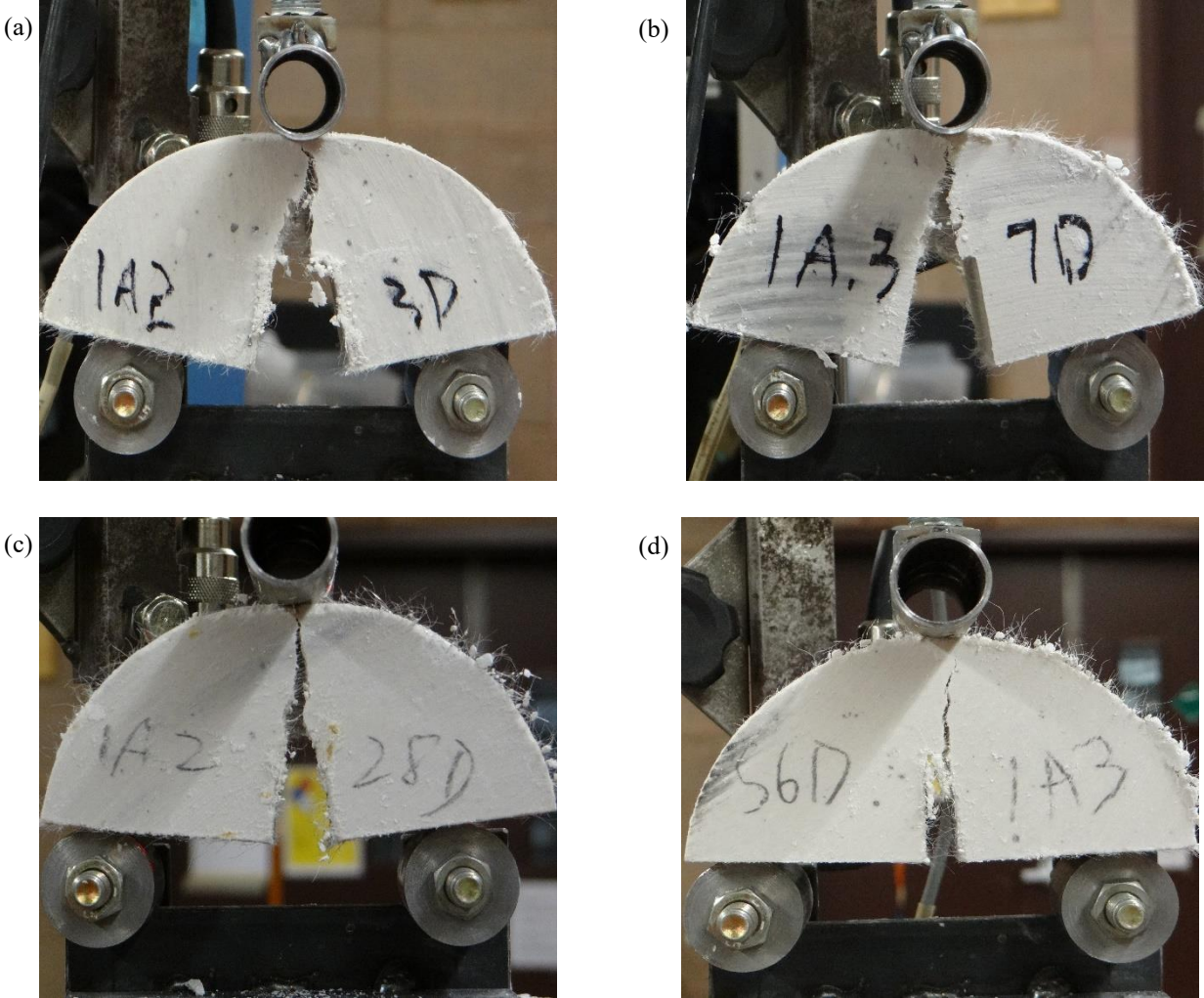
### 4.2.1 Effect of curing pressure on mode-I fracture behavior of FR-CPB



**Figure 4-12.** Effect of curing pressure on the mode-I load-displacement curves at (a) 3 days, (b) 7 days, (c) 28 days, and (d) 56 days.

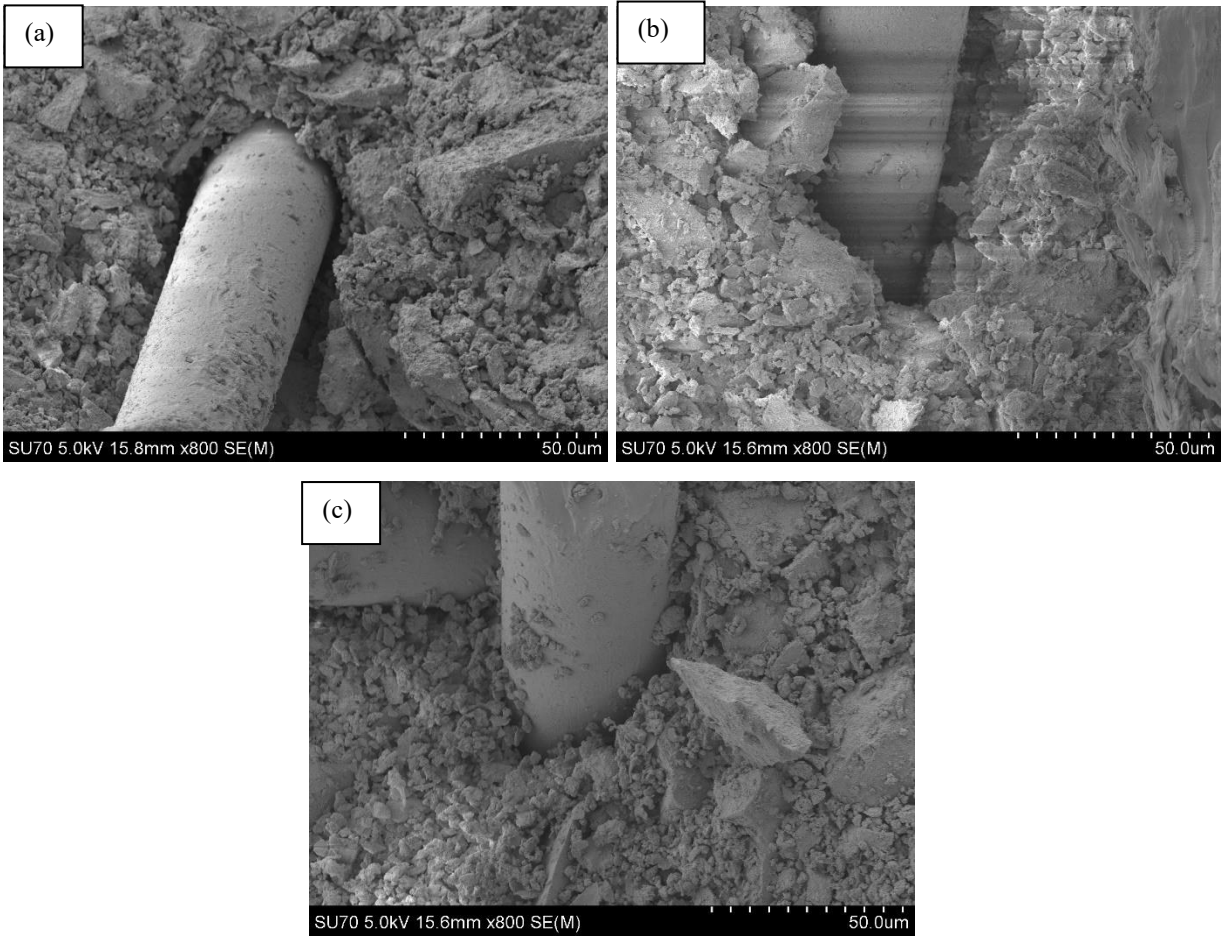
Figure 4-12 presents the evolution of mode-I load-displacement curves with both time and curing pressure. Regarding the time-dependent behavior, it is evident that at any given curing pressure, FR-CPB shows continuous improvement of the pre-peak slope, peak resistance force, and post-peak resistance force. Both bulk matrix and fibers contribute to the fracture behavior of FR-CPB.

The progression of cement hydration improves the interparticle bond strength, which improves the material stiffness and toughness to prevent crack propagation. The stiffer and stronger bulk matrix will also strengthen the fiber-matrix interaction at the post-peak stage at later ages. Moreover, early-age FR-CPB shows more obvious improvement in terms of pre-peak slope and peak resistance force. This is due to the rapid hydration rate at early ages, which results in more hydration products being generated in the FR-CPB matrix. The residual resistance was observed from all FR-CPB specimens at post-peak stages (Figure 4-13).



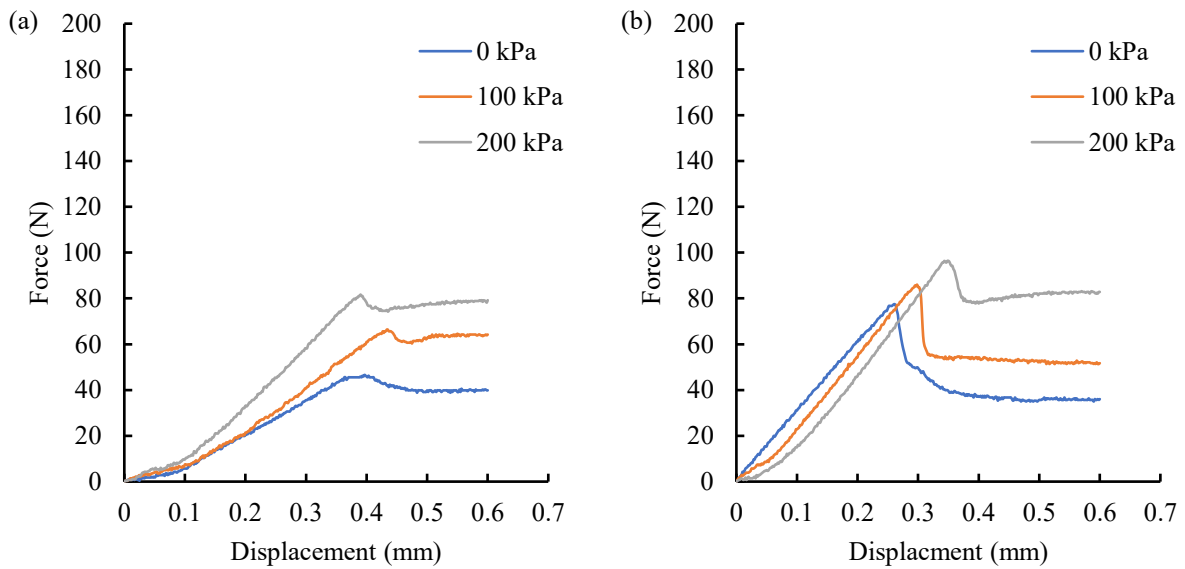
**Figure 4-13.** Fiber bridging across the crack surfaces in FR-CPB under mode-I loading (without curing pressure) at (a) 3 days, (b) 7 days, (c) 28 days, and (d) 56 days.

Regarding the pressure-dependent behavior, it is evident that at any given age, pre- and post-peak branches of the load-displacement curves are sensitive to the changes in curing pressures. An increase in curing pressure can steepen the slope of the load-displacement, increase the peak resistance force, and enhance the post-peak residual resistance. It is believed that these results are a result of the increased density of the bulk matrix of the FR-CPB. This is supported by both the results of dry density evolution presented in section 4.2.2 as well as by the SEM analysis presented in Figure 4-14. The effect of the denser bulk matrix on the fracture behaviors is twofold: First, the denser bulk matrix improves the contact area between tailings particles and thus promotes the formation of interparticle bond strength. Second, the denser bulk matrix generated under higher curing pressure is expected to strengthen the interfacial contact force between fibers and bulk matrix and thus improve the extent of fiber reinforcement, especially at the post-peak stage. However, there exist some differences in the post-peak response of FR-CPB at early and advanced ages. Specifically, the early-age FR-CPB shows a consistent dependency on the curing pressure, i.e., a higher curing pressure is able to yield an enhanced post-peak residual resistance. Meanwhile, the higher curing pressure does not always produce a higher residual resistance at the post-peak stage of advanced-age FR-CPB. This can be attributed to the unstable crack growth after the peak force. The sudden release of strain energy and associated inertial effect may cause severe irreversible damage and catastrophic failure to the CPB matrix in the vicinity of the crack surface. However, under a higher curing pressure, an advanced-age CPB can produce a stronger fracture toughness and thus requires higher critical fracture energy to initiate and propagate the cracks in the matrix. As a result, the advanced-age CPB under a higher curing pressure is expected to suddenly release a considerable amount of strain energy to create the crack surfaces after the onset of crack growth. Consequently, a great extent of post-peak damage can be generated and thus weaken the post-peak residual resistance. Therefore, it can be seen that the FR-CPB under a higher curing pressure may demonstrate a lower residual resistance at later ages (28 and 56 days). As such, curing pressure can dramatically complexify the mode-I fracture behavior of FR-CPB.



**Figure 4-14** Images of microstructure of 28-day FR-CPB matrix at (a) 0 kPa, (b) 100 kPa and (c) 200 kPa.

#### 4.2.2 Effect of curing pressure on mode-II fracture behavior of FR-CPB



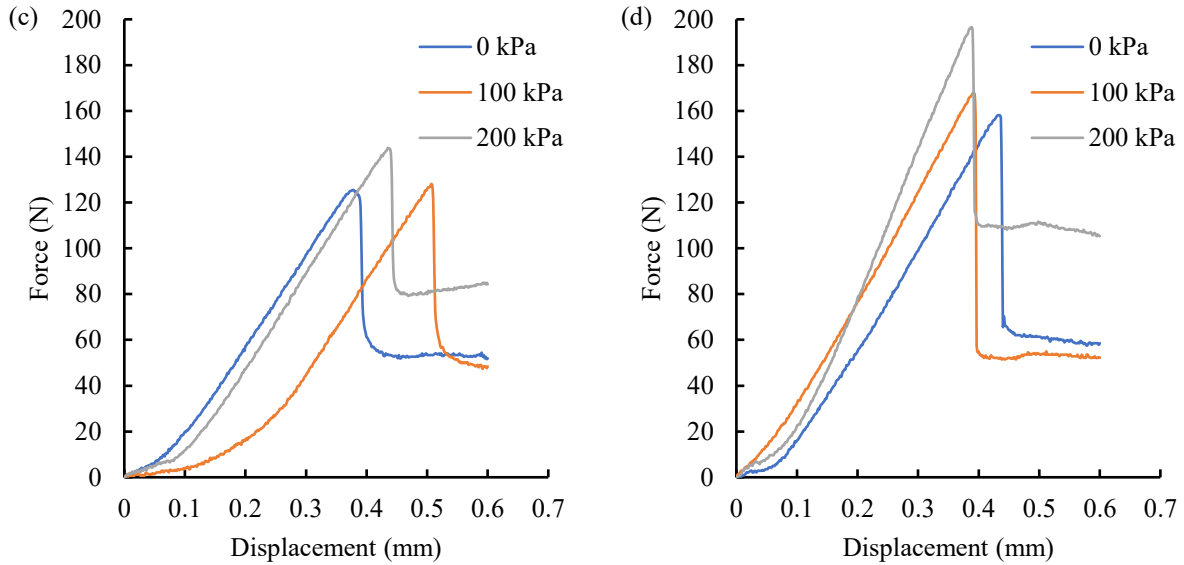
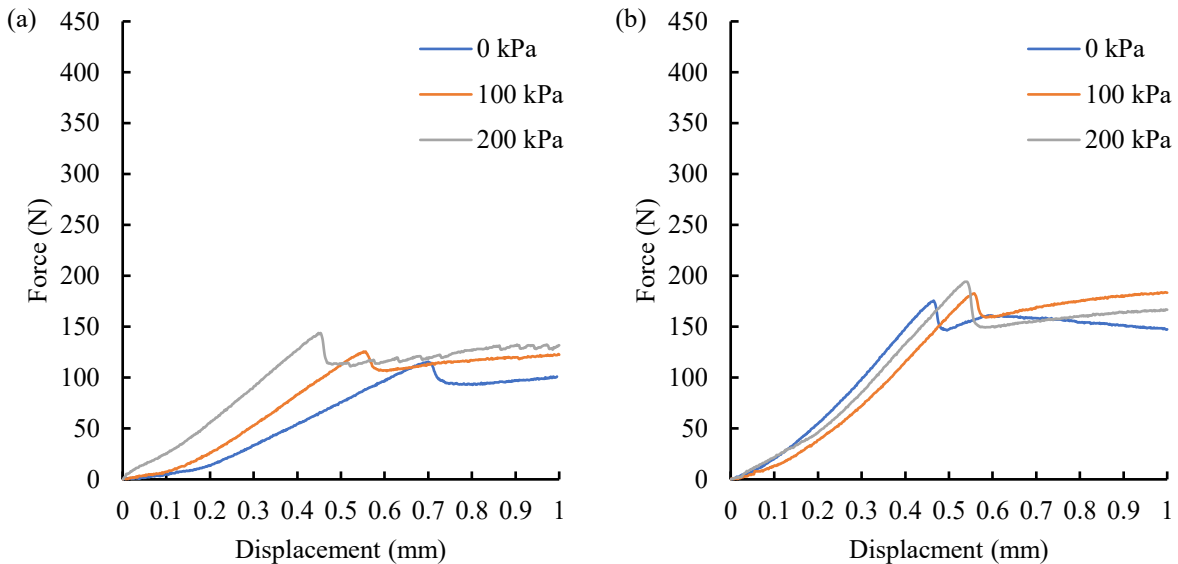


**Figure 4-15.** Effect of curing pressure on the mode-II load-displacement curves at (a) 3 days, (b) 7 days, (c) 28 days, and (d) 56 days.

Regarding pressure-dependent behavior, it is evident that at any given age, the pre-peak branch is more sensitive to curing time compared to that of the post-peak branch. When curing pressure is fixed, a continuous improvement of the slope of the pre-peak and peak force has been measured from early to advanced ages. The curing time dependency of pre-peak behavior clearly indicates the critical role played by the cement hydration in the formation of interparticle bond strength. However, a slight change in post-peak residual resistance under the same curing pressure was measured at all curing times. This is partially due to the loss of non-mobilizable interparticle bond strength along the crack surface after the peak point. As a result, the post-peak mode-II crack propagation is dominated by the interparticle friction resistance. Previous studies have confirmed that particle friction is significantly less sensitive to cement hydration as compared with the changes in the interparticle bond strength. In addition, the fiber bridging effect can also contribute to the post-peak residual resistance to the crack propagation under mode-II loading. However, compared with conventional FRCC, a very low cement content was adopted by CPB materials (cement content of FRCC is typically 3.3 times higher than that used by CPB materials). Therefore, the weak dependency of residual resistance on the curing time (i.e., cement hydration) also indicates that interparticle friction resistance dominates the post-peak fracture behavior compared with the fiber bridging effect.

As curing pressure is increased, we observe an influence on both pre- and post-peak fracture behavior of FR-CPB under mode-II loading. A higher curing pressure has the potential to increase the slope of the pre-peak branch and enhance the post-peak residual resistance. However, compared with changes in the pre-peak branch, curing pressures can influence the post-peak response to a greater extent. When the curing pressure is changed, a noticeable discrepancy in the post-peak residual resistance was detected at all curing times. The early-age FR-CPB consistently shows a higher residual resistance under a larger curing pressure. This is because, the denser CPB matrix formed under a higher curing pressure improves the friction resistance between tailings particles and thus contributes to the improvement of residual resistance. For the advanced-aged FR-CPB, the sudden release of large strain energy can also influence the magnitude of residual resistance, which has been discussed in Section 4.4.2. Based on the measured results, it can be found that under mode-II loading conditions, the pre-peak response of FR-CPB is more sensitive to the curing time, while the curing pressure plays a more critical role in the post-peak response.

#### 4.2.3 Effect of curing pressure on mode-III fracture behavior of FR-CPB



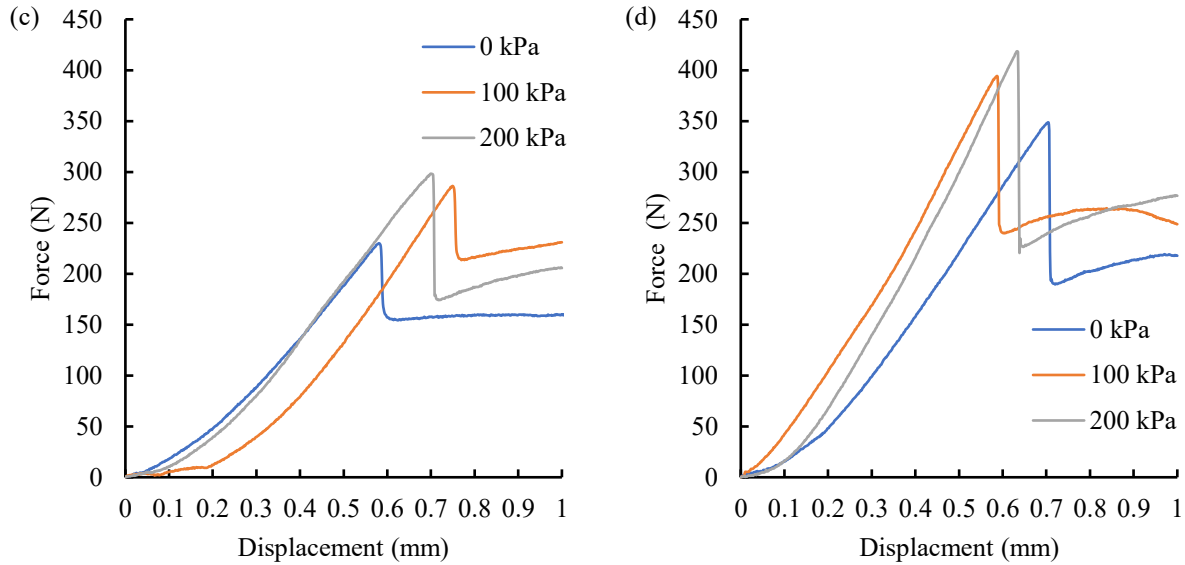


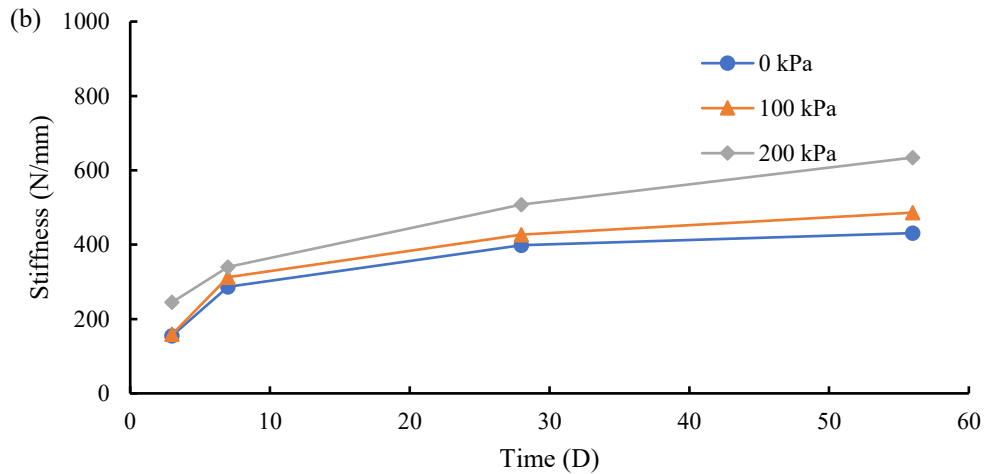
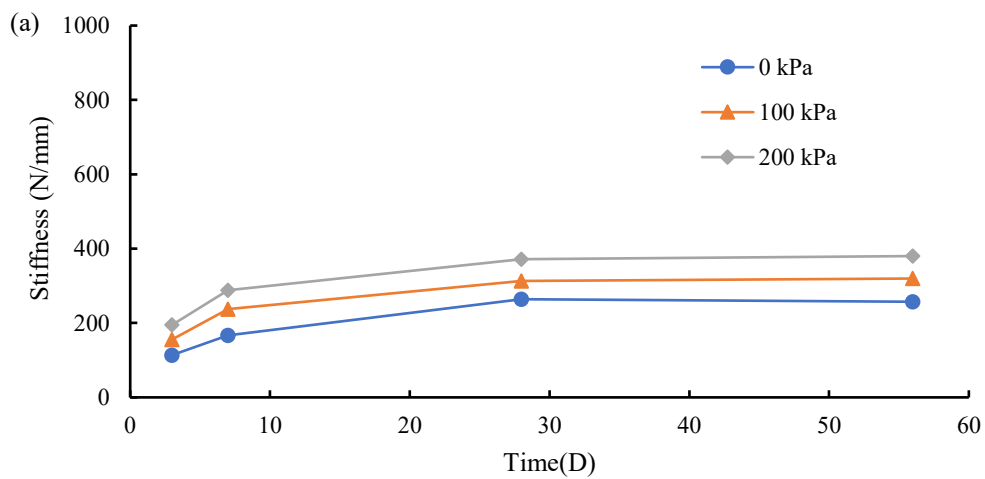
**Figure 4-16.** Effect of curing pressure on the mode-III load-displacement curves at (a) 3 days, (b) 7 days, (c) 28 days, and (d) 56 days.

The formation of unequal principal stresses within the mass of the greater CPB structure results in the formation of in-plane shear stress, which may lead to the propagation of mode-II cracking within the structure. The distribution of these stresses with the subsequent excavation of secondary adjacent stopes results in a loss of confining pressure on the exposed surface allowing for the CPB mass to undergo lateral deformation. This is a result of the surrounding discharge pressure that continues to be exerted on the other faces from the surrounding rock mass. As such, within the vicinity of the rock walls, the propagation of cracking will become parallel to that of the rock wall as torsional loads begin to take effect on the CPB structure. The resultant mode of failure in this instance switches to that of mode-III loading with the forces acting as out-of-plane-shear. This scenario highlights the need to study not only that of the primary and secondary forms of fracture behavior when examining the structural capacity of FR-CPB masses. As with sections 4.2.1 and 4.2.2, the fracture properties of FR-CPB subject to mode-III loading conditions are sensitive to both time and curing pressure. However, when compared to that of the primary and secondary forms of loading, a critical finding is that post-peak pseudo-hardening behavior was observed for mode-III loading at all ages, which indicates a stronger fiber bridging effect is achieved from FR-CPB under the torsional loads. In other words, fiber reinforcement has a more important role in the post-peak fracture behavior under mode-III loading. As a result, the friction resistance between

tailings makes a relatively weak contribution to the post-peak residual resistance, which can be used to interpret the similar residual resistance under mode-III loading. It should be noted that the rock/CPB interface resistance can prevent the local consolidation and leads to the formation of a relatively loose CPB matrix near the rock walls. Therefore, the measured pseudo-hardening behavior under mode-III loading can significantly improve the stability of FR-CPB materials under the rock/CPB interface loading.

#### 4.2.4 Effect of curing pressure on fracture properties of FR-CPB

##### 4.2.4.1 Material Stiffness



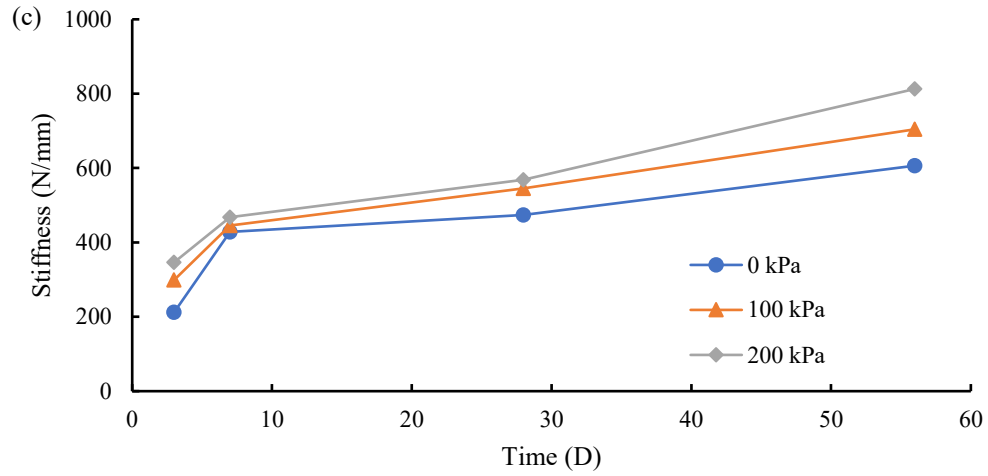


**Figure 4-17.** Effect of curing pressure on evolute stiffness of FR-CPB under (a) mode-I, (c) mode-II, and (c) mode-III loadings.

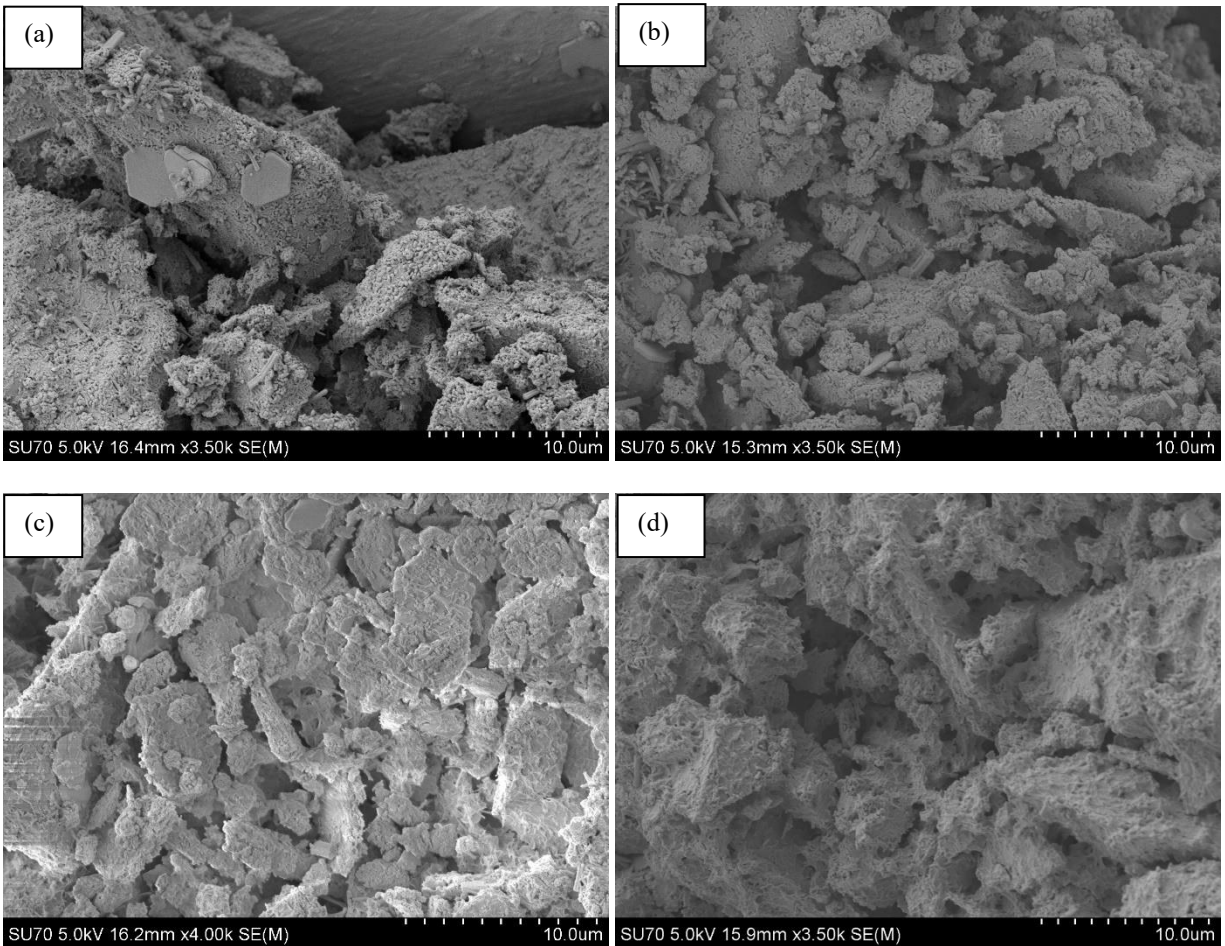


**Figure 4-18.** SEM images of microstructure of control CPB matrix at (a) 3 days, (b) 7 days, (c) 28 days, and (d) 56 days.

It can be observed from Figure 4-17 that there is a continuous improvement of material stiffness across all modes of loading with both increasing pressure and age. Most notably, there is a rapid growth rate at early ages, between 3 and 7 days. It is typical in cementitious materials for both strength and stiffness to follow a logarithmic improvement, the fastest growth rate happening at early ages. However, there are notable differences between stiffness evolution, and loading state observed in CPB. This difference between modes of loading relates to which factors of the mixture take on a dominant role in the development of the material stiffness. For instance, stiffness of FR-CPB shows a typical logarithmic evolution under mode-I loading, which is consistent with changes in hydration rate. Notably, the increases in pressure allow for higher stiffnesses to be achieved at all ages through the densification of the matrix and the increase in hydration products formed as a result of the increased penetration of pore water into the cementitious material. Therefore, cement hydration plays a dominant role in the development of mode-I stiffness of FR-CPB. This may be observed in the microstructural evolution of the control sample with regard to the amount of hydrate products formed over time (Figure 4-18). However, the mode-II and mode-III stiffness show a relatively weak nonlinearity with curing time. Although the elastic response governs the pre-peak branch, the microcracks are inevitably generated in the soft FR-CPB at the pre-peak stage. It has been established in section 2 that failure is a result of fiber pull out rather than rupture. As curing conditions are maintained between modes of loading, the changes in stiffness for mode-II and mode-III are thus contributed to by interparticle friction resistance and locking. Due to the weak sensitivity of friction resistance between tailings particles to the cement hydration process, the logarithmic evolution of mode-II and mode-III stiffness becomes less pronounced. The increase in frictional resistance between fiber and matrix allows for the stiffness to increase to a greater extent at higher ages than that of mode-I loading. In addition, it can be seen that the mode-II and mode-III stiffness are higher than that under mode-I loading, which can further confirm the additional contribution of friction resistance of tailings particles to the pre-peak stiffness. This frictional resistance is a result of the type of loading and the mechanisms engaged (in and out of plane shear).

#### 4.2.4.2 Fracture Toughness

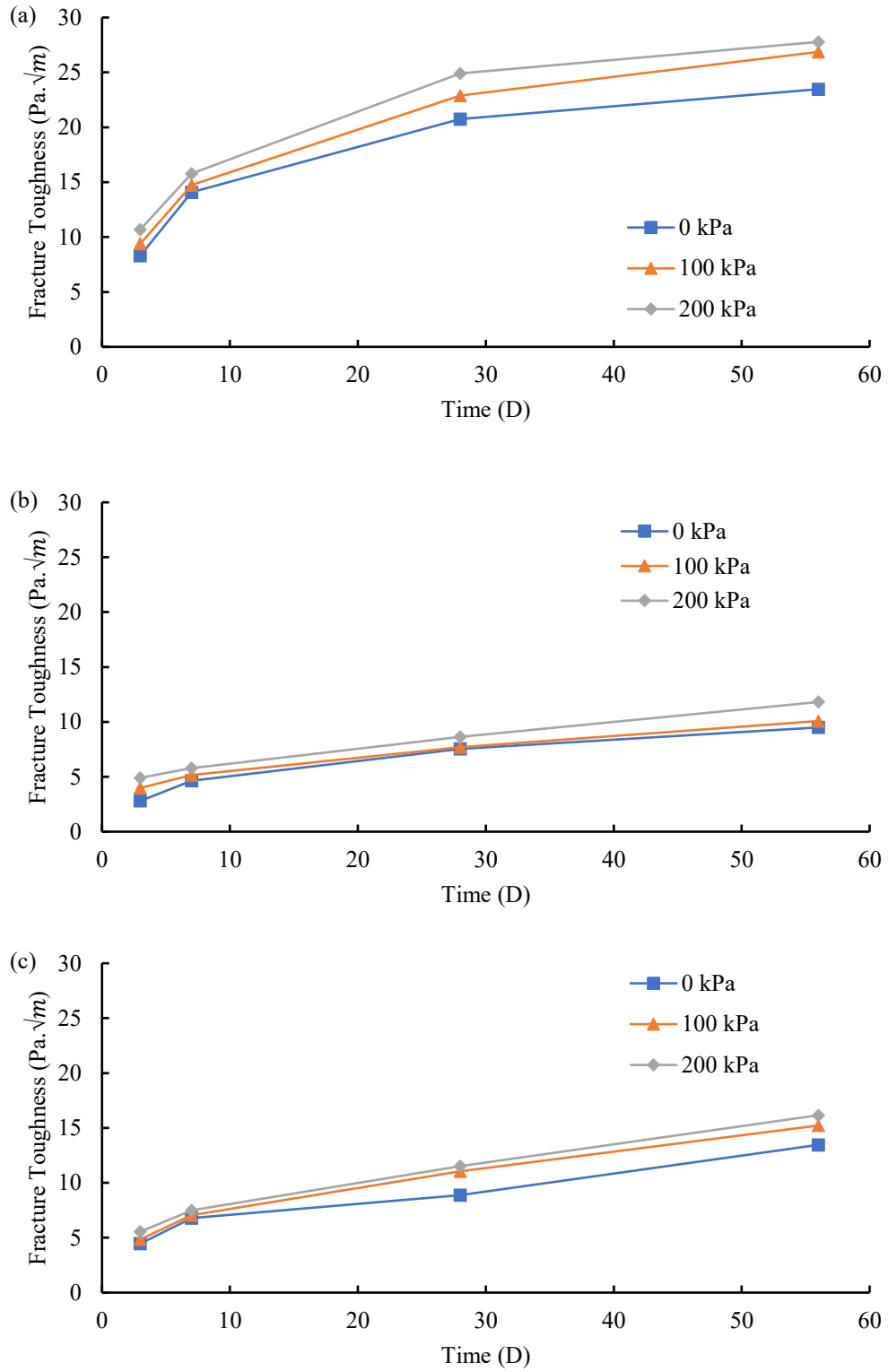


**Figure 4-19.** Effect of curing pressure on evolutive fracture toughness of FR-CPB under (a) mode-I, (c) mode-II, and (c) mode-III loadings.

As discussed in section 4.2.4.1, the differences in the evolution of fracture toughness with time between modes of loading may be attributed to the increased interparticle frictional resistance present in mode-II and mode-III loadings. The logarithmic increases with time for mode-I, and later-age linearity of mode-II and mode-III is even more apparent in the evolution of fracture toughness displayed in Figure 4-19. With regard to the effects of curing pressure on fracture toughness, the SEM imagery in Figure 4-20 shows improvements to the ITZ of fiber and matrix. Most apparent in later age samples but also present in that of early age is an increase in hydration products formed with increased curing pressure distinguishable by the interconnected nature of the CSH gel. This may be attributed to the consolidation of the material and greater penetration of pore water into the cementitious content. The rapid increase in fracture toughness of early age samples (3-7 days) is thought to be related to increases in the density of the material, as supported by prior studies[213]. However, this is not supported by the results reported for density over time in section 4.2.2. However, the mix design for FR-CPB used minimal cement content (0.5%), and thus the correlation between density and hydration may not be adept. The changes in hydrate visible between early ages, as seen in the SEM imagery, support the rapid gain in fracture toughness at this stage of testing. The gradual reduction in the rate of gain for fracture toughness in mode-I loading continues to be supported by its dependency on hydration, the increases in curing pressure increasing packing of the tailings particles, and the formation of hydrate within the pores. The linear increase in fracture toughness for mode-II and mode-III, therefore, further supports the conclusion that curing pressure correlates to greater interparticle friction within the FR-CPB.

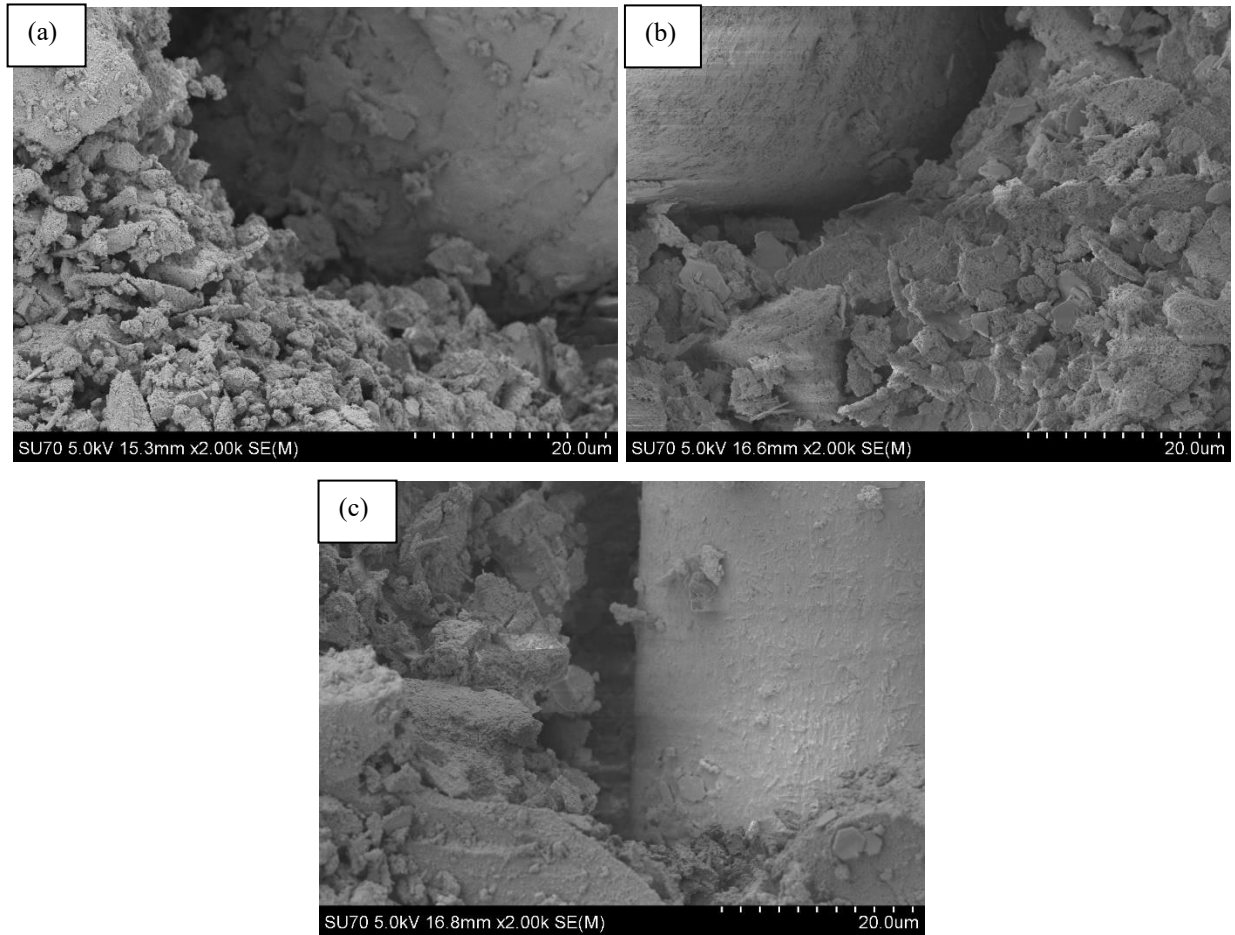


**Figure 4-20** Improvements to the ITZ of fiber and matrix with increasing curing pressure a) 0 kPa b) 100 kPa c) 200 kPa.

In addition to the evolution of fracture toughness, it is of great interest to discover the ratio of fracture toughness ( $K_{II}/K_I$  and  $K_{III}/K_I$ ). As shown in Figure 4-21, the  $K_{II}/K_I$  ratio is in the range of 0.33 to 0.64, while  $K_{III}/K_I$  ratio is in the range of 0.42 to 0.63. Although the magnitude of fracture toughness is sensitive to the changes in curing time and curing pressure, the fracture toughness ratios show a very limited dependency on the curing time and pressure. It should be noted that due to the relatively complex sample fabrication, the shear fracture toughness ( $K_{IIc}$  and  $K_{IIIc}$ ) is difficult to be measured as compared with the measurement of mode-I fracture toughness. The weak dependency of the fracture toughness ratio on curing time and pressure indicates that  $K_{Ic}$  can be used as a reliable quantity to approximate the unknown shear fracture toughness for FR-CPB materials.

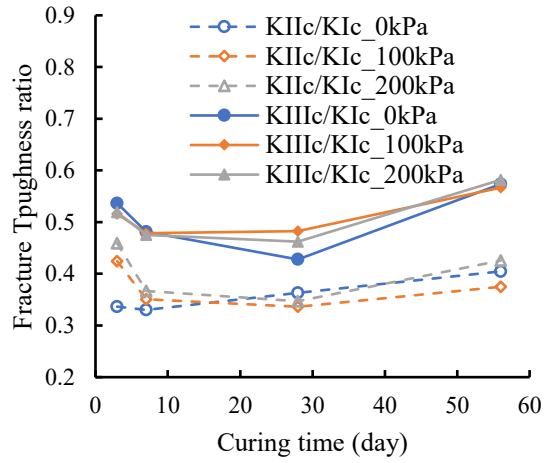
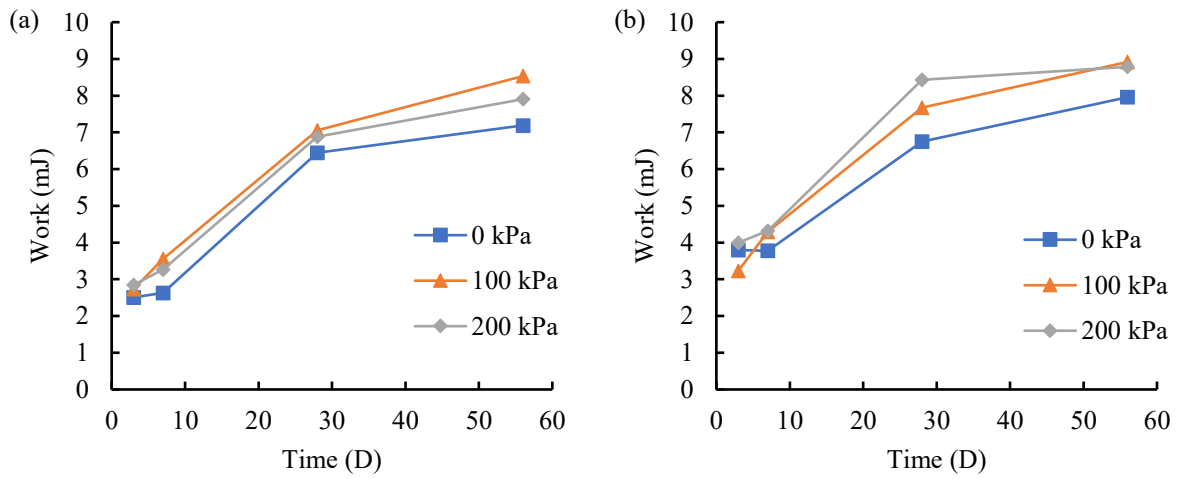
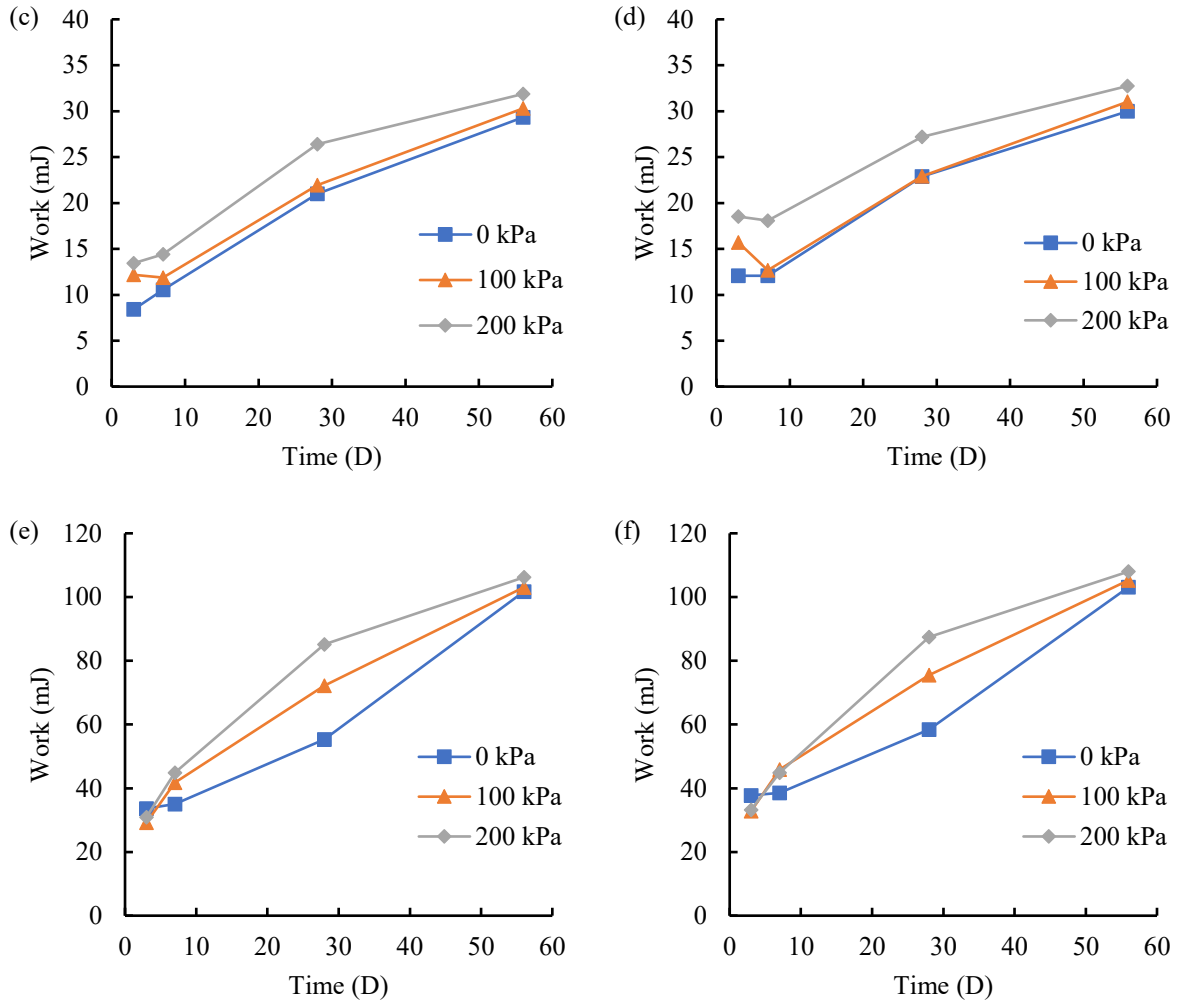


Figure 4-21. Comparison of fracture toughness ratios of FR-CPB.

#### 4.2.4.1 Fracture Energy





**Figure 4-22.** Effect of curing pressure on evolutive energy of fracture initiation ( $W_c$ ) and fracture energy of fiber bridging ( $W_f$ ) of FR-CPB under (a and b) mode-I, (c and d) mode-II, and (e and f) mode-III loadings.

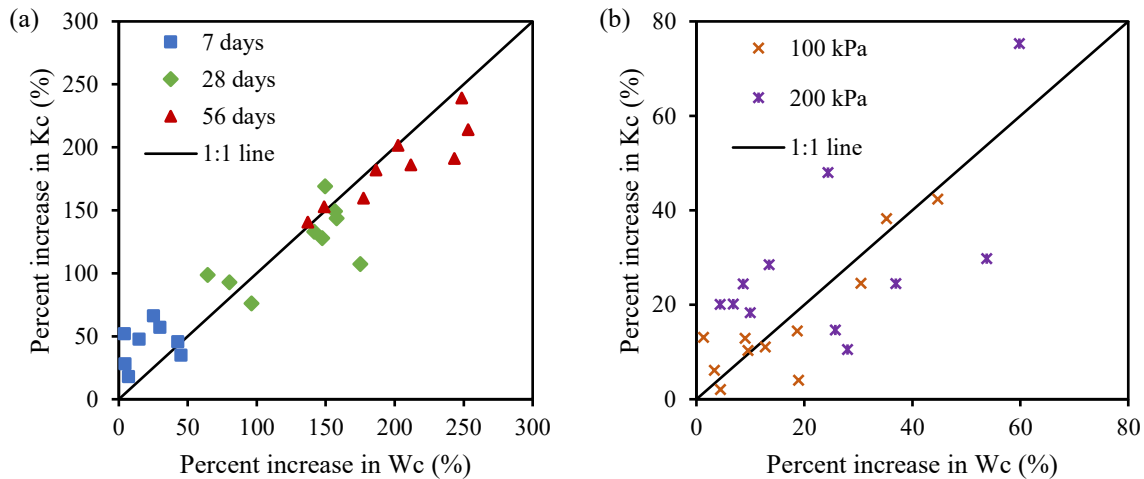
As with sections 4.2.4.1 and 4.2.4.2, the evolution of fracture energy follows similar trends with time for each mode of failure as accounted for by the increase in the bond between fiber and matrix. Strong nonlinear evolution of energy of crack initiation and fiber bridging were measured under mode-I loading when compared to that of mode-II and mode-III loading conditions. The overall values of fracture energy between failure modes cannot be compared directly as the property is extensive in nature, the calculation of the area of failure plane being beyond the scope of this study (refer to section 4.1.4.3). What can be determined from this data is twofold, that the evolution of fracture energy is sensitive to both time and curing pressure. With regard to curing time, FR-CPB is able to dissipate more strain energy at advancing ages and thus further resist the crack propagation in the matrix. The discrepancies between early age samples (3 to 7 days) are a result

of the low cement content and overall malleability of FR-CPB at the 3-day stage. At such stages small discrepancies in fiber distribution throughout the sample and the discontinuous network of hydration products may account for the variability. With regard to curing pressure, it can be seen that higher curing pressure can promote the improvement of fracture energy. The results are consistent with modes -II and -III. However, results of mode -I indicate a decrease in fracture initiation between 100 kPa and 200 kPa. Greater overall stiffness between 100 and 200 kPa without significant overall increases in peak load explains this with the decrease between increasing curing pressure does not present in the corresponding fracture energy of fiber bridging. Increases in energy to fiber bridging can be explained by the enhanced densification process in the bulk matrix and the greater degree of HD-CSH formation, strengthening the bond of both cement to tailings particle and cement to fiber. The densification of the bulk matrix has the ability to form an internal restraint boundary condition surrounding the FM-ITZ. The continued hydration of cement particles under the applied pressure act to form an unremovable confining pressure surrounding the ITZ. As found in prior studies [88-89], the FM-ITZ acts as an intermediary transferring the confining pressure to permanently increase the interfacial contact pressure along the fiber surface. The locked confining pressure boundary condition around the FM-ITZ is more significant at higher curing pressure. The progression of cement hydration, especially that of the smaller CSH hydrate forming within the reduced pore spaces, allows for greater interfacial contact pressure to occur and thus produces higher values for energy to fiber bridging. The fracture energy of fiber bridging ( $W_f$ ) is consistently greater than energy ( $W_c$ ). The obtained results indicate that additional external work is required to fully activate the fiber reinforcement in the CPB matrix after the onset of crack initiation.

#### **4.2.5 Sensitivity analysis of fracture toughness and energy of fracture initiation of FR-CPB to curing pressure**

The sensitivity analyses presented here follow suit with that of the analysis presented in section 4.1.5 using the same equations and methodologies. The comparison of the percent increase in  $K_c$  and  $W_c$  is plotted in Figure 4-23. In terms of similarity, the percent increase data are spread around the 1:1 line, which indicates the  $K_c$  and  $W_c$  change covariantly to curing time (Figure 4-23a) and curing pressure (Figure 4-23b). When compared to that of the analysis presented for CPB, it can be observed that the data is much tighter to the 1:1 line, indicating less of a discrepancy between the sensitivity of  $K_c$  and  $W_c$  to time and pressure. The observed transit of percent increase data

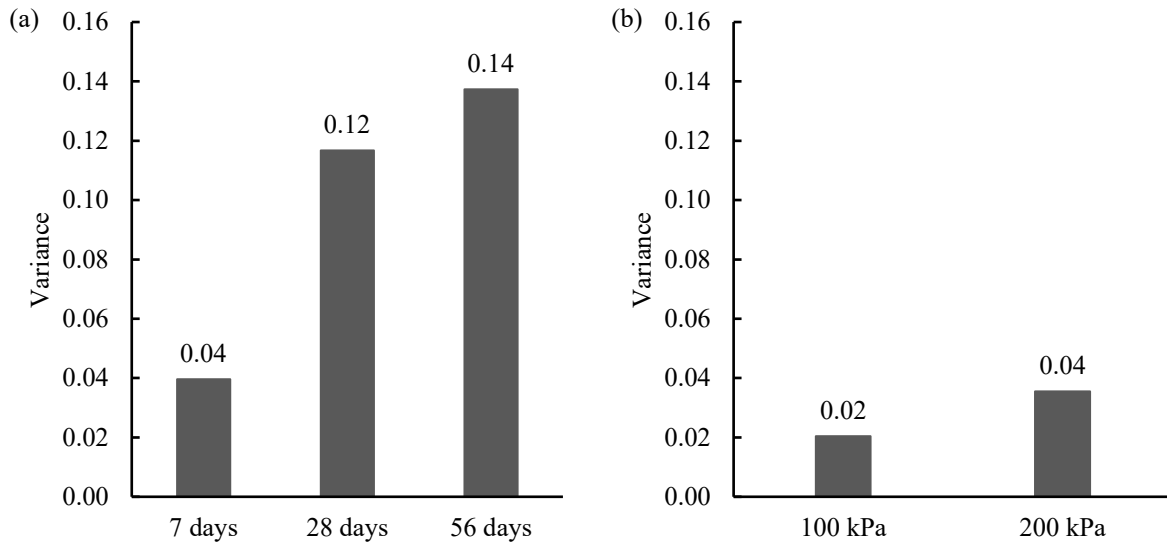
from the upper left quadrant to the lower right quadrant relative to the 1:1 line remains consistent between models, further highlighting that  $K_c$  shows more rapid changes at an early age while  $W_c$  possesses a higher rate of change at later ages. With regard to the individual effects of curing pressure and time, the effects of curing pressure (Figure 4-23b) show less distinction between increases in curing pressure (i.e., the data of 100 kPa and 200 kPa is intermingled) while that of time (Figure 4-23a) shows a formal separation between age and sensitivity of  $K_c$  and  $W_c$ . This highlights the greater significance of time when compared to that of pressure on the evolution of fracture properties for CPB material. Alternatively, this may also signify the need to increase the intervals of curing pressure when conducting testing.



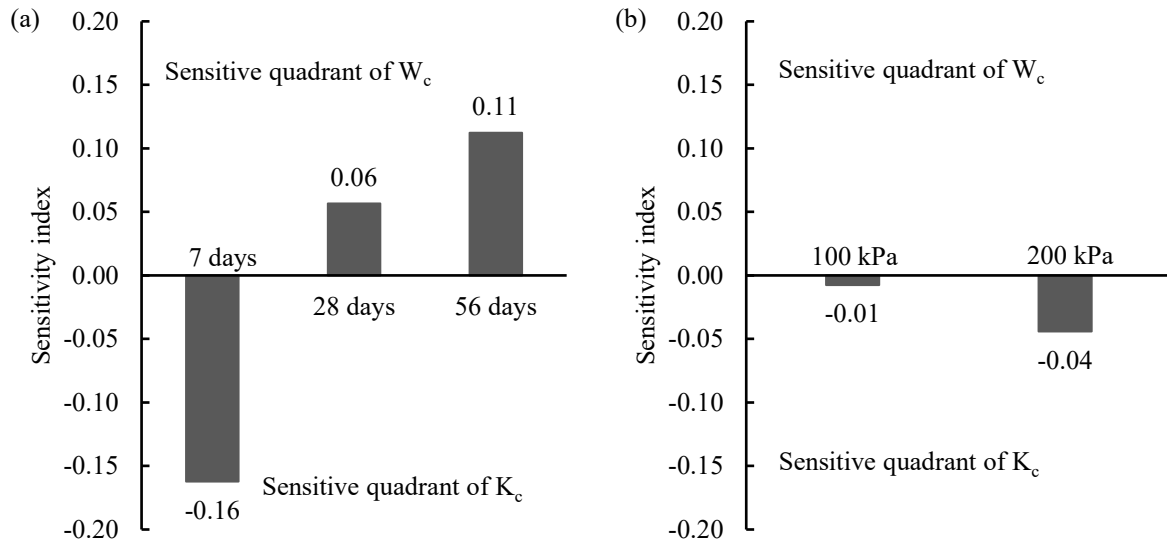
**Figure 4-23.** Comparison of the percent increase in  $K_c$  and  $W_c$  at (a) different curing times and (b) different curing pressures.

Figure 4-24 presents the variance in the dispersion of percent increase data as a means to quantify the sensitivity discrepancy of  $K_c$  and  $W_c$  to curing conditions. It can be observed that an increase in curing time can further enlarge the variability of percent increase data. While less significant when compared to curing time, similar results exist when comparing the variability when curing pressure is increased. As with section 4.1.5, a sensitivity index was thus calculated (Figure 4-25) as a means to determine the most suitable factor for analysis of the fracture properties of FR-CPB. As shown in Figure 4-25a, it can be seen that the sensitive fracture quantity switches from  $K_c$  to  $W_c$  as curing time increases. Therefore, to capture the effect of curing time, it is more appropriate to select  $K_c$  for early-age FR-CPB and  $W_c$  for advanced-age FR-CPB. Meanwhile, it can also be observed that the absolute value of early-age  $S_I$  is greater than that at advanced ages, which

indicates the significant contribution of early-age cement hydration to the development of fracture properties. Moreover, from Figure 4-25b, it can be seen that when curing pressure increases from 0 kPa (the reference pressure used to calculate percent increase) to 200kPa, the  $S_I$  shows a more negative value which indicates the stronger curing-pressure sensitivity of  $K_c$  compared with that of  $W_c$ . Consequently, when the induced curing pressure is a concern for the engineering design of FR-CPB,  $K_c$  can be used as a more reliable fracture property to evaluate the fracture behavior of FR-CPB.



**Figure 4-24.** Comparison of the sensitivity of  $K_c$  and  $W_c$  to (a) curing times and (b) curing pressures.



**Figure 4-25.** Comparison of dominant fracture quantities at (a) different curing times, and (b) different curing pressure.

## Chapter 5                      Conclusions and recommendations

### 5.1 Conclusions

This study investigated the effects of induced curing pressure on the evolution of fracture properties of FR-CPB. As such, an extensive experimental testing program was conducted on both CPB and FR-CPB samples with the progression of time (3, 7, 28, and 56 days) and increasing curing pressure (0 kPa, 100 kPa, and 200 kPa). Using load-displacement analysis, the evolution of material stiffness fracture toughness, the energy of crack initiation, and energy to fiber bridging were determined under modes -I, -II, and -III loading conditions. Auxiliary analysis of material density and microscopic evolution (through SEM analysis) was also performed as a means of supporting analysis. Results of the testing program have shown curing pressure to increase the fracture properties of FR-CPB to varying degrees at all curing durations and under all modes of loading. Based on the results obtained, the concluding findings of this study are thus as follows:

1. The fracture behavior of FR-CPB under each mode of loading proved sensitive to both curing pressure and curing time. While similar improvements were noted across all modes of loading, the behavior of the material under each mode of loading also exhibited unique attributes. Residual strength of early-age FR-CPB under mode-I loading showed a consistent dependency on curing pressure, while that of advanced ages demonstrated a weakened post-peak response. This highlights the considerable amount of strain energy required to initiate cracking and the sudden release of energy at failure under mode-I loading. At advanced ages, the material exhibited greater strengths but was correspondingly more brittle in nature as demonstrated by the heightened material stiffness and reduction of post-peak strength at advanced ages. Mode-II loading demonstrated a greater pre-peak dependency on time and greater post-peak dependency on pressure. The curing time dependency of pre-peak behavior indicates the critical role played by the cement hydration in the formation of interparticle bond strength. The effects of curing pressure contribute more to the post-peak response. Unlike the primary and secondary modes of loading, Mode-III loading exhibited pseudo-hardening behavior across all ages and curing pressures, indicating a stronger fiber bridging effect is achieved from FR-CPB under the torsional loads

2. Material stiffness of FR-CPB shows continuous improvements with both increased curing pressure and age. Across all modes of loading, a sharp increase in material stiffness is present between 3- and 7-day samples. This gain in material stiffness is easily attributed to the rapid progression of cement hydration at early ages. A significant conclusion from this research is the progression of material from 7- to 56- days. The progression under mode-I loading conditions follows a logarithmic trend similar to that of cement hydration, the effects of induced curing pressure increasing the material stiffness on average by 50% across all ages of curing. This highlights the dependency of mode -I material stiffness on the progression of cement hydration. With respect to modes -II and -III loading conditions, the progression of material stiffness relies upon the added contribution of interparticle friction resistance and locking of the fiber and matrix. Each mode of failure shows a greater percentage increase of material stiffness with respect to time when comparing results of 0 and 200 kPa. The benefits of fiber reinforcement are thus emphasized in the absence of similar continuous increases in ordinary CPB samples.
3. Fracture toughness of FR-CPB shows continuous improvement with both increased curing pressure and age. The increase in fracture toughness as a result of curing pressure is resultants of particle rearrangement and densification of the matrix. This is supported through SEM imagery and calculations of dry density. SEM imagery of FR-CPB samples at the age of 28 days showed a greater degree of interconnection between hydration product and tailings particles within the ITZ. A reduction in ettringite and CH along with higher volumes of CSH were noted. The reduction in pore spaces promotes the formation of CSH and potentially the development of greater degrees of HD-CSH as a result of increased penetration of pore water.
4. Although the magnitude of fracture toughness is sensitive to the changes in curing time and curing pressure, the ratios of fracture toughness between modes of loading showed a very limited dependency. The  $K_{II}/K_I$  ratio was found to be in the range of 0.33 to 0.64, and the  $K_{III}/K_I$  ratio in the range of 0.42 to 0.63. This limited dependency thus indicates the potential for mode-I fracture toughness to be used as a reliable quantity to approximate the fracture toughness of modes -II and -III for FR-CPB materials.
5. Consistent increases in the dissipation of strain energy were found for FR-CPB samples with the progression of curing, thus underlining the enhanced ability of FR-CPB to resist the

propagation of cracking at advanced ages. The effect of curing pressure on the energy of crack initiation was also found to increase the energy dissipation of FR-CPB samples with noted discrepancy for mode-I loading, the results of the 100 kPa analysis being greater than that of the 200 kPa. The addition of fiber reinforcement was found to increase the energy of crack initiation on average 76%, 59%, and 31%, respectively, under curing pressures of 0 kPa, 100 kPa, and 200 kPa.

6. With exception to results presented for 3-day curing time, the analysis of energy exerted to fully activate the fiber reinforcement within the FR-CPB material after the onset of crack initiation is greater with both curing pressure and time. The continued hydration of cement particles in conjunction with applied pressure creates an unremovable confining pressure around the FM-ITZ. The reduction in void spaces through densification of the matrix allows for the progression of CSH within the pore spaces creating greater interfacial contact pressure to occur between fiber and matrix. The exerted energy required to reach the pseudo-strain hardening stage is thus greater, with increased curing pressure representing a greater residual strength within the FR-CPB material.
7. When compared to the sensitivity analysis of CPB, it was observed that the data itself was much tighter to the 1:1 line, indicating less of a discrepancy between the sensitivity of  $K_c$  and  $W_c$  to time and pressure. As such, the fracture properties have more significance to the fiber-inclusive material. The sensitivity analysis of FR-CPB indicated that  $K_c$  and  $W_c$  change covariantly to both time and curing pressure. With regard to curing time, the dominant sensitivity index changed from  $K_c$  to  $W_c$  from early to advanced ages. As such, it is more appropriate to select  $K_c$  for early-age FR-CPB and  $W_c$  for advanced-age FR-CPB. However, with respect to the greatest sensitivity to curing time, that of the early age sensitivity to  $K_c$  produced the highest absolute value indicating the significant contribution of early-age cement hydration to the development of fracture properties. The dominant index with respect to curing pressure was  $K_c$ . As such, when the induced curing pressure is a concern for the engineering design of FR-CPB,  $K_c$  can be used as a more reliable fracture property to evaluate fracture behavior.

## 5.2 Recommendations for future work

While the conclusions drawn from this investigation meaningfully increase the understanding of the fracture behavior of FR-CPB under induced curing pressure, the opportunity for continued research will always remain. The author hopes that this study aids in the continued growth of understanding of FR-CPB, allowing for further research into the effects of curing pressure on the in-situ material. As such, the following recommendation for the continued investigation of the topic are as follows:

1. An independent investigation into the shear behavior of FR-CPB under induced curing pressure focuses on the effects of the confining boundary formed around the FM-ITZ and thus the increase in interfacial contact pressure between fiber and matrix. An understanding of the evolution of interfacial contact pressure with respect to time (under induced curing pressure) can provide valuable insights into the contribution of the property to the overall fracture behavior of FR-CPB.
2. Refinement of the pressure curing apparatus to allow for the investigation of greater induced curing pressures. The volume of CPB placed may far exceed that of the volumes modeled under 200 kPa curing conditions. Studies on similarly constituted materials such as that cemented soils have noted degradation of the matrix at higher induced pressures. As such, it is of interest to investigate the effects of greater pressures on the fracture behaviors of FR-CPB
3. Staged progression of pressure application and its effects on fracture behavior of FR-CPB. Previous studies have emphasized the effects of fill cycles on not only the pressure development within CPB structures but also on the microstructural evolution of the material properties. The rearrangement of tailing particles at early ages under induced curing pressure is locked in with the progression of cement hydration over time. As such, investigating the rate of application of pressure on the fracture behavior of FR-CPB may better represent that of in-situ conditions.
4. Using the obtained experimental data of FR-CPB under induced curing pressure, a numerical analysis of the effects of induced curing pressure on the fracture behavior of FR-CPB may be established. While the objective of this study was to create a low-cost pressure curing system capable of simulating in-situ conditions, the ultimate goal of this research would be to create a

mathematical model capable of quantitatively predicting the fracture properties of FR-CPB based on the presented in-situ conditions.

5. This study validated the benefits of fiber reinforcement in CPB, showing the evolution of FR-CPB fracture properties under induced curing pressure. Based on such data, an analysis of the capabilities of natural fibers in lieu of synthetic fiber would aid in the continued understanding of the capabilities of FR-CPB. Recognizing the cost associated with the inclusion of fiber reinforcement, further testing with economic fiber inclusion, such as that of natural fibers, may allow for a greater application of FR-CPB in the mining industry.

## References

- [1] S. feng WANG *et al.*, “Non-explosive mining and waste utilization for achieving green mining in underground hard rock mine in China,” *Trans. Nonferrous Met. Soc. China (English Ed.*, vol. 29, no. 9, pp. 1914–1928, 2019, doi: 10.1016/S1003-6326(19)65099-5.
- [2] C. Qi and A. Fourie, “Cemented paste backfill for mineral tailings management: Review and future perspectives,” *Minerals Engineering*, vol. 144. pp. 106–125, 2019. doi: 10.1016/j.mineng.2019.106025.
- [3] W. Xu, R. Zhao, X. Yang, L. Guo, C. Xie, and D. Wu, “Coupled Effect of Curing Temperature and Moisture on THM Behavior of Cemented Paste Backfill,” *Adv. Civ. Eng.*, vol. 2020, 2020, doi: 10.1155/2020/1870952.
- [4] N. Liu, L. Cui, and Y. Wang, “Analytical Assessment of Internal Stress in Cemented Paste Backfill,” *Adv. Mater. Sci. Eng.*, vol. 2020, 2020, doi: 10.1155/2020/6666548.
- [5] T. Belem and M. Benzaazoua, “Design and application of underground mine paste backfill technology,” *Geotechnical and Geological Engineering*, vol. 26, no. 2. pp. 147–174, 2008. doi: 10.1007/s10706-007-9154-3.
- [6] L. Henrique *et al.*, “Int J Appl Earth Obs Geoinformation The 2019 Brumadinho tailings dam collapse : Possible cause and impacts of the worst human and environmental disaster in Brazil,” vol. 90, no. April, 2020, doi: 10.1016/j.jag.2020.102119.
- [7] C. Qi and A. Fourie, “Cemented paste backfill for mineral tailings management: Review and future perspectives,” *Miner. Eng.*, vol. 144, no. September, 2019, doi: 10.1016/j.mineng.2019.106025.
- [8] S. Guo, M. Fall, and S. Haruna, “Interface Shear Behavior of Cementing Underground Mine Backfill,” *Int. J. Geomech.*, vol. 20, no. 12, pp. 1–17, 2020, doi: 10.1061/(asce)gm.1943-5622.0001852.
- [9] M. Edraki, T. Baumgartl, E. Manlapig, D. Bradshaw, D. M. Franks, and C. J. Moran, “Designing mine tailings for better environmental , social and economic outcomes : a review of alternative approaches,” *J. Clean. Prod.*, vol. 84, pp. 411–420, 2014, doi:

10.1016/j.jclepro.2014.04.079.

- [10] K. Klein and D. Simon, “Effect of specimen composition on the strength development in cemented paste backfill,” vol. 324, pp. 310–324, 2006, doi: 10.1139/T06-005.
- [11] A. Kesimal, E. Yilmaz, B. Ercikdi, I. Alp, and H. N. Deveci, “Effect of properties of tailings and binder on the short-and long-term strength and stability of cemented paste backfill,” vol. 59, pp. 3703–3709, 2005, doi: 10.1016/j.matlet.2005.06.042.
- [12] M. L. Walske, H. McWilliam, J. Doherty, and A. Fourie, “Influence of curing temperature and stress conditions on mechanical properties of cementing paste backfill,” *Can. Geotech. J.*, vol. 53, no. 1, pp. 148–161, 2016, doi: 10.1139/cgj-2014-0502.
- [13] J. P. Doherty, A. Hasan, G. H. Suazo, and A. Fourie, “Investigation of some controllable factors that impact the stress state in cemented paste backfill,” *Can. Geotech. J.*, vol. 52, no. 12, pp. 1901–1912, 2015, doi: 10.1139/cgj-2014-0321.
- [14] B. Koohestani, A. Koubaa, T. Belem, B. Bussière, and H. Bouzahzah, “Experimental investigation of mechanical and microstructural properties of cemented paste backfill containing maple-wood filler,” *Constr. Build. Mater.*, vol. 121, pp. 222–228, 2016, doi: 10.1016/j.conbuildmat.2016.05.118.
- [15] N. C. Consoli, H. P. Nierwinski, A. Peccin da Silva, and J. Sosnoski, “Durability and strength of fiber-reinforced compacted gold tailings-cement blends,” *Geotext. Geomembranes*, vol. 45, no. 2, pp. 98–102, 2017, doi: 10.1016/j.geotexmem.2017.01.001.
- [16] X. Chen *et al.*, “Fiber-reinforced cemented paste backfill: The effect of fiber on strength properties and estimation of strength using nonlinear models,” *Materials (Basel)*, vol. 13, no. 3, pp. 1–21, 2020, doi: 10.3390/ma13030718.
- [17] G. Xue, E. E. Yilmaz, W. Song, and E. E. Yilmaz, “Influence of fiber reinforcement on mechanical behavior and microstructural properties of cemented tailings backfill,” *Constr. Build. Mater.*, vol. 213, pp. 275–285, 2019, doi: 10.1016/j.conbuildmat.2019.04.080.
- [18] G. Xue, E. Yilmaz, G. Feng, and S. Cao, “Analysis of tensile mechanical characteristics of fibre reinforced backfill through splitting tensile and three-point bending tests,” *Int. J. Mining, Reclam. Environ.*, vol. 36, no. 3, pp. 218–234, Mar. 2022, doi:

10.1080/17480930.2021.2014693.

- [19] X. W. Yi, G. W. Ma, and A. Fourie, “Compressive behaviour of fibre-reinforced cemented paste backfill,” *Geotext. Geomembranes*, vol. 43, no. 3, pp. 207–215, 2015, doi: 10.1016/j.geotexmem.2015.03.003.
- [20] X. Chen, X. Shi, J. Zhou, Q. Chen, E. Li, and X. Du, “Compressive behavior and microstructural properties of tailings polypropylene fibre-reinforced cemented paste backfill,” *Constr. Build. Mater.*, vol. 190, pp. 211–221, 2018, doi: 10.1016/j.conbuildmat.2018.09.092.
- [21] G. Xue, E. Yilmaz, W. Song, and S. Cao, “Mechanical, flexural and microstructural properties of cement-tailings matrix composites: Effects of fiber type and dosage,” *Compos. Part B Eng.*, vol. 172, no. December 2018, pp. 131–142, 2019, doi: 10.1016/j.compositesb.2019.05.039.
- [22] A. Ghirian and M. Fall, “Coupled Behavior of Cemented Paste Backfill at Early Ages,” *Geotech. Geol. Eng.*, vol. 33, no. 5, pp. 1141–1166, 2015, doi: 10.1007/s10706-015-9892-6.
- [23] X. Chen, X. Shi, J. Zhou, and Z. Yu, “Influence of Polypropylene Fiber Reinforcement on Tensile Behavior and Failure Mode of Tailings Cemented Paste Backfill,” *IEEE Access*, vol. 7, pp. 69015–69026, 2019, doi: 10.1109/ACCESS.2019.2919480.
- [24] B. D. Thompson, W. F. Bawden, and M. W. Grabinsky, “In situ measurements of cemented paste backfill at the Cayeli mine,” *Can. Geotech. J.*, vol. 49, no. 7, pp. 755–772, 2012, doi: 10.1139/T2012-040.
- [25] K. Le Roux, W. F. Bawden, and M. F. Grabinsky, “Field properties of cemented paste backfill at the Golden Giant mine,” *Inst. Min. Metall. Trans. Sect. A Min. Technol.*, vol. 114, no. 2, pp. 65–80, 2005, doi: 10.1179/037178405X44557.
- [26] B. Thompson, M. Grabinsky, R. Veenstra, and W. Bawden, “In situ pressures in cemented paste backfill — a review of fieldwork from three mines,” *Proc. 14th Int. Semin. Paste Thick. Tailings*, pp. 491–503, 2011, doi: 10.36487/acg\_rep/1104\_42\_thompson.
- [27] T. Belem, O. El Aatar, B. Bussiere, M. Benzaazoua, M. Fall, and E. Yilmaz,

- “Characterisation of Self-Weight Consolidated Paste Backfill,” *Proc. Ninth Int. Semin. Paste Thick. Tailings*, pp. 333–345, 2006, doi: 10.36487/acg\_repo/663\_29.
- [28] J. Cayouette, “Optimization of paste backfill plant at Louvicourt mine,” *CIM Bull.*, vol. 96, no. 1075, pp. 51–57, 2003.
- [29] M. Revell, “Paste—how strong is it?,” in *Proceedings of the 8th international symposium on mining with backfill*, 2004, pp. 286–294.
- [30] M. H. B. Nasser *et al.*, “Cemented Paste Backfill (CPB) Material Properties for Undercut Analysis,” 2022, doi: 10.3390/mining2010007.
- [31] E. Yilmaz, M. Benzaazoua, T. Belem, and B. Bussière, “Effect of curing under pressure on compressive strength development of cemented paste backfill,” *Miner. Eng.*, vol. 22, no. 9–10, pp. 772–785, 2009, doi: 10.1016/j.mineng.2009.02.002.
- [32] E. Yilmaz, T. Belem, M. Benzaazoua, and B. Bussière, “Assessment of the modified CUAPS apparatus to estimate in situ properties of cemented paste backfill,” *Geotech. Test. J.*, vol. 33, no. 5, pp. 351–362, 2010, doi: 10.1520/GTJ102689.
- [33] A. Ghirian and M. Fall, “Strength evolution and deformation behaviour of cemented paste backfill at early ages: Effect of curing stress, filling strategy and drainage,” *Int. J. Min. Sci. Technol.*, vol. 26, no. 5, pp. 809–817, 2016, doi: 10.1016/j.ijmst.2016.05.039.
- [34] L. Cui and M. Fall, “Mechanical and thermal properties of cemented tailings materials at early ages: Influence of initial temperature, curing stress and drainage conditions,” *Constr. Build. Mater.*, vol. 125, pp. 553–563, 2016, doi: 10.1016/j.conbuildmat.2016.08.080.
- [35] N. Yang, X. Chen, R. Li, J. Zhang, H. Hu, and J. Zhang, “Mesoscale numerical investigation of the effects of fiber stiffness on the shear behavior of fiber-reinforced granular soil,” *Comput. Geotech.*, vol. 137, no. January, p. 104259, 2021, doi: 10.1016/j.compgeo.2021.104259.
- [36] T. Oh, I. You, N. Banthia, and D. Y. Yoo, “Deposition of nanosilica particles on fiber surface for improving interfacial bond and tensile performances of ultra-high-performance fiber-reinforced concrete,” *Compos. Part B Eng.*, vol. 221, no. May, p. 109030, 2021, doi: 10.1016/j.compositesb.2021.109030.

- [37] M. Roig-Flores, F. Šimicević, A. Maričić, P. Serna, and M. Horvat, “Interfacial transition zone in mature fiber-reinforced concretes,” *ACI Mater. J.*, vol. 115, no. 4, pp. 623–631, 2018, doi: 10.14359/51702419.
- [38] H. Baji and C. Q. Li, “An analytical solution for hydraulic conductivity of concrete considering properties of the Interfacial Transition Zone (ITZ),” *Cem. Concr. Compos.*, vol. 91, no. November 2017, pp. 1–10, 2018, doi: 10.1016/j.cemconcomp.2018.04.008.
- [39] S. He, Z. Li, and E. H. Yang, “Quantitative characterization of anisotropic properties of the interfacial transition zone (ITZ) between microfiber and cement paste,” *Cem. Concr. Res.*, vol. 122, no. August, pp. 136–146, 2019, doi: 10.1016/j.cemconres.2019.05.007.
- [40] C. Yang, P. Yang, W. sheng Lv, and Z. kai Wang, “Mechanical Performance of Confined Consolidation on the Strength Development of Cemented Paste Backfill,” *Geotech. Geol. Eng.*, vol. 38, no. 2, pp. 1097–1110, 2020, doi: 10.1007/s10706-019-01074-x.
- [41] B. Ali, E. Yilmaz, A. R. Tahir, F. Gamaoun, M. H. El Ouni, and S. M. Murtaza Rizvi, “The Durability of High-Strength Concrete Containing Waste Tire Steel Fiber and Coal Fly Ash,” *Adv. Mater. Sci. Eng.*, vol. 2021, 2021, doi: 10.1155/2021/7329685.
- [42] B. Ali, E. Yilmaz, M. Sohail Jameel, W. Haroon, and R. Alyousef, “Consolidated effect of fiber-reinforcement and concrete strength class on mechanical performance, economy and footprint of concrete for pavement use,” *J. King Saud Univ. - Eng. Sci.*, no. xxxx, 2021, doi: 10.1016/j.jksues.2021.09.005.
- [43] K. H. Tan, J. Walraven, S. Grünwald, J. Rovers, and B. Cotovanu, “Correlations among notched beam tests, double punch tests and round panel tests for a high performance fibre concrete cast at site,” *Cem. Concr. Compos.*, vol. 122, no. May, p. 104138, 2021, doi: 10.1016/j.cemconcomp.2021.104138.
- [44] C. Chen, G. Zhang, J. G. Zornberg, A. M. Morsy, and J. Huang, “Interface bond behavior of tensioned glass fiber-reinforced polymer (GFRP) tendons embedded in cemented soils,” *Constr. Build. Mater.*, vol. 263, p. 120132, 2020, doi: 10.1016/j.conbuildmat.2020.120132.
- [45] A. Ateş, “Mechanical properties of sandy soils reinforced with cement and randomly distributed glass fibers (GRC),” *Compos. Part B Eng.*, vol. 96, pp. 295–304, 2016, doi:

- 10.1016/j.compositesb.2016.04.049.
- [46] H. Soleimani-Fard, D. König, and M. Goudarzy, “Plane strain shear strength of unsaturated fiber-reinforced fine-grained soils,” *Acta Geotech.*, vol. 17, no. 1, pp. 105–118, 2022, doi: 10.1007/s11440-021-01197-7.
- [47] M. Deng, M. Zhang, F. Ma, F. Li, and H. Sun, “Flexural strengthening of over-reinforced concrete beams with highly ductile fiber-reinforced concrete layer,” *Eng. Struct.*, vol. 231, no. October 2020, p. 111725, 2021, doi: 10.1016/j.engstruct.2020.111725.
- [48] H. T. N. Nguyen, Y. Li, and K. H. Tan, “Shear behavior of fiber-reinforced concrete hollow-core slabs under elevated temperatures,” *Constr. Build. Mater.*, vol. 275, 2021, doi: 10.1016/j.conbuildmat.2020.121362.
- [49] L. Xu, F. Deng, and Y. Chi, “Nano-mechanical behavior of the interfacial transition zone between steel-polypropylene fiber and cement paste,” *Constr. Build. Mater.*, vol. 145, pp. 619–638, 2017, doi: 10.1016/j.conbuildmat.2017.04.035.
- [50] Q. Wang, G. Zhang, Y. Tong, and C. Gu, “Prediction on permeability of engineered cementitious composites,” *Crystals*, vol. 11, no. 5, pp. 1–10, 2021, doi: 10.3390/cryst11050526.
- [51] J. Němeček, P. Kabele, and Z. Bittnar, “Nanoindentation based assessment of micro-mechanical properties of fiber reinforced cementitious composite,” in *6th International RILEM Symposium on Fibre-Reinforced Concretes (FRC)*, 2004, no. September, pp. 401–410. [Online]. Available: [http://www.rilem.org/gene/main.php?base=500218&id\\_publication=44&id\\_papier=673](http://www.rilem.org/gene/main.php?base=500218&id_publication=44&id_papier=673)
- [52] V. Zacharda, P. Štemberk, and J. Němeček, “Nanomechanical performance of interfacial transition zone in fiber reinforced cement matrix,” *Key Eng. Mater.*, vol. 760 KEM, pp. 251–256, 2018, doi: 10.4028/www.scientific.net/KEM.760.251.
- [53] R. S. Teixeira *et al.*, “Nanoindentation study of the interfacial zone between cellulose fiber and cement matrix in extruded composites,” *Cem. Concr. Compos.*, vol. 85, pp. 1–8, 2018, doi: 10.1016/j.cemconcomp.2017.09.018.
- [54] L. Li, Z. Li, M. Cao, Y. I. Tang, and Z. H. E. Zhang, “Nanoindentation and porosity fractal

- dimension of calcium carbonate whisker reinforced cement paste after elevated temperatures (UP to 900°C),” *Fractals*, vol. 29, no. 2, pp. 1–16, 2021, doi: 10.1142/S0218348X21400016.
- [55] J. Han, D. Huang, J. Chen, and X. Lan, “Experiment study and finite element analysis of the coupling effect of steel fiber length and coarse aggregate maximum size on the fracture properties of concrete,” *Crystals*, vol. 11, no. 8, 2021, doi: 10.3390/cryst11080850.
- [56] J. L. Zhang, X. Liu, Y. Yuan, and H. A. Mang, “Multiscale modeling of the effect of the interfacial transition zone on the modulus of elasticity of fiber-reinforced fine concrete,” *Comput. Mech.*, vol. 55, no. 1, pp. 37–55, 2015, doi: 10.1007/s00466-014-1081-6.
- [57] X. Qian, B. Shen, B. Mu, and Z. Li, “Enhancement of aging resistance of glass fiber reinforced cement,” *Mater. Struct. Constr.*, vol. 36, no. 259, pp. 323–329, 2003, doi: 10.1617/13843.
- [58] Y. Wang, L. Wei, J. Yu, and K. Yu, “Mechanical properties of high ductile magnesium oxychloride cement-based composites after water soaking,” *Cem. Concr. Compos.*, vol. 97, no. August 2017, pp. 248–258, 2019, doi: 10.1016/j.cemconcomp.2018.12.028.
- [59] T. Zhang, Y. Zhang, H. Zhu, and Z. Yan, “Experimental investigation and multi-level modeling of the effective thermal conductivity of hybrid micro-fiber reinforced cementitious composites at elevated temperatures,” *Compos. Struct.*, vol. 256, no. August 2020, p. 112988, 2021, doi: 10.1016/j.compstruct.2020.112988.
- [60] R. J. Flatt, G. W. Scherer, and J. W. Bullard, “Why alite stops hydrating below 80% relative humidity,” *Cem. Concr. Res.*, vol. 41, no. 9, pp. 987–992, 2011, doi: 10.1016/j.cemconres.2011.06.001.
- [61] A. Zhou, H. Wei, T. Liu, D. Zou, Y. Li, and R. Qin, “Interfacial technology for enhancement in steel fiber reinforced cementitious composite from nano to macroscale,” *Nanotechnol. Rev.*, vol. 10, no. 1, pp. 636–652, 2021, doi: 10.1515/ntrev-2021-0037.
- [62] J. Cheng, T. C. Li, X. Liu, and L. H. Zhao, “A 3D discrete FEM iterative algorithm for solving the water pipe cooling problems of massive concrete structures,” *Int. J. Numer. Anal. Methods Geomech.*, vol. 40, pp. 487–508, 2015, [Online]. Available:

[http://onlinelibrary.wiley.com/doi/10.1002/nag.527/abstract%5Cnhttps://web.natur.cuni.cz/uhigug/masin/download/MTVC\\_IJNAMG06-pp.pdf](http://onlinelibrary.wiley.com/doi/10.1002/nag.527/abstract%5Cnhttps://web.natur.cuni.cz/uhigug/masin/download/MTVC_IJNAMG06-pp.pdf)

- [63] J. M. Mayoral and M. P. Romo, “Seismic response of bridges with massive foundations,” *Soil Dyn. Earthq. Eng.*, vol. 71, pp. 88–99, 2015, doi: 10.1016/j.soildyn.2015.01.008.
- [64] E. O. L. Lantsoght, “How do steel fibers improve the shear capacity of reinforced concrete beams without stirrups?,” *Compos. Part B Eng.*, vol. 175, no. July, p. 107079, 2019, doi: 10.1016/j.compositesb.2019.107079.
- [65] B. R. Ellingwood and Y. Mori, “Probabilistic methods for condition assessment and life prediction of concrete structures in nuclear power plants,” *Nucl. Eng. Des.*, vol. 142, no. 2–3, pp. 155–166, 1993, doi: 10.1016/0029-5493(93)90199-J.
- [66] A. Wang, S. Cao, and E. Yilmaz, “Effect of height to diameter ratio on dynamic characteristics of cemented tailings backfills with fiber reinforcement through impact loading,” *Constr. Build. Mater.*, vol. 322, no. November 2021, p. 126448, 2022, doi: 10.1016/j.conbuildmat.2022.126448.
- [67] J. Li, S. Cao, E. Yilmaz, and Y. Liu, “Compressive fatigue behavior and failure evolution of additive fiber-reinforced cemented tailings composites,” *Int. J. Miner. Metall. Mater.*, vol. 29, no. 2, pp. 345–355, 2022, doi: 10.1007/s12613-021-2351-x.
- [68] D. Deb and S. Jain, “Compaction-Based Analytical Stress Model for 3D Inclined Backfilled Stopes,” *Int. J. Geomech.*, vol. 18, no. 4, p. 04018009, 2018, doi: 10.1061/(asce)gm.1943-5622.0001112.
- [69] A. Janalizadeh Choobbasti and S. Soleimani Kutanaei, “Effect of fiber reinforcement on deformability properties of cemented sand,” *J. Adhes. Sci. Technol.*, vol. 31, no. 14, pp. 1576–1590, 2017, doi: 10.1080/01694243.2016.1264681.
- [70] A. J. Choobbasti, S. S. Kutanaei, and M. Ghadakpour, “Shear behavior of fiber-reinforced sand composite,” *Arab. J. Geosci.*, vol. 12, no. 5, 2019, doi: 10.1007/s12517-019-4326-z.
- [71] S. S. Kutanaei and A. J. Choobbasti, “Triaxial behavior of fiber-reinforced cemented sand,” *J. Adhes. Sci. Technol.*, vol. 30, no. 6, pp. 579–593, 2016, doi: 10.1080/01694243.2015.1110073.

- [72] B. Shafei, M. Kazemian, M. Dopko, and M. Najimi, “State-of-the-art review of capabilities and limitations of polymer and glass fibers used for fiber-reinforced concrete,” *Materials (Basel)*, vol. 14, no. 2, pp. 1–45, 2021, doi: 10.3390/ma14020409.
- [73] V. P. Berardi, “Fracture failure modes in fiber-reinforced polymer systems used for strengthening existing structures,” *Appl. Sci.*, vol. 11, no. 14, 2021, doi: 10.3390/app11146344.
- [74] S. Abdallah, M. Fan, and D. W. A. Rees, “Bonding Mechanisms and Strength of Steel Fiber–Reinforced Cementitious Composites: Overview,” *J. Mater. Civ. Eng.*, vol. 30, no. 3, p. 04018001, 2018, doi: 10.1061/(asce)mt.1943-5533.0002154.
- [75] B. Boulekbache, M. Hamrat, M. Chemrouk, and S. Amziane, “Failure mechanism of fibre reinforced concrete under splitting test using digital image correlation,” *Mater. Struct. Constr.*, vol. 48, no. 8, pp. 2713–2726, 2015, doi: 10.1617/s11527-014-0348-x.
- [76] A. Dubey, “Fiber Reinforced Concrete: Characterization of flexural toughness & some studies of fiber matrix bond slip interactions,” University of British Columbia, 1999.
- [77] A. Dalalbashi, B. Ghiassi, D. V. Oliveira, and A. Freitas, “Effect of test setup on the fiber-to-mortar pull-out response in TRM composites: Experimental and analytical modeling,” *Compos. Part B Eng.*, vol. 143, no. February, pp. 250–268, 2018, doi: 10.1016/j.compositesb.2018.02.010.
- [78] A. Takaku and R. G. C. Arridge, “The effect of interfacial radial and shear stress on fibre pull-out in composite materials,” *J. Phys. D. Appl. Phys.*, vol. 6, no. 17, pp. 2038–2047, 1973, doi: 10.1088/0022-3727/6/17/310.
- [79] J. K. Kim, L. M. Zhou, and Y. W. Mai, “Interfacial debonding and fibre pull-out stresses - Part II A new model based on the fracture mechanics approach,” *J. Mater. Sci.*, vol. 27, no. 12, pp. 3155–3166, 1992, doi: 10.1007/BF01116005.
- [80] K. V. Pochiraju, G. P. Tandon, and N. J. Pagano, “Analyses of single fiber pushout considering interfacial friction and adhesion,” *J. Mech. Phys. Solids*, vol. 49, no. 10, pp. 2307–2338, 2001, doi: 10.1016/S0022-5096(01)00045-X.
- [81] L. Chi, S. Lu, and Y. Yao, “Damping additives used in cement-matrix composites: A

- review,” *Compos. Part B Eng.*, vol. 164, no. April 2018, pp. 26–36, 2019, doi: 10.1016/j.compositesb.2018.11.057.
- [82] T. Liu, R. Bai, Z. Chen, Y. Li, and Y. Yang, “Tailoring of polyethylene fiber surface by coating silane coupling agent for strain hardening cementitious composite,” *Constr. Build. Mater.*, vol. 278, p. 122263, 2021, doi: 10.1016/j.conbuildmat.2021.122263.
- [83] B. D. Ellis, D. L. McDowell, and M. Zhou, “Simulation of single fiber pullout response with account of fiber morphology,” *Cem. Concr. Compos.*, vol. 48, pp. 42–52, 2014, doi: 10.1016/j.cemconcomp.2014.01.003.
- [84] A. Perrot and D. Rangeard, “Effects of mix design parameters on consolidation behaviour of fresh cement-based materials,” *Mater. Struct. Constr.*, vol. 50, no. 2, pp. 1–9, 2017, doi: 10.1617/s11527-016-0988-0.
- [85] Y. Ji, L. Pel, and Z. Sun, “The microstructure development during bleeding of cement paste: An NMR study,” *Cem. Concr. Res.*, vol. 125, no. July, p. 105866, 2019, doi: 10.1016/j.cemconres.2019.105866.
- [86] L. Cui and M. Fall, “Numerical Simulation of Consolidation Behavior of Large Hydrating Fill Mass,” *Int. J. Concr. Struct. Mater.*, vol. 14, no. 1, 2020, doi: 10.1186/s40069-020-0398-0.
- [87] F. Lin and C. Meyer, “Hydration kinetics modeling of Portland cement considering the effects of curing temperature and applied pressure,” *Cem. Concr. Res.*, vol. 39, no. 4, pp. 255–265, 2009, doi: 10.1016/j.cemconres.2009.01.014.
- [88] E. A. H. Alwesabi, B. H. A. Bakar, I. M. H. Alshaikh, A. M. Zeyad, A. Altheeb, and H. Alghamdi, “Experimental investigation on fracture characteristics of plain and rubberized concrete containing hybrid steel-polypropylene fiber,” *Structures*, vol. 33, no. July, pp. 4421–4432, 2021, doi: 10.1016/j.istruc.2021.07.011.
- [89] B. A. Graybeal, “Compressive Behavior of Ultra-High-Performance Fiber-Reinforced Concrete,” vol. 146, no. 104, 2007.
- [90] H. Yazici *et al.*, “Compressive fatigue behavior and failure evolution of additive fiber-reinforced cemented tailings composites,” *Mater. Struct. Constr.*, vol. 48, no. 2, pp. 209–

- 220, 2018, doi: 10.1007/s12613-021-2351-x.
- [91] Y. Zhang, J. W. Ju, Q. Chen, Z. Yan, H. Zhu, and Z. Jiang, “Characterizing and analyzing the residual interfacial behavior of steel fibers embedded into cement-based matrices after exposure to high temperatures,” *Compos. Part B Eng.*, vol. 191, no. December 2019, p. 107933, 2020, doi: 10.1016/j.compositesb.2020.107933.
- [92] M. Helmi, M. R. Hall, L. A. Stevens, and S. P. Rigby, “Effects of high-pressure/temperature curing on reactive powder concrete microstructure formation,” *Constr. Build. Mater.*, vol. 105, pp. 554–562, 2016, doi: 10.1016/j.conbuildmat.2015.12.147.
- [93] S. F. Lee and S. Jacobsen, “Study of interfacial microstructure, fracture energy, compressive energy and debonding load of steel fiber-reinforced mortar,” *Mater. Struct. Constr.*, vol. 44, no. 8, pp. 1451–1465, 2011, doi: 10.1617/s11527-011-9710-4.
- [94] G. Ye, P. Lura, and K. Van Breugel, “Modelling of water permeability in cementitious materials,” *Mater. Struct. Constr.*, vol. 39, no. 9, pp. 877–885, 2006, doi: 10.1617/s11527-006-9138-4.
- [95] M. L. Witteman and P. H. Simms, “Unsaturated flow in hydrating porous media with application to cemented mine backfill,” *Can. Geotech. J.*, vol. 54, no. 6, pp. 835–845, 2017, doi: 10.1139/cgj-2015-0314.
- [96] S. Chakilam and L. Cui, “Effect of polypropylene fiber content and fiber length on the saturated hydraulic conductivity of hydrating cemented paste backfill,” *Constr. Build. Mater.*, vol. 262, p. 120854, 2020, doi: 10.1016/j.conbuildmat.2020.120854.
- [97] L. Festugato, A. Fourie, and N. C. Consoli, “Cyclic shear response of fibre-reinforced cemented paste backfill,” *Geotech. Lett.*, vol. 3, no. JAN/MAR, pp. 5–12, 2013, doi: 10.1680/geolett.12.00042.
- [98] G. Ye *et al.*, “Evaluation of internal bleeding in concrete using a self-weight bleeding test,” *Mater. Struct. Constr.*, vol. 39, no. 6, pp. 1–9, 2017, doi: 10.1061/(asce)gt.1943-5606.0001524.
- [99] K. Rajesh Kumar, G. Shyamala, and A. Adesina, “Structural performance of corroded reinforced concrete beams made with fiber-reinforced self-compacting concrete,”

- Structures*, vol. 32, no. January, pp. 1145–1155, 2021, doi: 10.1016/j.istruc.2021.03.079.
- [100] G. Suazo, A. Fourie, and J. Doherty, “Experimental Study of the Evolution of the Soil Water Retention Curve for Granular Material Undergoing Cement Hydration,” *J. Geotech. Geoenvironmental Eng.*, vol. 142, no. 7, p. 04016022, 2016, doi: 10.1061/(asce)gt.1943-5606.0001468.
- [101] L. Cui and M. Fall, “Modeling of self-desiccation in a cemented backfill structure,” *Int. J. Numer. Anal. Methods Geomech.*, vol. 42, no. 3, pp. 558–583, 2018, doi: 10.1002/nag.2756.
- [102] N. Lu, “Generalized Soil Water Retention Equation for Adsorption and Capillarity,” *J. Geotech. Geoenvironmental Eng.*, vol. 142, no. 10, 2016, doi: 10.1061/(asce)gt.1943-5606.0001524.
- [103] P. Simms and M. Grabinsky, “Direct measurement of matric suction in triaxial tests on early-age cemented paste backfill,” *Can. Geotech. J.*, vol. 46, no. 1, pp. 93–101, 2009, doi: 10.1139/T08-098.
- [104] R. Gao, K. Zhou, W. Liu, and Q. Ren, “Correlation between the pore structure and water retention of cemented paste backfill using centrifugal and nuclear magnetic resonance methods,” *Minerals*, vol. 10, no. 7, pp. 1–19, 2020, doi: 10.3390/min10070610.
- [105] I. Loan, S. Libos, L. Cui, and X. Liu, “Effect of curing temperature on time-dependent shear behavior and properties of polypropylene fiber-reinforced cemented paste backfill,” *Constr. Build. Mater.*, vol. 311, no. October, p. 125302, 2021, doi: 10.1016/j.conbuildmat.2021.125302.
- [106] I. L. S. Libos and L. Cui, “Effects of curing time, cement content, and saturation state on mode-I fracture toughness of cemented paste backfill,” *Eng. Fract. Mech.*, vol. 235, no. January, p. 107174, 2020, doi: 10.1016/j.engfracmech.2020.107174.
- [107] L. Cui and M. Fall, “Coupled thermo-hydro-mechanical-chemical modeling of the geotechnical response of cemented paste backfill structures,” *70 Years Can. Geotech. Geosci. (GeoOttawa 2017)*, no. November, 2017.
- [108] F. Abbasy, F. P. Hassani, S. A. G. Madiseh, J. Côté, and M. R. Nokken, “An experimental study on the effective parameters of thermal conductivity of mine backfill,” *Heat Transf.*

- Eng.*, vol. 35, no. 13, pp. 1209–1224, 2014, doi: 10.1080/01457632.2013.870373.
- [109] M. Wyrzykowski, P. J. McDonald, K. L. Scrivener, and P. Lura, “Water Redistribution within the Microstructure of Cementitious Materials due to Temperature Changes Studied with  $^1\text{H}$  NMR,” *J. Phys. Chem. C*, vol. 121, no. 50, pp. 27950–27962, 2017, doi: 10.1021/acs.jpcc.7b08141.
- [110] E. J. Sellevold and Bjøntegaard, “Coefficient of thermal expansion of cement paste and concrete: Mechanisms of moisture interaction,” *Mater. Struct. Constr.*, vol. 39, no. 9, pp. 809–815, 2006, doi: 10.1617/s11527-006-9086-z.
- [111] S. Caré, “Effect of temperature on porosity and on chloride diffusion in cement pastes,” *Constr. Build. Mater.*, vol. 22, no. 7, pp. 1560–1573, 2008, doi: 10.1016/j.conbuildmat.2007.03.018.
- [112] S. Shiozawa and G. S. Campbell, “Soil thermal conductivity,” *Remote Sens. Rev.*, vol. 5, no. 1, pp. 301–310, 1990, doi: 10.1080/02757259009532137.
- [113] W. J. Likos, “Pore-Scale Model for Thermal Conductivity of Unsaturated Sand,” *Geotech. Geol. Eng.*, vol. 33, no. 2, pp. 179–192, 2015, doi: 10.1007/s10706-014-9744-9.
- [114] D. Belkharouché and A. Chaker, “Effects of moisture on thermal conductivity of the lightened construction material,” *Int. J. Hydrogen Energy*, vol. 41, no. 17, pp. 7119–7125, 2016, doi: 10.1016/j.ijhydene.2016.01.160.
- [115] J. I. Escalante-García and J. H. Sharp, “Effect of Temperature on the Hydration of the Main Clinker,” *Cem. Concr. Res.*, vol. 28, no. 9, pp. 1245–1257, 1998.
- [116] R. Snellings *et al.*, “Hydration kinetics of ternary slag-limestone cements: Impact of water to binder ratio and curing temperature,” *Cem. Concr. Res.*, vol. 151, no. October 2021, p. 106647, 2022, doi: 10.1016/j.cemconres.2021.106647.
- [117] 225 AC, “Guide to the selection and use of hydraulic cements,” *Am. Concr. Inst.*, 2016.
- [118] F. Meducin, H. Zanni, C. Noik, G. Hamel, and B. Bresson, “Tricalcium silicate (C3S) hydration under high pressure at ambient and high temperature (200 °C),” *Cem. Concr. Res.*, vol. 38, no. 3, pp. 320–324, 2008, doi: 10.1016/j.cemconres.2007.09.024.

- [119] B. Bresson, F. Meducin, H. Zanni, and C. Noik, “Hydration of tricalcium silicate (C3S) at high temperature and high pressure,” *J. Mater. Sci.*, vol. 37, no. 24, pp. 5355–5365, 2002, doi: 10.1023/A:1021093528888.
- [120] Q. Zhou and J. J. Beaudoin, “Effect of applied hydrostatic stress on the hydration of Portland cement and C3S,” *Adv. Cem. Res.*, vol. 15, no. 1, pp. 9–16, 2003, doi: 10.1680/adcr.2003.15.1.9.
- [121] A. Neville, “Creep of concrete: plain, reinforced, and prestressed,” 1971.
- [122] G. Goracci, M. Monasterio, H. Jansson, and S. Cervený, “Dynamics of nano-confined water in Portland cement - Comparison with synthetic C-S-H gel and other silicate materials,” *Sci. Rep.*, vol. 7, no. 1, pp. 1–10, 2017, doi: 10.1038/s41598-017-08645-z.
- [123] T. Honorio, F. Masara, and F. Benboudjema, “Heat capacity, isothermal compressibility, isosteric heat of adsorption and thermal expansion of water confined in C-S-H,” *Cement*, vol. 6, no. January 2021, p. 100015, 2021, doi: 10.1016/j.cement.2021.100015.
- [124] S. Xu, G. C. Simmons, and G. W. Scherer, “Thermal expansion and viscosity of confined liquids,” *Mater. Res. Soc. Symp. - Proc.*, vol. 790, pp. 85–91, 2003, doi: 10.1557/proc-790-p6.8.
- [125] S. H. Garofalini, T. S. Mahadevan, S. Xu, and G. W. Scherer, “Molecular mechanisms causing anomalously high thermal expansion of nanoconfined water,” *ChemPhysChem*, vol. 9, no. 14, pp. 1997–2001, 2008, doi: 10.1002/cphc.200800455.
- [126] S. Mindness, J. Young, and D. Darwin, “Concrete: Prentice Hall,” in *Concrete: Prentice Hall*, Prentice Hall, 2003.
- [127] N. Zhang, X. Yu, A. Pradhan, and A. J. Puppala, “Thermal Conductivity of Quartz Sands by Thermo-Time Domain Reflectometry Probe and Model Prediction,” *J. Mater. Civ. Eng.*, vol. 27, no. 12, pp. 1–10, 2015, doi: 10.1061/(asce)mt.1943-5533.0001332.
- [128] K. Sakyi-Bekoe, “Assessment of the Coefficient of Thermal Expansion of Alabama Concrete,” p. 213, 2008.
- [129] N. I. Kömle, E. S. Hütter, and W. J. Feng, “Thermal conductivity measurements of coarse-

- grained gravel materials using a hollow cylindrical sensor,” *Acta Geotech.*, vol. 5, no. 4, pp. 211–223, 2010, doi: 10.1007/s11440-010-0126-z.
- [130] A. Neville and J. Brooks, “Concrete Technology: Longman Scientific & Technical England,” 1987.
- [131] M. A. Kant, J. Ammann, E. Rossi, C. Madonna, D. Höser, and P. Rudolf Von Rohr, “Thermal properties of Central Aare granite for temperatures up to 500 °C: Irreversible changes due to thermal crack formation,” *Geophys. Res. Lett.*, doi: 10.1002/2016GL070990.
- [132] *Concrete microstructure, properties and Materials. 3rd ed. New York: Mcgraw Hill. 2017.*
- [133] A. P. S. Selvadurai and S. M. Rezaei Niya, “Effective thermal conductivity of an intact heterogeneous limestone,” *J. Rock Mech. Geotech. Eng.*, vol. 12, no. 4, pp. 682–692, 2020, doi: 10.1016/j.jrmge.2020.04.001.
- [134] O. A. Balogun, A. A. Akinwande, A. A. Adediran, P. P. Ikubanni, S. A. Shittu, and O. S. Adesina, “Experimental Study on the Properties of Fired Sand–Clay Ceramic Products for Masonry Applications,” *J. Mater. Civ. Eng.*, vol. 33, no. 2, pp. 1–12, 2021, doi: 10.1061/(asce)mt.1943-5533.0003532.
- [135] Y. Du and Y. Ge, “Multiphase model for predicting the thermal conductivity of cement paste and its applications,” *Materials (Basel)*., vol. 14, no. 16, 2021, doi: 10.3390/ma14164525.
- [136] M. J. Abdolhosseini Qomi, F. J. Ulm, and R. J. M. Pellenq, “Physical origins of thermal properties of cement paste,” *Phys. Rev. Appl.*, vol. 3, no. 6, pp. 1–17, 2015, doi: 10.1103/PhysRevApplied.3.064010.
- [137] S. Ghabezloo, “Micromechanics analysis of thermal expansion and thermal pressurization of a hardened cement paste,” *Cem. Concr. Res.*, vol. 41, no. 5, pp. 520–532, 2011, doi: 10.1016/j.cemconres.2011.01.023.
- [138] H. Xu, Y. Zhao, S. C. Vogel, L. L. Daemen, and D. D. Hickmott, “Anisotropic thermal expansion and hydrogen bonding behavior of portlandite: A high-temperature neutron diffraction study,” *J. Solid State Chem.*, vol. 180, no. 4, pp. 1519–1525, 2007, doi:

10.1016/j.jssc.2007.03.004.

- [139] K. J. Krakowiak *et al.*, “Engineering of high specific strength and low thermal conductivity cementitious composites with hollow glass microspheres for high-temperature high-pressure applications,” *Cem. Concr. Compos.*, vol. 108, no. May 2019, p. 103514, 2020, doi: 10.1016/j.cemconcomp.2020.103514.
- [140] T. D., *Practical Guide to Polypropylene: RAPRA Technology*. 2002.
- [141] J. Mark, *Polymer Data Handbook*. Oxford University Press, 2009.
- [142] T. Kashiwagi *et al.*, “Thermal and flammability properties of polypropylene/carbon nanotube nanocomposites,” *Polymer (Guildf)*., vol. 45, no. 12, pp. 4227–4239, 2004, doi: 10.1016/j.polymer.2004.03.088.
- [143] J. Stolz, Y. Boluk, and V. Bindiganavile, “Mechanical, thermal and acoustic properties of cellular alkali activated fly ash concrete,” *Cem. Concr. Compos.*, vol. 94, no. August, pp. 24–32, 2018, doi: 10.1016/j.cemconcomp.2018.08.004.
- [144] Y. Wang, “Study on high temperature behaviours of FRHPC pipe members,” Dalian University of Technology, 2008.
- [145] Y. Zhang, J. W. Ju, H. Zhu, Q. Guo, and Z. Yan, “Micromechanics based multi-level model for predicting the coefficients of thermal expansion of hybrid fiber reinforced concrete,” *Constr. Build. Mater.*, vol. 190, pp. 948–963, 2018, doi: 10.1016/j.conbuildmat.2018.09.030.
- [146] H. G. Noh, H. C. Kang, M. H. Kim, and H. S. Park, “Estimation Model for Effective Thermal Conductivity of Reinforced Concrete Containing Multiple Round Rebars,” *Int. J. Concr. Struct. Mater.*, vol. 12, no. 1, 2018, doi: 10.1186/s40069-018-0291-2.
- [147] T. Hassan *et al.*, “Acoustic, mechanical and thermal properties of green composites reinforced with natural fiberswaste,” *Polymers (Basel)*., vol. 12, no. 3, 2020, doi: 10.3390/polym12030654.
- [148] R. Stapulionienė, S. Vaitkus, S. Vėjelis, and A. Sankauskaitė, “Investigation of thermal conductivity of natural fibres processed by different mechanical methods,” *Int. J. Precis.*

- Eng. Manuf.*, vol. 17, no. 10, pp. 1371–1381, 2016, doi: 10.1007/s12541-016-0163-0.
- [149] J. J. Valenza and G. W. Scherer, “Evidence of anomalous thermal expansion of water in cement paste,” *Cem. Concr. Res.*, vol. 35, no. 1, pp. 57–66, 2005, doi: 10.1016/j.cemconres.2004.08.022.
- [150] Z. Zhao, C. Sun, and R. Zhou, “Thermal conductivity of confined-water in graphene nanochannels,” *Int. J. Heat Mass Transf.*, vol. 152, p. 119502, 2020, doi: 10.1016/j.ijheatmasstransfer.2020.119502.
- [151] X. Wang, H. Shao, J. Hesser, C. Zhang, W. Wang, and O. Kolditz, “Numerical analysis of thermal impact on hydro-mechanical properties of clay,” *J. Rock Mech. Geotech. Eng.*, vol. 6, no. 5, pp. 405–416, 2014, doi: 10.1016/j.jrmge.2014.07.002.
- [152] V. R. Tarnawski and W. H. Leong, “Advanced Geometric Mean Model for Predicting Thermal Conductivity of Unsaturated Soils,” *Int. J. Thermophys.*, vol. 37, no. 2, pp. 1–42, 2016, doi: 10.1007/s10765-015-2024-y.
- [153] M. Zhang, G. Ye, and K. Van Breugel, “Microstructure-based modeling of water diffusivity in cement paste,” *Constr. Build. Mater.*, vol. 25, no. 4, pp. 2046–2052, 2011, doi: 10.1016/j.conbuildmat.2010.11.042.
- [154] X. Pang and C. Meyer, “Modeling cement hydration by connecting a nucleation and growth mechanism with a diffusion mechanism. Part II: Portland cement paste hydration,” *Sci. Eng. Compos. Mater.*, vol. 23, no. 6, pp. 605–615, 2016, doi: 10.1515/secm-2013-0259.
- [155] M. Zajac, S. Hoock, C. Stabler, and M. Ben Haha, “Effect of hydration kinetics on properties of compositionally similar binders,” *Cem. Concr. Res.*, vol. 101, no. July, pp. 13–24, 2017, doi: 10.1016/j.cemconres.2017.08.005.
- [156] E. Gartner and T. Sui, “Alternative cement clinkers,” *Cem. Concr. Res.*, vol. 114, pp. 27–39, 2018, doi: 10.1016/j.cemconres.2017.02.002.
- [157] X. Pang, W. Cuello Jimenez, and B. J. Iverson, “Hydration kinetics modeling of the effect of curing temperature and pressure on the heat evolution of oil well cement,” *Cem. Concr. Res.*, vol. 54, no. 110, pp. 69–76, 2013, doi: 10.1016/j.cemconres.2013.08.014.

- [158] A. Schindler and K. Folliard, “Heat of hydration models for cementitious materials,” *ACI M. J.*, vol. 102, no. 2, p. 25, 2005.
- [159] J. W. Bullard, “A three-dimensional microstructural model of reactions and transport in aqueous mineral systems,” *Model. Simul. Mater. Sci. Eng.*, vol. 15, no. 7, pp. 711–738, 2007, doi: 10.1088/0965-0393/15/7/002.
- [160] D. P. Bentz, “Three-dimensional computer simulation of portland cement hydration and microstructure development,” *J. Am. Ceram. Soc.*, vol. 80, no. 1, pp. 3–21, 1997, doi: 10.1111/j.1151-2916.1997.tb02785.x.
- [161] Z. Liu, B. Zhang, and X. Yu, “Multiphysics for early stage cement hydration: Theoretical framework,” *Adv. Mater. Res.*, vol. 255–260, pp. 4247–4250, 2011, doi: 10.4028/www.scientific.net/AMR.255-260.4247.
- [162] G. Sciumè, F. Benboudjema, C. De Sa, F. Pesavento, Y. Berthaud, and B. A. Schrefler, “A multiphysics model for concrete at early age applied to repairs problems,” *Eng. Struct.*, vol. 57, pp. 374–387, 2013, doi: 10.1016/j.engstruct.2013.09.042.
- [163] Z. Liu and X. Yu, “Multiscale Chemico-Thermo-Hydro-Mechanical Modeling of Early-Stage Hydration and Shrinkage of Cement Compounds,” *J. Mater. Civ. Eng.*, vol. 25, no. 9, pp. 1239–1247, 2013, doi: 10.1061/(asce)mt.1943-5533.0000754.
- [164] J. J. Thomas *et al.*, “Modeling and simulation of cement hydration kinetics and microstructure development,” *Cem. Concr. Res.*, vol. 41, no. 12, pp. 1257–1278, 2011, doi: 10.1016/j.cemconres.2010.10.004.
- [165] F. Lin, “Modeling of hydration kinetics and shrinkage of Portland cement paste,” Columbia University, 2006.
- [166] S. Papatzani, K. Paine, and J. Calabria-Holley, “A comprehensive review of the models on the nanostructure of calcium silicate hydrates,” *Constr. Build. Mater.*, vol. 74, no. November, pp. 219–234, 2015, doi: 10.1016/j.conbuildmat.2014.10.029.
- [167] H. M. JENNINGS and S. K. JOHNSON, “Simulation of Microstructure Development During the Hydration of a Cement Compound,” *J. Am. Ceram. Soc.*, vol. 69, no. 11, pp. 790–795, 1986, doi: 10.1111/j.1151-2916.1986.tb07361.x.

- [168] K. Van Breugel, “Simulation of hydration and formation of structure in hardening cement-based materials,” Delft University of Technology, 1993.
- [169] T. Knudsen, “Modeling hydration of Portland cement—the effect of particle size distribution.,” in *Proceedings of the engineering foundation conference on characterization and performance prediction of cement and concrete.*, 1982, pp. 125–150.
- [170] H. NAKAMURA, S. Hamada, T. Tanimoto, and A. Miyamoto, “Estimation of thermal crack resistance for mass concrete structures with uncertain material properties.,” *ACI Struct. J.*, vol. 96, no. 4, pp. 509–518, 1999.
- [171] M. Cervera, R. Faria, J. Oliver, and T. Prato, “Numerical modelling of concrete curing, regarding hydration and temperature phenomena,” *Comput. Struct.*, vol. 80, no. 18–19, pp. 1511–1521, 2002, doi: 10.1016/S0045-7949(02)00104-9.
- [172] D. P. Bentz, “Influence of water-to-cement ratio on hydration kinetics: Simple models based on spatial considerations,” *Cem. Concr. Res.*, vol. 36, no. 2, pp. 238–244, 2006, doi: 10.1016/j.cemconres.2005.04.014.
- [173] Y. Zhang, C. Bouillon, N. Vlasopoulos, and J. J. Chen, “Measuring and modeling hydration kinetics of well cements under elevated temperature and pressure using chemical shrinkage test method,” *Cem. Concr. Res.*, vol. 123, no. July, 2019, doi: 10.1016/j.cemconres.2019.05.013.
- [174] B. Tamboue, “The role of C-S-H microstructure and calcium hydroxide on creep and shrinkage of hardened portland cement paste,” University of Ottawa, 2001.
- [175] E. Fraga, A. Cuesta, J. D. Zea-Garcia, A. G. De la Torre, A. Yáñez-Casal, and M. A. G. Aranda, “Rietveld quantitative phase analysis of oil well cement: In Situ hydration study at 150 Bars and 150 °C,” *Materials (Basel)*, vol. 12, no. 12, 2019, doi: 10.3390/ma12122897.
- [176] M. Chen, L. Lu, S. Wang, P. Zhao, W. Zhang, and S. Zhang, “Investigation on the formation of tobermorite in calcium silicate board and its influence factors under autoclaved curing,” *Constr. Build. Mater.*, vol. 143, pp. 280–288, 2017, doi: 10.1016/j.conbuildmat.2017.03.143.
- [177] X. Pang, P. A. Otieno, and G. P. Funkhouser, “Modeling the Effect of Curing Pressure on

- the Viscosity Evolution of Oilwell Cement,” *2014 AADE Fluids Tech. Conf. Exhib.*, p. AADE-14-FTCE-06, 2014.
- [178] L. Sun, X. Pang, Y. Bu, and C. Wang, “Experimental Study of the Effect of Curing Temperature and Pressure on the Property Evolution of Oil Well Cement,” *55th U.S. Rock Mechanics/Geomechanics Symposium*. p. ARMA-2021-1397, Jun. 18, 2021.
- [179] G. W. Scherer, G. P. Funkhouser, and S. Peethamparan, “Effect of pressure on early hydration of class H and white cement,” *Cem. Concr. Res.*, vol. 40, no. 6, pp. 845–850, 2010, doi: 10.1016/j.cemconres.2010.01.013.
- [180] G. Quercia, H. J. H. Brouwers, A. Garnier, and K. Luke, “Influence of olivine nano-silica on hydration and performance of oil-well cement slurries,” *Mater. Des.*, vol. 96, pp. 162–170, 2016, doi: 10.1016/j.matdes.2016.02.001.
- [181] S. Rahimi-Aghdam, Z. P. Bažant, and M. J. Abdolhosseini Qomi, “Cement hydration from hours to centuries controlled by diffusion through barrier shells of C-S-H,” *J. Mech. Phys. Solids*, vol. 99, no. November 2016, pp. 211–224, 2017, doi: 10.1016/j.jmps.2016.10.010.
- [182] D. Fan and S. Yang, “Mechanical properties of C-S-H globules and interfaces by molecular dynamics simulation,” *Constr. Build. Mater.*, vol. 176, pp. 573–582, 2018, doi: 10.1016/j.conbuildmat.2018.05.085.
- [183] R. G. Patel, D. C. Killoh, L. J. Parrott, and W. A. Gutteridge, “Influence of curing at different relative humidities upon compound reactions and porosity in Portland cement paste,” *Mater. Struct.*, vol. 21, no. 3, pp. 192–197, 1988, doi: 10.1007/BF02473055.
- [184] V. Baroghel-Bouny, P. Mounanga, A. Khelidj, A. Loukili, and N. Rafai, “Autogenous deformations of cement pastes: Part II. W/C effects, micro-macro correlations, and threshold values,” *Cem. Concr. Res.*, vol. 36, no. 1, pp. 123–136, 2006, doi: 10.1016/j.cemconres.2004.10.020.
- [185] P. Vargas, O. Restrepo-Baena, and J. I. Tobón, “Microstructural analysis of interfacial transition zone (ITZ) and its impact on the compressive strength of lightweight concretes,” *Constr. Build. Mater.*, vol. 137, pp. 381–389, 2017, doi: 10.1016/j.conbuildmat.2017.01.101.

- [186] P. D. Tennis and H. M. Jennings, “A Model for two types of calcium silicate hydrate in the microstructure of Portland cement pastes,” *Cem. Concr. Res.*, vol. 30, no. 6, pp. 855–863, 2000, doi: 10.1016/S0008-8846(00)00257-X.
- [187] M. Vandamme, F. J. Ulm, and P. Fonollosa, “Nanogranular packing of C-S-H at substoichiometric conditions,” *Cem. Concr. Res.*, vol. 40, no. 1, pp. 14–26, 2010, doi: 10.1016/j.cemconres.2009.09.017.
- [188] A. Nonat, “The structure and stoichiometry of C-S-H,” *Cem. Concr. Res.*, vol. 34, no. 9, pp. 1521–1528, 2004, doi: 10.1016/j.cemconres.2004.04.035.
- [189] H. M. Jennings, J. J. Thomas, J. S. Gevrenov, G. Constantinides, and F. J. Ulm, “A multi-technique investigation of the nanoporosity of cement paste,” *Cem. Concr. Res.*, vol. 37, no. 3, pp. 329–336, 2007, doi: 10.1016/j.cemconres.2006.03.021.
- [190] I. G. Richardson, “Tobermorite/jennite- and tobermorite/calcium hydroxide-based models for the structure of C-S-H: Applicability to hardened pastes of tricalcium silicate,  $\beta$ -dicalcium silicate, Portland cement, and blends of Portland cement with blast-furnace slag, metakaol,” *Cem. Concr. Res.*, vol. 34, no. 9, pp. 1733–1777, 2004, doi: 10.1016/j.cemconres.2004.05.034.
- [191] G. Constantinides and F. J. Ulm, “The nanogranular nature of C-S-H,” *J. Mech. Phys. Solids*, vol. 55, no. 1, pp. 64–90, 2007, doi: 10.1016/j.jmps.2006.06.003.
- [192] M. Vandamme and F. J. Ulm, “Nanogranular origin of concrete creep,” *Proc. Natl. Acad. Sci. U. S. A.*, vol. 106, no. 26, pp. 10552–10557, 2009, doi: 10.1073/pnas.0901033106.
- [193] P. Mondal, S. P. Shah, L. D. Marks, and J. J. Gaitero, “Comparative study of the effects of microsilica and nanosilica in concrete,” *Transp. Res. Rec.*, no. 2141, pp. 6–9, 2010, doi: 10.3141/2141-02.
- [194] J. J. Kim, M. K. Rahman, and M. M. Reda Taha, “Examining microstructural composition of hardened cement paste cured under high temperature and pressure using nanoindentation and  $^{29}\text{Si}$  MAS NMR,” *Appl. Nanosci.*, vol. 2, no. 4, pp. 445–456, 2012, doi: 10.1007/s13204-012-0058-z.
- [195] I. G. Richardson, “Nature of the hydration products in hardened cement pastes,” *Cem.*

- Concr. Compos.*, vol. 22, no. 2, pp. 97–113, 2000, doi: 10.1016/S0958-9465(99)00036-0.
- [196] S. Yashiro, “Application of particle simulation methods to composite materials: a review,” *Adv. Compos. Mater.*, vol. 26, no. 1, pp. 1–22, 2017, doi: 10.1080/09243046.2016.1222508.
- [197] Y. Wang, “Multiphysics analysis of lightning strike damage in laminated carbon/glass fiber reinforced polymer matrix composite materials: A review of problem formulation and computational modeling,” *Compos. Part A Appl. Sci. Manuf.*, vol. 101, pp. 543–553, 2017, doi: 10.1016/j.compositesa.2017.07.010.
- [198] A. Ferrari, J. Jimenez-Martinez, T. Le Borgne, Y. M. Eheust, and I. Lunati, “Challenges in modeling unstable two-phase flow experiments in porous micromodels,” 1002, doi: 10.1002/2014WR016384.
- [199] P. De Anna *et al.*, “Mixing and reaction kinetics in porous media: An experimental pore scale quantification,” *Environ. Sci. Technol.*, vol. 48, no. 1, pp. 508–516, 2014, doi: 10.1021/es403105b.
- [200] X. Sun *et al.*, “Injectable bioactive polymethyl methacrylate–hydrogel hybrid bone cement loaded with BMP-2 to improve osteogenesis for percutaneous vertebroplasty and kyphoplasty,” *Bio-Design Manuf.*, vol. 5, no. 2, pp. 318–332, 2022, doi: 10.1007/s42242-021-00172-1.
- [201] M. Voltolini *et al.*, “Understanding cement hydration at the microscale: New opportunities from ‘pencil-beam’ synchrotron X-ray diffraction tomography,” *J. Appl. Crystallogr.*, vol. 46, no. 1, pp. 142–152, 2013, doi: 10.1107/S0021889812046985.
- [202] M. Sun, G. Geng, D. Xin, and C. Zou, “Molecular quantification of the decelerated dissolution of tri-calcium silicate (C3S) due to surface adsorption,” *Cem. Concr. Res.*, vol. 152, no. May 2021, p. 106682, 2022, doi: 10.1016/j.cemconres.2021.106682.
- [203] A. J. N. MacLeod, F. G. Collins, and W. Duan, “Effects of carbon nanotubes on the early-age hydration kinetics of Portland cement using isothermal calorimetry,” *Cem. Concr. Compos.*, vol. 119, no. February, p. 103994, 2021, doi: 10.1016/j.cemconcomp.2021.103994.
- [204] J. H. Song and T. Belytschko, “Multiscale aggregating discontinuities method for micro-

- macro failure of composites,” *Compos. Part B Eng.*, vol. 40, no. 6, pp. 417–426, 2009, doi: 10.1016/j.compositesb.2009.01.007.
- [205] X. Ouyang, Z. Wu, B. Shan, Q. Chen, and C. Shi, “A critical review on compressive behavior and empirical constitutive models of concrete,” *Constr. Build. Mater.*, vol. 323, no. January, p. 126572, 2022, doi: 10.1016/j.conbuildmat.2022.126572.
- [206] M. Alber *et al.*, “Integrating machine learning and multiscale modeling—perspectives, challenges, and opportunities in the biological, biomedical, and behavioral sciences,” *npj Digit. Med.*, vol. 2, no. 1, 2019, doi: 10.1038/s41746-019-0193-y.
- [207] L. Wu, P. Liu, Z. Zhang, D. Zhu, and H. Wang, “Multiscale modeling for high-performance concrete: A review,” *Int. J. Multiscale Comput. Eng.*, vol. 16, no. 3, pp. 267–283, 2018, doi: 10.1615/IntJMultCompEng.2018022827.
- [208] K. Matouš, M. G. D. Geers, V. G. Kouznetsova, and A. Gillman, “A review of predictive nonlinear theories for multiscale modeling of heterogeneous materials,” *J. Comput. Phys.*, vol. 330, pp. 192–220, 2017, doi: 10.1016/j.jcp.2016.10.070.
- [209] T. Belem, O. El Aatar, B. Bussière, and M. Benzaazoua, “Gravity-driven 1-D consolidation of cemented paste backfill in 3-m-high columns,” *Innov. Infrastruct. Solut.*, vol. 1, no. 1, pp. 10–14, 2016, doi: 10.1007/s41062-016-0039-2.
- [210] S. F. Veloso Marques, N. C. Consoli, and L. Festugato, “Effects of curing stress on the stiffness of a cement-mixed sand,” *E3S Web Conf.*, vol. 92, pp. 1–5, 2019, doi: 10.1051/e3sconf/20199204006.
- [211] A. Taher, Z. Rabb, J. Kuwano, J. Deng, and T. W. Boon, “Effect of curing stress and period on the mechanical properties of cement-mixed sand,” *Soils Found.*, vol. 51, no. 4, pp. 651–661, 2011, doi: 10.3208/sandf.51.651.
- [212] M. A. Uddin, M. Jameel, H. R. Sobuz, M. S. Islam, and N. M. S. Hasan, “Experimental study on strength gaining characteristics of concrete using Portland Composite Cement,” *KSCE J. Civ. Eng.*, vol. 17, no. 4, pp. 789–796, 2013, doi: 10.1007/s12205-013-0236-x.
- [213] Y. Zhao, A. Taheri, M. Karakus, A. Deng, and L. Guo, “The effect of curing under applied stress on the mechanical performance of cement paste backfill,” *Minerals*, vol. 11, no. 10,

pp. 1–17, 2021, doi: 10.3390/min11101107.